Physics - Dissertations   College of Arts and Sciences

6-1-2012

Measurement Of Neutron Radius In Lead By Parity Violating Scattering Flash ADC DAQ

Ahmed Zafar

zahmed@jlab.org

Follow this and additional works at: http://surface.syr.edu/phy_etd

Part of the Physics Commons

ABSTRACT

This dissertation reports the experiment PREx, a parity violation experiment which is designed to measure the neutron radius in ^{208}Pb. PREx is performed in hall A of Thomas Jefferson National Accelerator Facility from March 19th to June 21st. Longitudionally polarized electrons at energy 1 GeV scattered at and agnle of $\theta_{lab} = 5.8\,^\circ$ from the Lead target. Beam corrected pairty violaing counting rate asymmetry is $(A_{corr} = 594 \pm 50(stat) \pm 9(syst))ppb$ at $Q^2 = 0.009068 GeV^2$.

This dissertation also presents the details of Flash ADC Data Acquisition(FADC DAQ) system for Moller polarimetry in Hall A of Thomas Jefferson National Accelerator Facility. The Moller polarimeter measures the beam polarization to high precision to meet the specification of the PREx(Lead radius experiment). The FADC DAQ is part of the upgrade of Moller polarimetery to reduce the systematic error for PREx. The hardware setup and the results of the FADC DAQ analysis are presented.

MEASUREMENT OF NEUTRON RADIUS IN LEAD BY PARITY VIOLATING SCATTERING

Flash ADC DAQ

A Dissertation Presented to

The Faculty of the Department of Physics

of Syracuse University

In Partial Fulfillment

Of the Requirements for the Degree of

Doctor of Philosophy in Physics

by

Zafar Ahmed

June

2012

Acknowledgements

Dedicated to:

Professor Abdus Salam

TABLE OF CONTENTS

LIST OF TABLES

LIST OF FIGURES

CHAPTER 1

Introduction

The study of density distribution of protons and neutrons in a nucleus is a classic area of research but still it has many challenges to address. Precise measurements of proton and neutron density distribution has significant impact on standard model. The electromagnetic charge of Proton makes it much easy to measure the proton densities in a nucleus [1] with very high accuracy. Parity violation in weak interaction is a powerful tool to probe the Standard Model and to measure different parameters precisely. Previous parity experiments(HAPPEX I, HAPPEX II, HAPPEX III and PVDIS) performed by parity collaboration of hall A of Thomas Jefferson National Accelerator Facility are great success. PREx is designed to measure neutron density distribution in Lead via parity violation and it is considered the most difficult of this series of parity violation experiments in hall A. The charge radius of ^{208}Pb is measured with very high accuracy $r_{charge} = 5.5013(7)fm$[1] so the neutron radius is the important parameter not known with high accuracy. Parity violating scattering of electrons from a nucleus is a test of standard model at low energies and it would give fundamental information about nuclear structure.

Before going into the experimental details of PREx, a short introduction to

weak interaction and parity violation is given here.

1.1 Weak Interaction and Parity Violation

In Physics parity is a discrete symmetry and can be described as the inversion of spatial coordinates($\vec{x} \to -\vec{x}$). It had been believed that laws of physics were same under parity inversion till the physicists came across the theta tau puzzle. In order to explain theta tau puzzle compelling arguments about parity violation in weak interactions were made by Lee and Yang[2] in 1956. Lee and Yang proposed several experiments to check parity conservation in weak interaction. The first observation of parity violation in weak interactions was made by C. S. Wu[3] in beta decay of polarized ^{60}Co nuclei.

The SU(2)×U(1) non abelian gauge field theory of electorweak interaction was developed by Salam, Weinberg and Glashow[4][5][6] in 1960s. One of the many successes of electroweak theory is to explain the parity violation when we express weak interaction as chiral gauge interaction. $W^{\pm}$ and Z^0 are the massive charged and neutral gauge bosons of SU(2)×U(1) model respectively. Evidence of neutral current interactions was first found at CERN in Gargamelle neutrino experiment[7] in 1973. Then in 1978 at SLAC an experiment of parity violation in inelastic electron deuterium scattering was performed. This experiment [8]measured the interference between weak neutral current and electromagnetic current and hence the electroweak model was successfully confirmed.

This thesis describes the details of PREx experiment in which we used parity violation in elastic scattering of polarized electrons by neutrons in Lead atom to measure the electroweak radius of neutron in Lead atom.

1.2   Neutron Skin

A qualitative feature of fundamental importance of nuclear structure in heavy atoms is that the radius of neutron is assumed to be 0.25 fm more than proton radius, this is known as neutron skin. Neutron skin is never measured cleanly in stable nucleus. The proton radius is measured cleanly in the spectroscopy of munoic atoms[9]. It was first calculated by T. W. Donnelly and others[10] that the neutron density could be measured by measuring the parity violating asymmetry. The model Independence of parity violating scattering of electrons makes it the best candidate to measure the neutron density.

1.3   Weak Neutral Current

PREx experiment in hall A was perform end by hitting the Lead target atoms with polarized electrons at energy 1 GeV. In the scattering process electrons exchange γ and Z^0 bosons with nucleons. The weak neutral current from exchange of Z^0 boson gives rise to parity violation and hence scattering amp lite depends upon polarization of incident electrons. At tree level the following Feynman diagrams taken from[11] contribute to the scattering cross section:
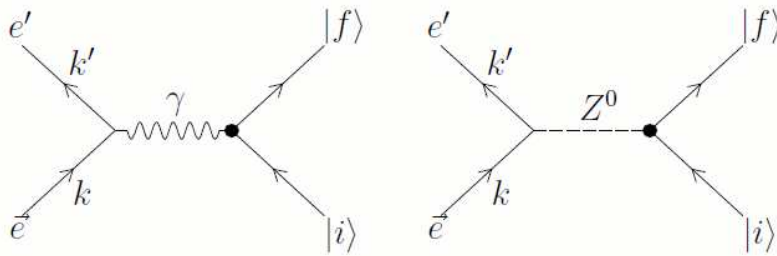
FIG. 1.1: Feynman diagrams for electro-weak scattering of electron and Nucleon.

The S matrix of scattering amplitude of electron nucleon scattering cross section is given by [12]

$$S_{fi} = S_{fi}^{\gamma} - \left(\frac{\hbar}{c}\right)^2 \frac{G}{\sqrt{2}\Omega} \bar{u}\gamma_\mu \left(a + b\gamma_5\right) u \int e^{ik\cdot x} \langle f|\mathcal{J}_\mu^0(x)|i\rangle d^4x \tag{1.1}$$

From equation 1.1 we can see that scattering cross section has both electromagnetic and weak interactions in it. In equation 1.1 S_{fi}^{γ} is the matrix element of electromagnetic cross section, G is Fermi's weak coupling constant the weak neutral current $\mathcal{J}_\mu^0(x)$ is consists upon two parts, one is vector and the other is axial-vector.

$$\langle f|\mathcal{J}_\mu^0(x)|i\rangle = \langle f|J_\mu^0(x) + J_{\mu 5}^0(x)|i\rangle \tag{1.2}$$

In standard model a and b are given by

$$a = -(1 - 4\sin^2\theta_W) \tag{1.3a}$$

$$b = -1. \tag{1.3b}$$

The detailed expression of equation 1.1 in standard model is:

$$\begin{aligned}
S_{fi} = {} & \frac{-(2\pi)^4 \iota}{\Omega^2} \delta^{(4)}(k+i-k'-f)\Bigg\{ \bar{u}(k')(e\gamma_\mu)u(k)\frac{\delta_{\mu\nu}}{q^2}(\bar{u}(f)(-e\gamma_\nu)u(i)) + \\
& \bar{u}(k')\left[\frac{-g\gamma_\mu}{4\cos\theta_w}[1 - 4\sin^2\theta_w + \gamma_5]u(k)\frac{\delta_{\mu\nu} + q_\mu q_\nu/m_Z^2}{q^2 + m_Z^2}\right] \\
& \bar{u}(f)\left[\frac{g\gamma_\nu}{4\cos\theta_W}[1 - 4\sin^2\theta_w + \gamma_5]u(i)\right]\Bigg\}
\end{aligned} \tag{1.4}$$

1.4 Parity Violating Asymmetry

One physically measured quantity in parity violation process is the difference in cross sections of right-handed and left-handed polarized electrons hitting the Lead atom which is known as parity violating asymmetry. If $\frac{d\sigma}{d\Omega}$ is the differentail cross section of electron neutron scattering as described in fig1.1, then the parity violation asymmetry is defined as:

$$A_{\mathrm{PV}} = \left\{ \frac{d\sigma^R}{d\Omega} - \frac{d\sigma^L}{d\Omega} \right\} \bigg/ \left\{ \frac{d\sigma^R}{d\Omega} + \frac{d\sigma^L}{d\Omega} \right\}, \tag{1.5}$$

for simplicity the above equation can be written as:

$$A_{\mathrm{PV}} = \left\{ \sigma^R - \sigma^L \right\} / \left\{ \sigma^R + \sigma^L \right\}, \tag{1.6}$$

Where σ^R is cross section for right handed polarized electrons and σ^L is cross section for left handed polarized electrons. The differential cross section for inclusive electron scattering from nuclei in plane wave Born approximation is proportional to square of amplitudes. The parity violating asymmetry for electron nucleon scattering was calculated first time by Donnelly, Dubach and Sick [10].

$$A_{\mathrm{PV}} = \left\{ \frac{G|Q^2|\kappa}{2\pi\alpha\sqrt{2}} \right\} \frac{W^{(pv)}}{F^2}, \tag{1.7}$$

In equation 1.7 we kept only the square of the amplitude and G is Fermi's weak coupling constant, α is fine structure constant, Q^2 is four momentum transfer and $\kappa = 1$ in Standard Model. $W^{(pv)}$ and F^2 are parity violating weak interaction response function and electromagnetic form factor respectively which are given by:

$$F^2 = \upsilon_L F_L^2 + \upsilon_T F_T^2, \tag{1.8}$$

$$W^{(PV)} = \upsilon_L W_{AV}^L + \upsilon_T W_{AV}^T + \upsilon_{T'} W_{AV}^{T'}, \tag{1.9}$$

Subscripts and superscripts V,T and T' describe the longitudinal and two transverse directions. Four momentum transfer $Q^2 = \omega^2 - q^2$. Longitudinal and transverse response functions for electromagnetic and weak interactions are given by:

$$\upsilon_L = \left(\frac{Q^2}{q^2} \right)^2, \tag{1.10a}$$

$$v_T = -\frac{Q^2}{2q^2} + \tan^2 \frac{\theta}{2}, \tag{1.10b}$$

$$v_{T'} = \tan \frac{\theta}{2} \sqrt{-\frac{Q^2}{2q^2} + \tan^2 \frac{\theta}{2}}, \tag{1.10c}$$

where θ is the scattering angle of electron. A multipole expansion can be used to express $W^{(pv)}$ and F^2. Ignoring the mixing of nuclear states the expression for $W^{(pv)}$ and F^2.is given by [10].

$$F_L^2(q) = \sum_{J \geq 0} F_{CJ}^2(q) \tag{1.11a}$$

$$F_T^2(q) = \sum_{J \geq 1} \left\{ F_{EJ}^2(q) + F_{MJ}^2(q) \right\}, \tag{1.11b}$$

$$W_{AV}^L(q) = a_A \sum_{J \geq 0} F_{CJ}^2(q) \tilde{F}_{CJ}(q), \tag{1.11c}$$

$$W_{AV}^T(q) = a_A \sum_{J \geq 1} \left\{ F_{EJ}^2(q) \tilde{F}_{EJ}(q) + F_{MJ}^2(q) \tilde{F}_{MJ}(q) \right\}, \tag{1.11d}$$

$$W_{AV}^{T'}(q) = -a_V \sum_{J \geq 1} \left\{ F_{EJ}^2(q) \tilde{F}_{EJ_5}(q) + F_{MJ}^2(q) \tilde{F}_{MJ_5}(q) \right\}, \tag{1.11e}$$

CJ, EJ and MJ stands for Coulomb, electric and magnetic currents respectively and subscribe 5 if for the axial current. The details of multipole expansion can be found in [13] and [14].

1.5 Neutron Density and Parity Violation

There are some examples of measurements of neutron densities using different techniques given in [15]. Coulomb energy differences were used to get the neutron radii [16] but it is sensitive to isospin violating interactions. Proton nucleus scattering [17] are sensitive to surface and interior neutron densities. Stripping reactions (p,d) and (d,t) are used to get neutron densities but at large radius it is sensitive to the tail in the neutron density[18].

Parity violating scattering of electron from a nucleus gives model independent measurement of neutron densities. In low momentum transfer regime the Z^0 bosons mainly couples to neutron because weak charge of neutron $Q_W^n = -1$ is much larger than the weak charge of proton $Q_W^p = 1 - 4\sin^2\theta_W \approx 0.075$ where θ_W is Weinberg angle. In a scattering of an electron by a nucleus the potential between an electron and a nucleus is given by

$$V(r) = \int d^3r' \left(\sum \langle \psi_p^\dagger(r)\psi_p(r)\rangle\right) \Big/ |r - r'| +$$
$$\gamma_5 \frac{G_F}{2^{3/2}} \left\{(1 - 4\sin^2\theta_W)\left(\sum\langle\psi_p^\dagger(r)\psi_p(r)\rangle\right) - \left(\sum\langle\psi_n^\dagger(r)\psi_n(r)\rangle\right)\right\},$$

$$(1.12)$$

Two summations in expression of axial vector potential are proton and neutron point densities. Parity violation gives the observeable magnitude of axial vector, the second term in equation 1.12. Parity violating asymmetry of differential cross sections for left and right handed electrons is given by:

$$A_{PV} = \frac{G_F Q^2}{4\pi\alpha\sqrt{2}}\left[1 - 4\sin^2\theta_W - \frac{F_n(Q^2)}{F_p(Q^2)}\right], \tag{1.13}$$

Where $F_n(Q^2)$ and $F_p(Q^2)$ are neutron and proton form factors given by

$$F_n(Q^2) = \frac{1}{4\pi}\int d^3r\, j_0(Qr)\rho_n(r), \tag{1.14}$$

$$F_p(Q^2) = \frac{1}{4\pi}\int d^3r\, j_0(Qr)\rho_p(r), \tag{1.15}$$

$\rho_n(r)$ and $\rho_n(r)$ are neutron and proton density given in equation 1.12. As we know that $1 - 4\sin^2\theta_W$ is small so the parity violating asymmetry depends upon the ratio of neutron form factor to the proton form factor arising from axial vector potential. So parity violation gives a clean measurement of neutron distribution in the atom.

In a very recent paper [19] the values of parity violating asymmetry and the resulting values of neutron radius and neutron skin are computed in distorted wave Born approximation at PREx kinematics using 47 mean field models. These values are given in following tow figures:
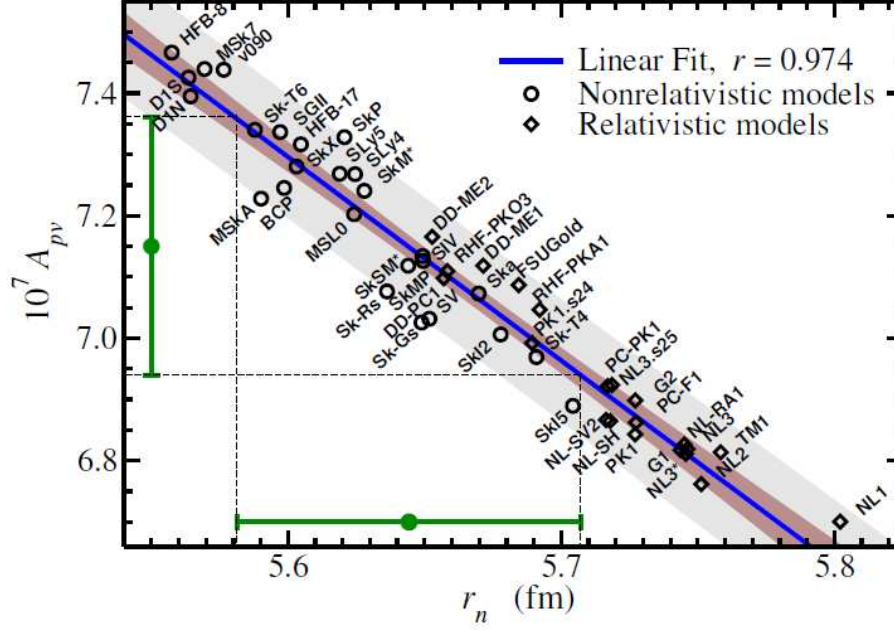
FIG. 1.2: Parity violating asymmetry v/s neutron radius for different MF interactions.

In the figures 1.2 and 1.3 the authors assumed a value of 0.715 for A_{PV} with 3% error given by green dot and green error bar. The linear fit for fig 1.2 is $A_{PV} = 25.83 - 3.31 r_n$ and linear fit for fig 1.3 is $A_{PV} = 7.88 - 3.35 r_n$.

1.6 Analyzing Power

The electron beam we have in hall A is not 100% longitudinally polarized. Small transverse polarization is a potential source of systematic error. This transverse polarization can give rise to false asymmetry. The qualitative difference of cross sections for electrons polarized transversed to the scattering plane going into left
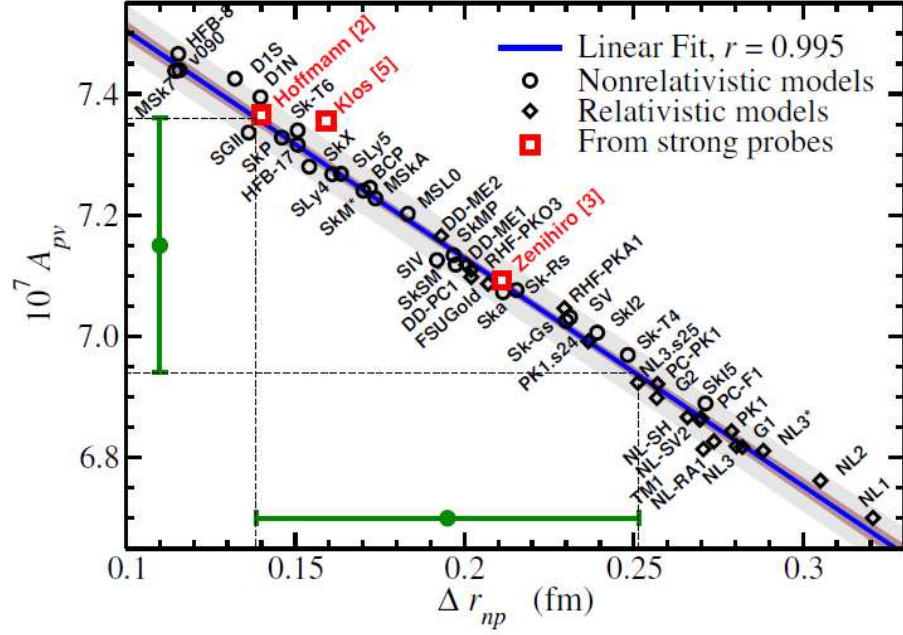
FIG. 1.3: Parity violating asymmetry v/s neutron skin for different MF interactions.

HRS and right HRS is known as analyzing power A_n. In first Born approximation A_n vanishes so a non zero value of analyzing power is related to two photon exchange. First in [20], it was assumed that ground state of the target nucleus contribute to the order of $Z\alpha$ and each excited state contributes to the order of α but later in [21] it is calculated that dominant contribution is from the intermediates states. We can write analyzing power as:

$$A_n = \frac{\sigma_\uparrow - \sigma_\downarrow}{\sigma_\uparrow + \sigma_\downarrow}, \tag{1.16}$$

The scattering of electron from a spinless nuclei with one and two photon exchange terms included is given by

$$T = \frac{e^2}{Q^2}\bar{u}(k')\{m_e A_1 + A_2\gamma_\mu P^\mu\}u(k), \tag{1.17}$$

In equation 1.17 A_1 arises from two photon exchange and for elastic scattering we have $A_2^0 = 2ZF_N(Q^2)$. Using optical theorem and including two photon exchange

the analyzing power to the order of α is given by

$$A_n = -\frac{m_2}{\sqrt{s}}\tan\left(\frac{\theta_{cm}}{2}\right)\frac{ImA_1}{ZF_N(Q^2)}, \qquad (1.18)$$

The explicit expressions of ImA_1 for elastic and inelastic scattering are given in [21]

$$
\begin{aligned}
ImA_1^{elastic} =\ & \frac{Z^2\alpha}{\pi}\frac{Q^2}{Q^2 - \frac{(s-M^2)^2}{s}}\frac{s+M^2}{s-M^2} \\
& \times \int_0^{4E^2} dQ_1^2 \int_{Q_-}^{Q^+} \frac{dQ_2^2}{\sqrt{(Q_+ - Q_2^2)(Q_2^2 - Q-)}} \\
& \times \frac{Q^2 - Q_1^2 - Q_2^2}{2Q_1^2 Q_2^2} F_N(Q_1^2)F_N(Q_2^2),
\end{aligned}
\qquad (1.19)
$$

$$
\begin{aligned}
ImA_1^{inelastic} =\ & \frac{1}{4\pi^2}\frac{M}{E_{lab}}\int_0^{E_{lab}} d\omega\,\omega\,\sigma_\gamma N(\omega) \\
& \times ln\left[\frac{Q^2}{m^2}\left(\frac{E_{lab}}{\omega}-1\right)^2\right],
\end{aligned}
\qquad (1.20)
$$

Four momentum transfer are $Q_1^2 = -q_1^2$ and $Q_1^2 = -q_1^2$, where q_1, q_2 are incoming and outgoing photon momenta respectively. The analyzing power for the elastic scattering equation 1.19 and for the inelastic scattering equation1.20 is plotted v/s scattering angle θ_{cm}. The following figure taken from [21]
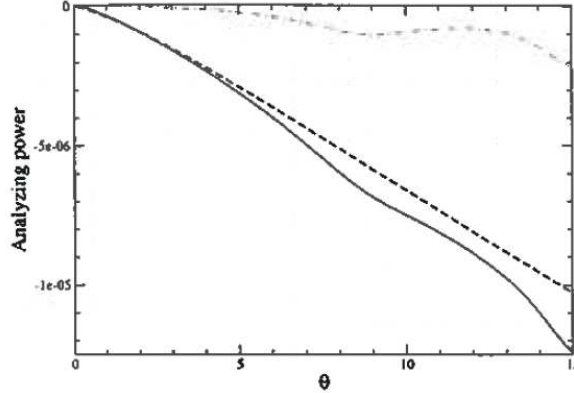
FIG. 1.4: Analyzing power for elastic and inelastic scattering v/s scattering angle.

In figure 1.4 elastic analyzing power is dashed-doted line, inelastic analyzing power is dashed line and solid line is sum of the two for ^{208}Pb at PREx kinematics. These contributions to parity violating asymmetry from analyzing power can be large so during the PREx we made special measurements to see the size of transverse polarization. Left and right transverse polarization are equal and opposite so the transverse polarization effects cancel each other. Transverse polarization measurements are shown in chapter 4.

1.7   Uncertainties to Parity Violating Asymmetry

Although parity violating gives a clean measurement of neutron density but still we need to check the possible corrections. A brief summary of the possible corrections is given here. The details of these corrections can be found in [15]. The largest piece of corrections comes from coulomb distortions. The other important corrections are strangeness, neutron electric form factors, parity admixtures, dispersion corrections, meson exchange currents, shape dependence, isospin admixtures, radiative corrections, role of excited states and the effect of target impurities. All these corrections are small and measurement of parity violating asymmetry is clean.

1.7.1   Coulomb Distortions

The electromagnetic interactions while the nucleus remains in its ground state are Coulomb distortions. Coulomb distortions are of the order of $Z\alpha/\pi$ where Z is the number of protons in nucleus. The accurate calculations of Coulomb distortions are given in [22]. A numerical code ELASTIC is used to solve partial wave Dirac equation numerically and weak cahrged density is assumed to have same spatial distribution as the charge density. Three results of calculation for Coulomb distortions relevant for PREx are shown in figure 1.5 from [22].
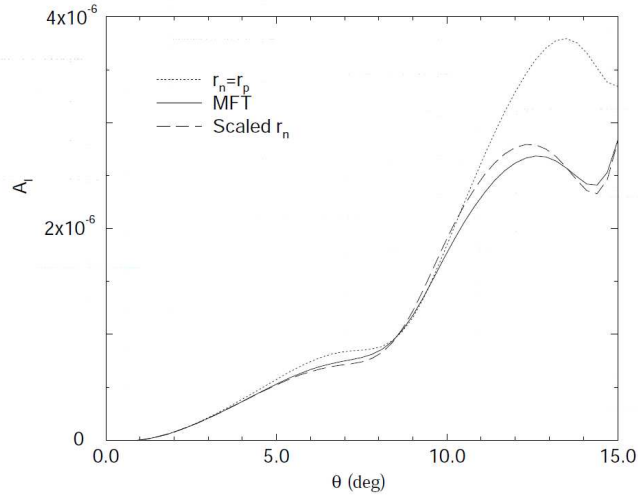
FIG. 1.5: Parity violating asymmetry v/s scattering angle θ.

Figure 1.5 shows the parity violating asymmetry v/s. scattering angle for forward angles at energy 850 MeV. Weak density and three parameter Fermi charge density are assumed to be same. Weak density and three parameter Fermi charge density are shown by dotted curve (please see ref 9 of [22]). Relativistic mean filed(MFT) charge densities and weak densities are shown by solid curve [23]. A scaled version of three parameter Fermi charge density is used for dashed line. Weak density for relativistic mean filed(MFT) is given by:

$$\rho_W(r) = \int d^3r' G_E(|r - r'|)[-\rho_n(r') + (1 - 4\sin^2\theta_W)\rho_p(r')], \qquad (1.21)$$

where in equation 1.21 ρ_n and ρ_n point densities for neutron and proton and $G_E(r) \approx \frac{\Lambda^3}{8\pi}e^{-\Lambda r}$ and $\Lambda = 4.27 Fm^{-1}$. Strange quark contribution, neutron form factor and meson exchange currents are neglected for $\rho_W(r)$. A value of $\sin^2\theta_W = 0.23$ is used.

The weak density for scaled version of the three parameter Fermi charge density is given by:

$$\rho_W(r) = -[\frac{N}{Z} + 4\sin^2\theta_W - 1]\lambda^3\rho(\lambda r), \qquad (1.22)$$

In equation 1.22 the scaled parameter $\lambda = 0.9502$.
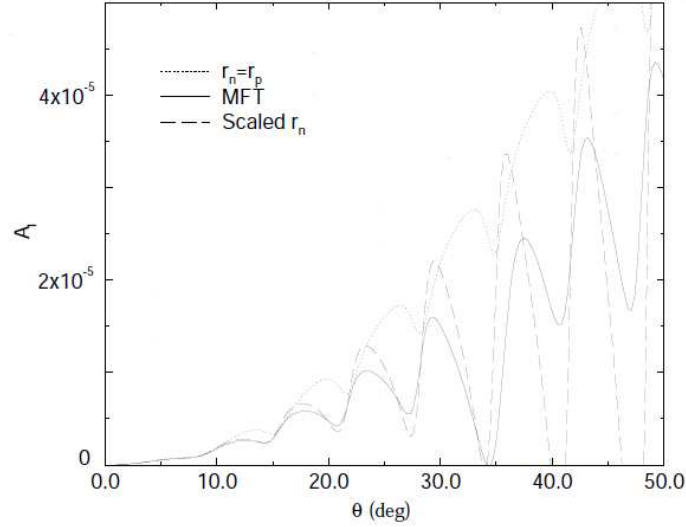
FIG. 1.6: Parity violating asymmetry vs scattering angle θ for large forward angle scattering.

Figure 1.7 is same as Figure 1.5 except it shows the parity violating asymmetry for larger scattering angles.

Figure 1.7 shows the charge and weak densities of ^{208}Pb vs. radius. Solid and dotted curves at the bottom are charge densities for relativistic mean field theory and three parameter Fermi fit to the elastic scattering. Upper three curves are weak densities and dashed curve is scaled version of three parameter Fermi fit.

These calculations give significantly large corrections to parity violating asymmetry. Still with these distortions the experiment is feasible when we measure the asymmetry around six degree.
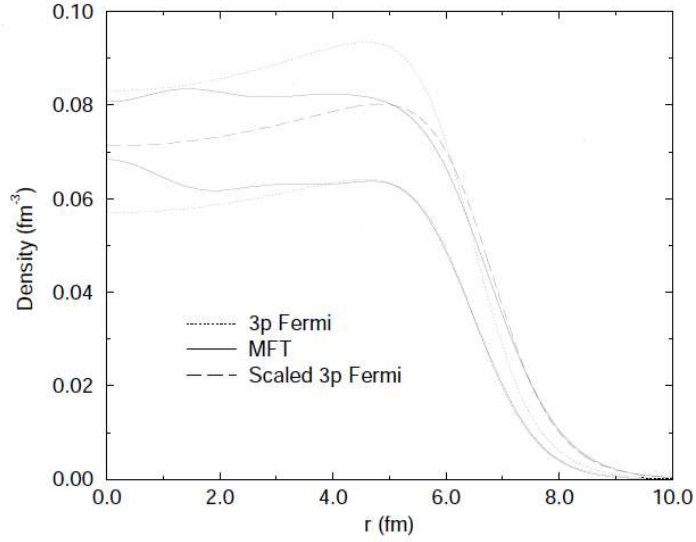
FIG. 1.7: Weak density and charge density of ^{208}Pb v/s radius.

1.7.2 Strangeness Correction

Point density of neutron is closely related to weak radius of neutron. If we consider the strange quark contribution then the expression for weak charge density is given by

$$\rho_W(r) = 4 \int d^3 r' \left[G_n^Z(r') N \rho_n(|\mathbf{r} - \mathbf{r}\prime|) + G_p^Z(r') N \rho_p(|\mathbf{r} - \mathbf{r}\prime|) \right], \tag{1.23}$$

where proton and neutron form factors(G_p^Z, G_n^Z) are given by

$$G_p^Z = \frac{1}{4} \left[(G_p(1 - 4\sin^2\theta_W) - (G_n + G_s) \right], \tag{1.24}$$

$$G_n^Z = \frac{1}{4} \left[(G_n(1 - 4\sin^2\theta_W) - (G_p + G_s) \right], \tag{1.25}$$

Solving equation 1.23 for ^{208}Pb ($R_n \approx 5.50$ and $\sin^2\theta_W = 0.23$) and assuming that neutron radius is much larger than the difference of neutron and proton weak radius ($R_n - R_p$):

$$R_W = R_n + 0.055(R_n - R_p) + 0.061(\pm 0.002) - 0.0089(\pm 0.0003) - 0.011\rho_s, \quad (1.26)$$

The values 0.061 and -0.0089 are taken from [24] and strange form factor G_s is given by

$$G_s(Q^2) = \frac{\rho_s \tau}{(1 + 4.97\tau)^2}, \quad (1.27)$$

where $\tau = Q^2/4M^2$. So it shows that the correction due to strange quark is less than 1% if $|\rho_s| < 5$. This conditon on ρ_s is already established by two previous experiments HAPPEX[25] and SAMPLE[26]. Combining the results of HAPPEX and SAMPLE gives us

$$0.011\rho_s = -0.0043 \pm 0.021 fm, \quad (1.28)$$

According to equating 1.33 the correction from strangeness is 0.4% and we can make a clean measurement of neutron density in ^{208}Pb.

1.7.3   Inelastic Scattering

In principle the contribution to parity violating asymmetry from inelastic scattering is small because the inelastic scattering cross section at low Q^2 is very small as compared to the elastic scattering cross section. ^{208}Pb has its first excited state at energy 2.6 MeV and its spin parity is 3^- which is a collective density oscillation [27] state. Parity violation asymmetry with nucleus in spin excited sate J is given by [10]

$$A_{PV}^J = \frac{G_F Q^2}{4\pi\alpha\sqrt{2}}\left[4\sin^2\theta_W - 1 + \frac{F_n^J(Q^2)}{F_p^J(Q^2)}\right], \quad (1.29)$$

where $F_n^j(Q^2)$ and $F_n^j(Q^2)$ are neutron and proton form factors and we can express them in terms of neutron and proton transition densities $\rho_n^{tr}(r)$, $\rho_p^{tr}(r)$ respectively

$$F_n^j(Q^2) = N \int r^2 dr j_J(qr)\rho_n^{tr}(r) \tag{1.30a}$$

$$F_p^j(Q^2) = N \int r^2 dr j_J(qr)\rho_p^{tr}(r) \tag{1.30b}$$

If we expand transition densities in term of Bessel function provided the Q^2 is small and collective density oscillation $(\frac{F_n^j(Q^2)}{F_p^j(Q^2)})$ is a deformed sate of ground state[27], then we have

$$\frac{F_n^j(Q^2)}{F_p^j(Q^2)} \approx \frac{\alpha_j^n N}{\alpha_j^p N}(\frac{R_n}{R_p})^J, \tag{1.31}$$

Now in the first excited state of ^{208}Pb neutrons and protons can either oscillate in phase ($\alpha_j^n \approx \alpha_j^p$, isoscaler) or they can oscillate out of phase ($\alpha_j^n \approx$ - α_j^p, isovector). Solving equation 1.29 for isoscaler state and assuming that $R_n \approx R_p$ we find that contribution of isoscaler excited state of ^{208}Pb nucleus is similar to elastic asymmetry. Before solving 1.29 for isovector excited state we must know that there are no distorted wave calculations but it is assumed that coulomb effects are same to the inelastic and the elastic scattering. Then solving equation 1.29 for isovector excited state with $R_n \approx R_p + 0.2$ and $q = 0.45 fm_{-1}$ give us:

$$A(3^-) \approx 0.83 \pm 0.29 \pm 0.03 \times 10^{-6}, \tag{1.32}$$

In equation 1.32 the first error and second error comes from the assumption that R_n is known to 1%. So we can see that inelastic scattering contributions get reduced by the facts that isoscaler asymmetry is smilier to electing scattering asymmetry and also that the inelastic cross section is much smaller than elastic cross section. As

given by [28], the scattering amplitude for inelastic scattering of first excited state of ^{208}Pb at energy 850 MeV is 0.35 mb/sr where as the elastic scattering amplitude at energy 850 MeV and scattering angle six degree is 1140 mb/sr.

1.7.4 Parity Admixture

As shown by [29], the parity admixture will not give a contribution to parity violation asymmetry as long as the initial and final states are in in spin zero state. So parity admixture corrections is negligible.

1.7.5 Meson Exchange Current

Mesons can carry the weak charge but they can carry it for distances much smaller than the radius of neutron R_n. So meson exchange current(MEC) does not change the neutron radius measurement via parity violation. For further details of MEC please see [30]

1.7.6 Dispersion correction

Multiple scatterings of electrons with ^{208}Pb nucleus where nucleus is in any of the intermediate excited states, give rise to dispersion corrections. This dispersion correction is negligible because the ratio of the coherent sum of the elastic cross section to the incoherent sum of inelastic transitions is α/Z which is negligible.

1.7.7 Surface Thickness

Since Q^2 is not zero so the dependence of measurement of weak radius of neutron on surface thicnkness is very small if not zero. In order to understand that how relevant is the role of neutron distribution in a nucleus to extract the neutron radius using equating 1.23, let us consider the Wood Saxon model.

$$\rho_W(r) = \frac{\rho_0}{\exp\left[(r - c)/z\right] + 1}, \tag{1.33}$$

where c is radius parameter and $z \approx 0.55$ is thickness parameter. In order to get R_W with 1% we need to know z with $\pm 0.14 (25\%)$ at $Q^2 = 0.0008 \ GeV^2$ and since surface thickness of the weak density is known better than 25% as discussed in [15]. So surface thickness makes small corrections to the measurement of neutron radius.

1.7.8 Isospin Violation Correction

In heavy nucleus the proton radius is smaller than neutron radius so this shows that isospin symmetry is broken at some level. It is shown by [31] that the difference in matrix element of up quark in proton and matrix element of down quark in neutron makes very small corrections.

1.7.9 Target Impurities

Lead target of PREx is sandwich between two diamond foils and during the experiment we took separate measurements for carbon asymmetry. These measurements are small and the details are given in chapter4.

1.8 Important Results of PREx

PREx has significant effect on variety of Fields, from nuclear structure to astro physics.

1.8.1   Atomic Parity Non-Conservation

First we discuss the atomic parity non conservation. For an atomic parity non conservation measurement an isoscaler distribution of nuclear density is assumed i.e. $\rho_n(r) = \rho_p(r)$. But precisely speaking we know that $\rho_n(r) \neq \rho_p(r)$ so there is correction to the weak charge

$$Q_W = Q_W^{St.Mod} + \Delta Q_W^{n-p}, \tag{1.34}$$

In atomic theories neutrons and protons are treated same so equation 1.35 can be written approximately:

$$Q_W = N(1 - \frac{q_n}{q_p}), \tag{1.35}$$

If we consider the same distribution for neutron and proton then ΔQ_W^{n-p} is zero and here we need elastic scattering of parity violating electrons to show the effect of non zero ΔQ_W^{n-p}. For example the Cs experiment [32] gives the value of $Q_W = -72.06(0.28)_{expt}(0.034)_{atomic-theory}$ which is 2.5σ away from theory [33] $Q_W^{Standard-Model} = -73.20(0.13)_{theory}$. This is because, for the experimental values the atomic theory calculations [34, 35] were used which do not consider the non zero value of ΔQ_W^{n-p}. If we know the radius of neutron with at least 2% of error then we can reduce the nuclear structure uncertainties to ± 0.13.

1.8.2   Nuclear Symmetry Energy

A brief discussion about neutron skin measurement and the symmetry energy around normal density(L) is given in [19]. Thicker the neutron skin is, larger the value of symmetry energy around normal density is. A 3% error in A_{PV} with central value 0.715, will give us $L = 64 \pm 39(\text{MeV})$. Following figure shows the value's of L and neutron skin measured by different MF models:
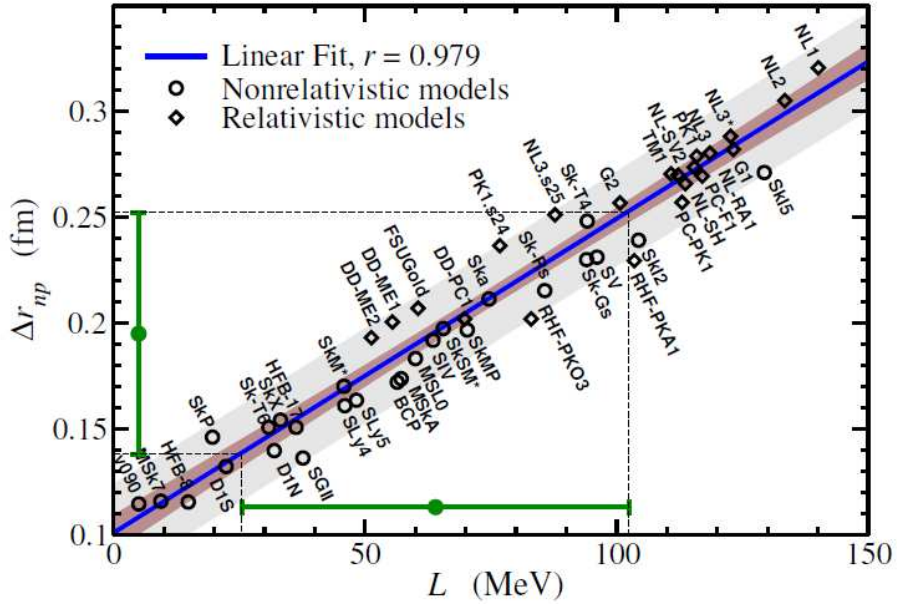
FIG. 1.8: Neutron skin vs asymmetry energy.

1.8.3   Neutron Density and Astro Physics

The measurement of neutron density parameters many areas of astro physics for example, structure of neutron rich matter [36][37], study of neutron stars [38][39], giant flares[40] and gravitational radiation[41].

1.9   Summary of Specific Responsibilities of the Author

The electron beam in Jefferson lab is not 100% polarized so we need to normalize the parity asymmetry with a measurement of the beam polarization. A cutting edge data acquisition system based upon Jlab custom build F250 flash ADC was installed for Hall A Moller polarimeter just before HAPPEX III in September 2009. In addition to the analysis of the experimental data of PREx It was the responsibility

of the author to make the Flash ADC data acquisition system operational and get results in good agreement with the old DAQ of the Hall A Moller polarimeter. This responsibility included the hardware setup of the Flash ADC DAQ and then the analysis of the Flash ADC data. It required a lot of lab tests with artificial beam signals generated by a pulser and check the stability of the Flash ADC. During the running periods of HAPPEX III and PVDIS the Flash ADC DAQ was tested with real beam on signals and many improvements were made. For example first two modules of FADC were not triggering on scintillator channels. So we requested the DAQ group to upgrade the FPGA logic of FADC. During the PREx run we made sure that the quality of data is good by continually checking the online data analysis. I also worked as weekly analysis coordinator do the offline analysis for daily group meetings. Along with parity analysis I also analyze the data of Flash ADC DAQ of hall A Moller polarimeter and showed that the results of old and Flash ADC DAQs agree.

CHAPTER 2

Experimental Design

2.1 Accelerator

PREx experiment is performed at hall A of Thomas Jefferson National Accelerator Facility(TJNAF) in Newport News, VA. In PREx we measured the parity violating asymmetry which is of the order of half part per million (ppm). Its very difficult to measure such a small asymmetry so we must keep the systematics under controlled. TJNAF is one of the best accelerator facilities around the globe to probe in nucleus and check standard model precisely. Electrons are injected into the accelerator at injector building. Superconducting radio frequency cavities are used in two linear accelerators to accelerate the electrons and it takes 5 passes to reach the energy of 6 GeV. The energy spread in the beam is $\Delta E/E < 10^{-4}$ and the fundamental RF frequency of the beam is 1.467 GHz. Different beam parameters like beam position, beam current and beam energy are carefully monitored. TJNAF can deliver a beam of 200 uA to three experimental halls A, B and C. Three polarimeters are used to measure the beam polarization, Mott Polarimeter is in the injector building and two polarimeters, Moller and Compton are in the hall A. PREx target

is Lead block sandwich between diamond foils for thermal conductivity. Electrons are scattered at an angle of 5.8 degree from target and focused at PREx detectors by two HRS. This chapter describes the important pieces of experimental setup. Following diagram shows the overall locations of different parts of accelerator. This diagram is taken from accelerator divisions' website.
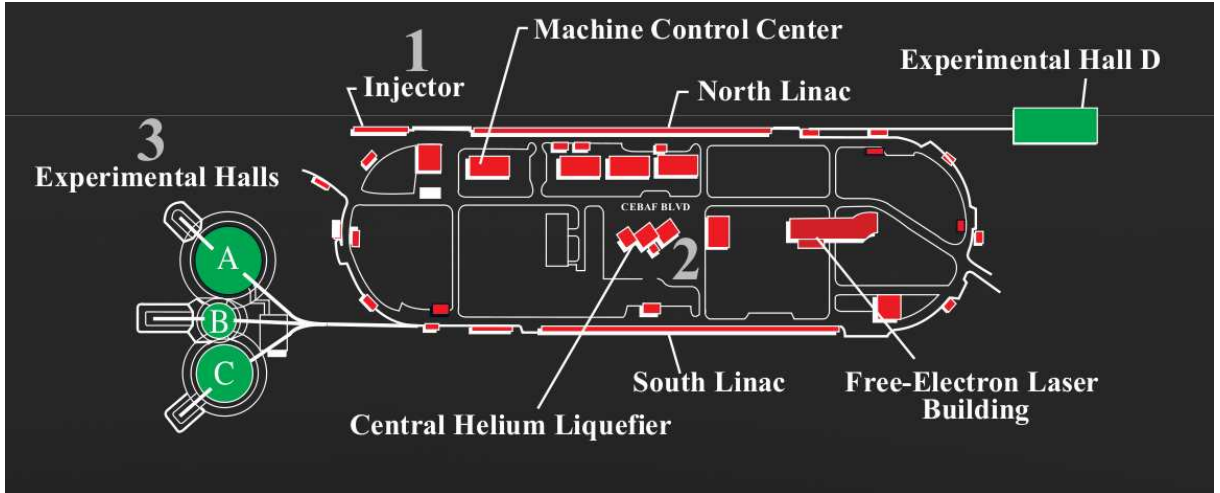
FIG. 2.1: Accelerator and experimental halls.

2.2 Polarized Source

Production of longitudinally polarized electrons is shown shown in fig2.1. First a LASER is generated with a longitudinal polarization. Then with the help of a Pockels cell linear polarization of this LASER is converted into left and right transverse polarization. The transversely polarized LASER optically pumps the photo-cathode. Photo-cathode is made of a strained GaAs crystal. Electrons in valance band of GaAs crystal moves to conduction band and then injected into the accelerator by keeping the GaAs crystal at a bias potential of -100kV.

2.2.1 Laser System

A fiber LASER system is used to produce the polarized electrons. Fiber laser starts with a dinode which is biased with a dc current and a RF wave is applied to this laser. The balacne between dc power and RF wave must be maintained to perform the gain-switching technique. Pulse of fiber laser is 30ps long and frequency is 499MHz. A second harmonic generator assembly is used to convert the 1560nm laser light to 780nm laser by making its frequency double. A 780nm laser light is desired to run the photo emissions gun. There are total three laser systems, each for one experimental hall. Beam intensity in hall A is controlled by an attenuator in the path of laser light. This attenuator consists of rotatable half-wave plate and a linear polarizer. Following schematic diagram(taken from [42]) shows the different components of laser system for three experimental halls.
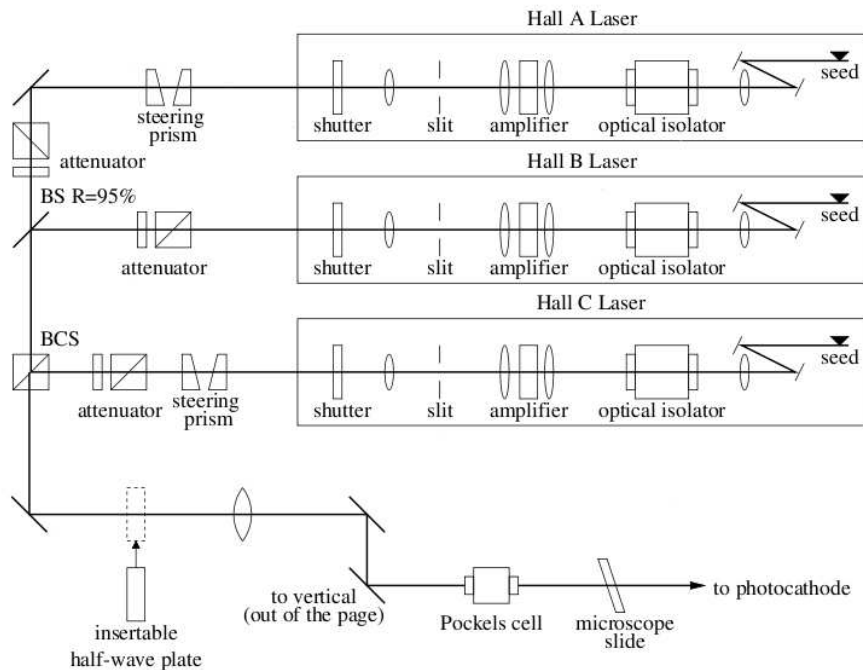
FIG. 2.2: Laser System.

Each laser is 120° out of phase with others. After the attenuator electron

beam passes through an insert-able half wave plate and the Pickles cell. Pickles cell converts the linearly polarization into circular polarization. Circularly polarized light hits the GaAs crystal cathode and with the photo emission effect polarized electrons are injected into the accelerator.

2.2.2 Insertable Half Wave Plate

Insertable Half Wave Plate(IHWP) is an optical device upstream of Pockels cell and it rotates the orientation of beam polarization by $90\,^\circ$. The fast angle of IHWP is aligned at $45\,^\circ$ with respect to the linear polarization of the laser. The idea behind using the IHWP is that if there is any electronic pick up which co-related to left or right helicity state of electron beam then we reverse the helicity state with an optical device without changing the electronics. Now when we add two sets of data, with and without IHWP, the electronic pick up will cancel out. A set of data with one state of IHWP is known as Slug.

2.2.3 Pockels Cell and PITA effect

A Pockels cell is a electro-optic device which acts as a quarter wave retarder and converts the linearly polarized light into circularly polarized light. A voltage of $\pm 2.5 kV$ is applied to Pockels cell at the rate of 120Hz. Polarity reversal of Pockels is pseudoramdomly selected. If Pockels cell is perfectly aligned then we have 100% circular polarization but it is not the case so we are left with a little bit of linear polarization. Now when this laser light with a small linear polarization incident non-normally on any optical device which has non zero analyzing power will result in in-plane and out of plane transmission of small linear polarization. This will result in an intensity asymmetry of laser light because left handed and right handed circular polarizations have their linear components oriented differently for each other. This

helecity co-related intensity difference is known as PITA effect[43]. This asymmetry can be controlled by making a correction to applied potential to Pockels cell . The phase shift induced by Pockels cell for left and right circularly polarized light is given by:

$$\delta_R = -(\frac{\pi}{2} + \alpha) - \Delta, \tag{2.1a}$$

$$\delta_L = -(\frac{\pi}{2} + \alpha) - \Delta, \tag{2.1b}$$

where α is symmetric and Δ is antisymmetric off sets in the phase shift. For a perfect circular polarization we have $\alpha = \Delta = 0$. For asymmetry measurement α cancels out and we are sensitive to Δ only. Let us assume that x' and y' are the orthogonal transmission axis of the optical analyzer with $T_{x'}$ and $T_{y'}$ are their transmission factors respectively and x' makes an angle θ with the Pockels cells' fast axis. Then the intensity asymmetry is given by [44]:

$$A = \frac{\epsilon}{T} \cos 2\theta \times (\Delta - \Delta^0), \tag{2.2}$$

Where $\epsilon = T_{x'} - T_{y'}$ and $T = T_{x'} + T_{y'}$. The ratio $\epsilon/T << 1$ is the analyzing power. Δ^0 is the offset in phase shift because of the residual birefringence in Pockels cell. The quantity $\frac{\epsilon}{T} \cos 2\theta$ is PITA slope and we can see that intensity asymmetry T is linear to Δ. Following is the schematic diagram of PITA effect. So we can adjust the Δ by changing the applied voltage to Pockels cell by an amount of $V_\Delta = \Delta V_{\frac{\lambda}{2}}/\pi$. Where $V_{\frac{\lambda}{2}}$ is the voltage required to provide a half wave retardation. A PITA scan shown in fig 2.4 is taken from $HALOG\#321889$. During this scan insertabe half wave place is IN, rotatable half wave plate is at at 2350 and Pockels cell voltages are 6.123/9.131. PITA slope $= -574 ppm/V (units of PC)$.
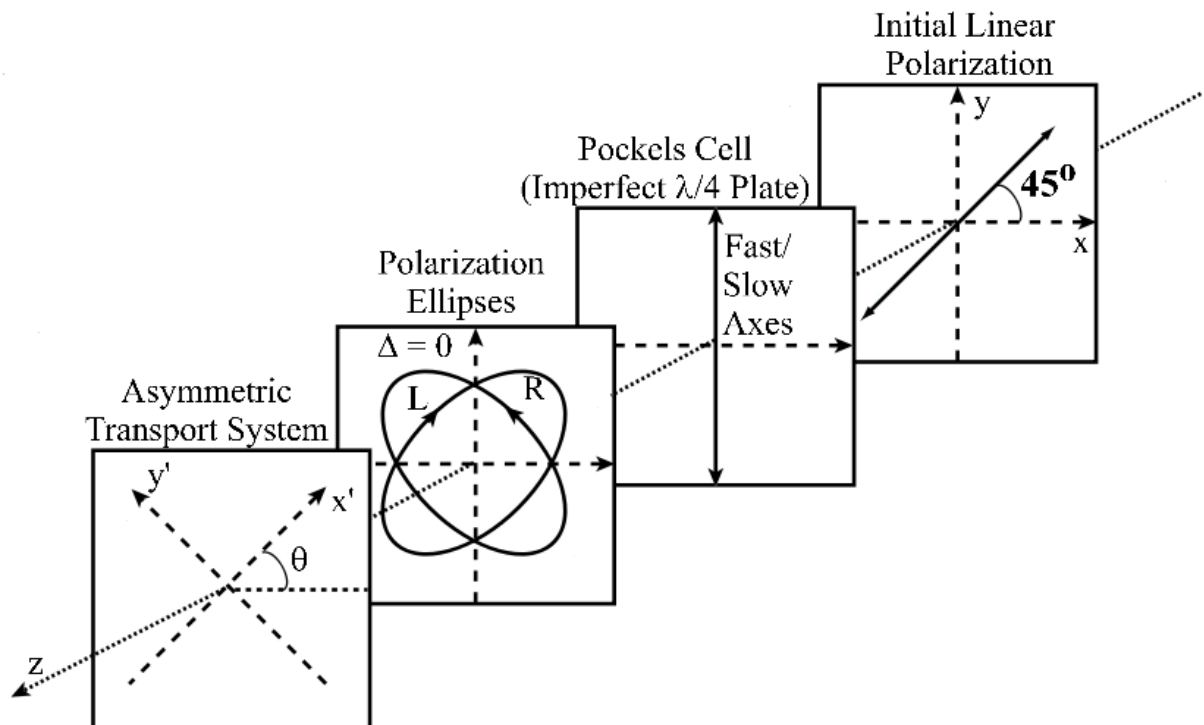
FIG. 2.3: PITA effect.
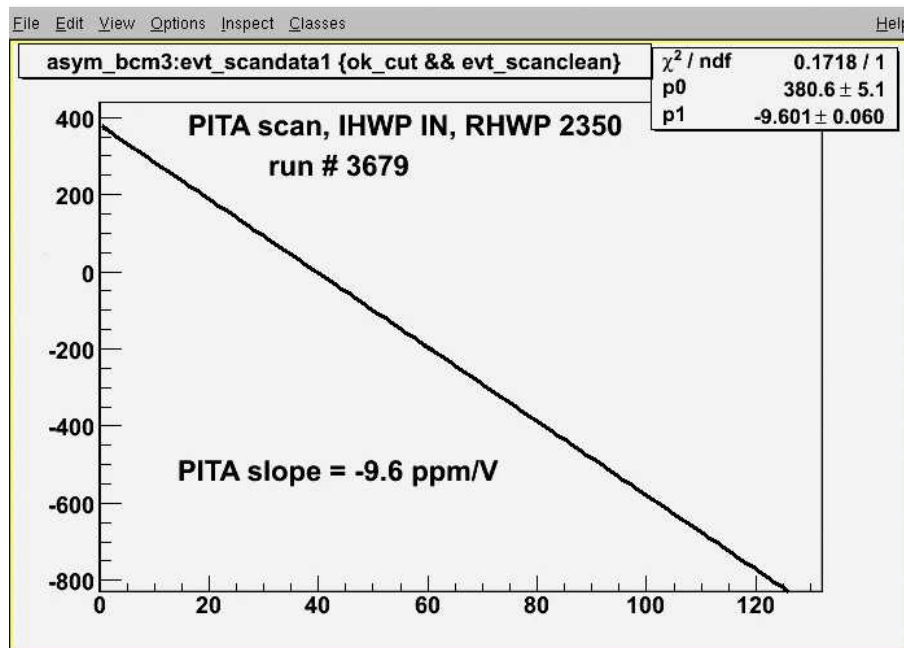
FIG. 2.4: PITA scan.

PITA feedback

The PITA scan shown in fig 2.4 has a linear relationship between charge asymmetry and voltage applied to Pockels cell. We also know that there is a linear relationship between charge asymmetry and phase offset Δ given by equation 2.2, so we can construct a feedback system to reduce the PITA effect. We periodically check the charge asymmetry with the help of a beam current monitor and make corrections to the Pockels cell's high voltages so that the charge asymmetry is almost zero. Parity DAQ checks the charge asymmetry after every 2500 window pairs. We call this 2500 window pairs a mini run. So the voltage correction applied to n^{th} mini run is given by:

$$V_\Delta^n = V_\Delta^{n-1} - (A_I^{n-1}/M), \tag{2.3a}$$

$$V_R^n = V_R^0 + V_\Delta^n, \tag{2.3b}$$

$$V_L^n = V_L^0 + V_\Delta^n, \tag{2.3c}$$

Where M is the PITA slope. V_R^0 and V_R^0 are the initial Pockels voltages for right and left helicity states such that $V_R^0 \approx -V_R^0$.

2.2.4   Rotatable Half Wave Plate

Equation 2.2 is a rather simple case. There are more optical elements in the path of polarized LASER beam before it hits the GaAs cathode. There is an IHWP and a vacuum window and each of these two have an analyzing power. IHWP and vacuum window can introduce some intensity asymmetry. If IHWP introduces a retardation of $\pi + \gamma$ and vacuum window induces birefringence β such that $\gamma \ll 1$ and $\beta \ll 1$ then we can write equation 2.2 as given by [44]

$$A_I = -\frac{\epsilon}{T}[(\Delta - \Delta^0)\cos{(2\theta - 4\psi)} - \gamma\sin{(2\theta - 2\psi)} - \beta\sin{(2\theta - 2\rho)}], \qquad (2.4)$$

where ψ and ρ are orientation angles of the IHWP and the vacuum window fast axes respectively as measured from the horizontal axis. With the help of rotatable half wave plate(RHWP) we can minimize the analyzing power effects from IHWP and vacuum window. RHWP can rotate the major axis of orientation of the polarization ellipses of circularly polarized laser beam with respect to the axis of analyzing power of GaAs.
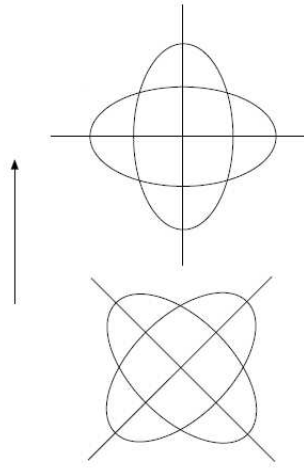
FIG. 2.5: Circular polarization ellipse and GaAs analyzing power axis.

In figure 2.6 arrow shows the direction of axis of analyzing power of GaAs crystal. As a standard procedure we measure the charge asymmetry as function of orientation of RHWP and call it RHWP scan. An example of RHWP is given below. This scan is taken from $HALOG\#310130$.

Practically we choose such an orientation of RASP that we have some value of PITA slope so we are sensitive to analyzing power and then PITA feedback can make correction to the Yokel's cells' voltage.
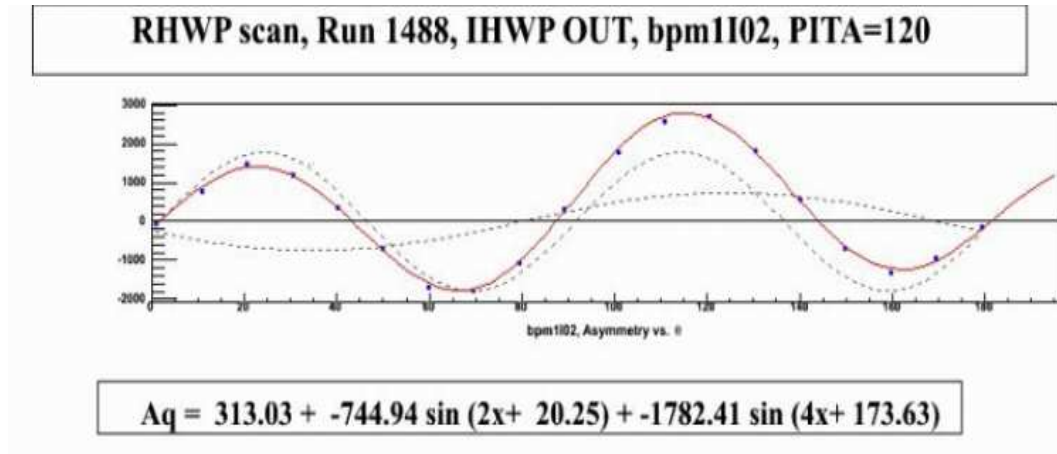
FIG. 2.6: RASP scan.

2.2.5 Gal's Cathode

First successful attempt to produce polarized electrons in the conduction band by the method of optical pumping is reported by G. Lampel[45]. Another break through is made by D. T. Pierce, F.Meier and P. Zurcher[46] with the use of GaAs crystal as a polarized source and the 45% polarization of electrons with high current detected. A strained-super lattice GaAs photo cathode is used in PREx and 89% polarization is measured. In a strained GaAs crystal a thin layer of GaAs is grown on GaAsP substrate. In a super-lattice strained Crystal used in Jefferson lab 14 pairs of GaAs and GaAsP are grown. Because of the lattice mismatch there is a strain between GaAs and GaAsP then this strain breaks the degeneracy in the valance band of GaAs. The valance band of GaAs is $P_{3/2}(m_j = \pm 1/2)$ and the conduction band is $S_{1/2}(m_j = \pm 1/2)$. Energy difference between valance band and conduction band is shown in figure 2.8, it also shows how left and right circularly polarized laser excites the electrons from valacne band to conduction band. Figure 2.9 shows the band structure of super-lattice strained GaAs crystal. These diagrams are taken from injector groups' website.

Now with a laser light of appropriate wave length the electrons can be moved
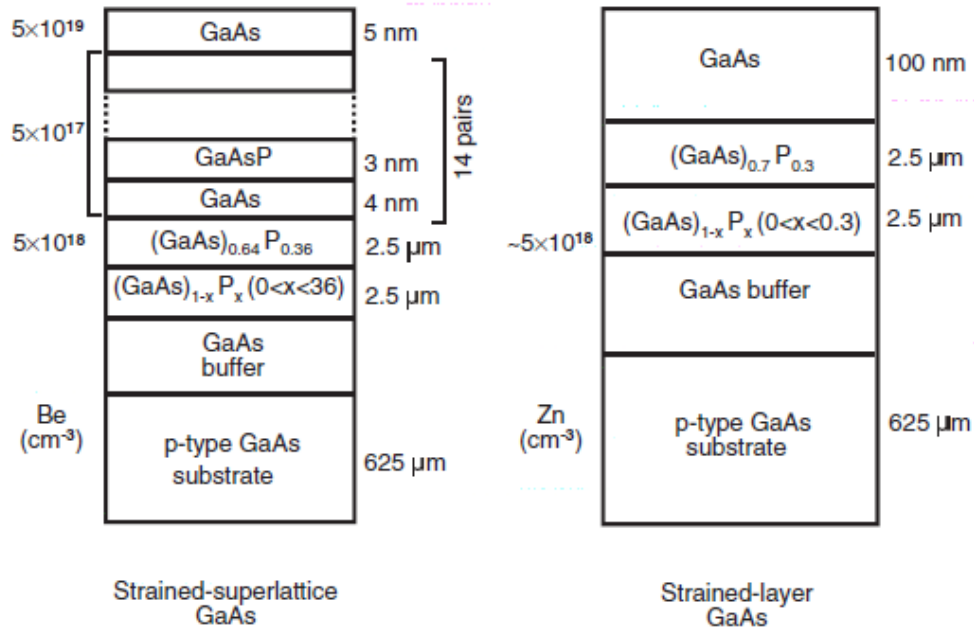
FIG. 2.7: Super-lattice strained GaAs crystal.

from valance band to conduction band, this is known as optical pumping. Left and right handed circularly polarized laser moves the electrons from valance band to $m_j = -1/2$ and $m_j = 1/2$ states respectively. A negative electron affinity is generated at the surface of GaAs crystal by a chemical treating process using Cesium. This negative electron affinity makes it possible to emit the spin polarized electrons from the conduction band. The difference between bulk GaAs crystal and supper-lattice GaAs crystal is given in [47] and the exact details of super-lattice GaAs cathode used in Jefferson lab can be found here [48]. A schematic diagram of strained GaAs crystal and super-lattice strained GaAS crystal is shown in figure 2.7. In figure 2.12 a schematics of laser system and photo cathode is shown.

2.3 Wien Filter

Other than IHWP there is another method to cahge the convention of left and right helicity states passively. A double wien filter is used during PREx. A Wien
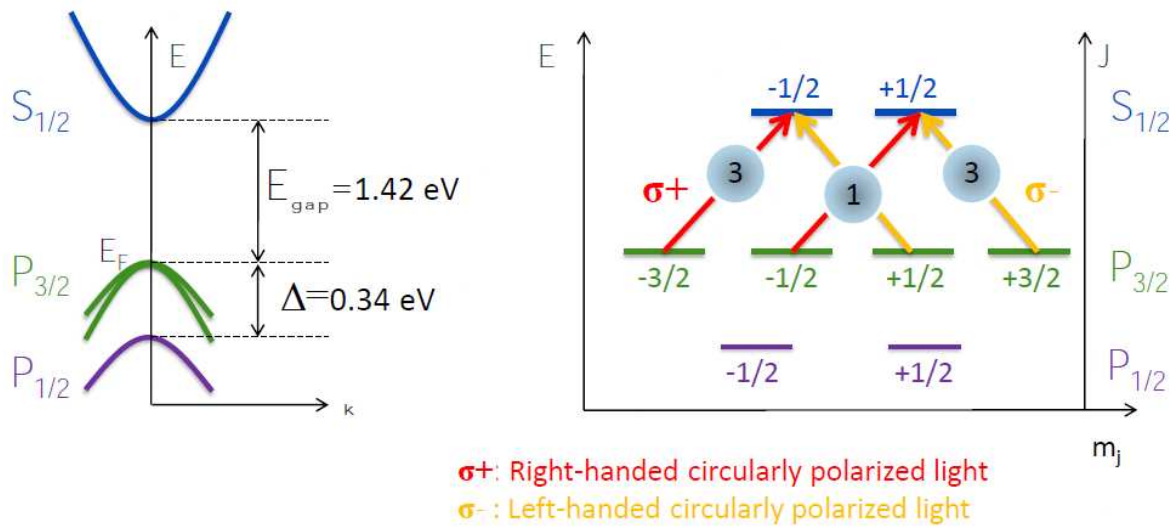
FIG. 2.8: Excitation of electrons by left(yellow) and right(red) circularly polarized light in Bulk GaAs crystal.
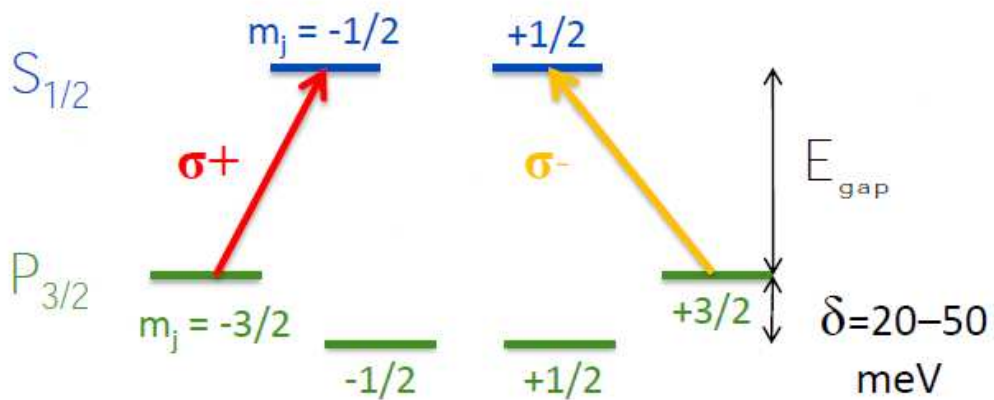
FIG. 2.9: Excitation of electrons in super-lattice strained GaAs crystal by left(yellow) and right(red) circularly polarized light.

filter is an electric device to rotate the spin of polarized electrons. A dipole magnet is used to rotate the beam polarization. In Win filter we apply an electric and a magnetic filed perpendicular to each other. Both fields are transverse to the beam motion. Strength of electric and magnetic filed is selected such that the net Lorentz force on electrons is zero.

$$F = q(\vec{E} + \frac{\vec{v}}{c} \times \vec{B}) = 0, \tag{2.5}$$

where $v = c\frac{E}{B}$. Since the net force is zero so polarization of the beam passing through wien filter changes by an angle η_{wien} without any deflection. Wien angel is dominated by electric field integral. A schematic diagram of wien filter is given below:
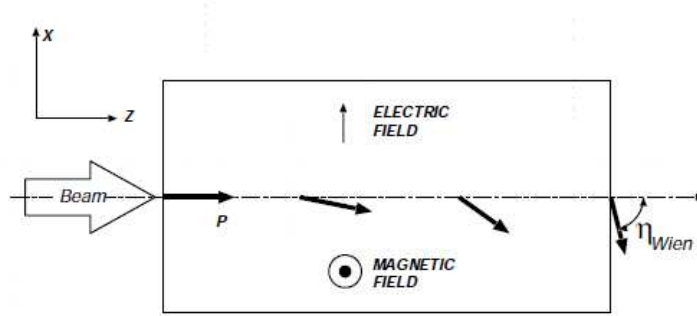
FIG. 2.10: Rotation of polarization in Wien filter.

A **Double Wien Filter** provides a $180°$ spin rotation which cancels the higher order helicity correlated beam asymmetries e.g. vertical polarization and spot size. Double wien filter rotates the spin as B but focuses as B^2. The convention of rotation in double wien filter is given in diagram2.11.

There is another very important role of wien filter. The circular arcs of accelerator and bending arc of the beam line of hall A can introduce a spin precession. The precession angle is given by
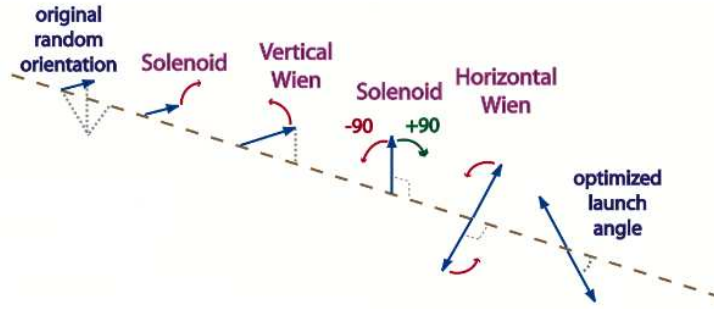
FIG. 2.11: Rotation of polarization in double Wien filter.

$$\chi = \gamma(\frac{g-2}{2})\Delta\theta, \tag{2.6}$$

where $\Delta\theta$ is the bend angle, g is electron g factor and $\gamma = (1 - v^2/c^2)^{-1/2}$. So with the help of wien filter we can adjust the initial spin precession such that when beam enters the hall A we get an optimum linear polarization.

A schematic diagram of polarized source and laser system is shown in figure 2.12
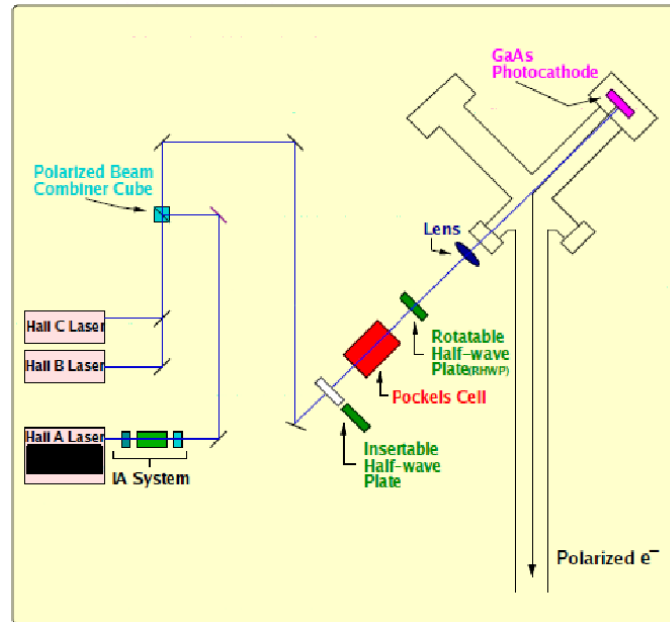
FIG. 2.12: Laser system, optical elements and photo cathode.

2.4 Polarimeters

Since the electron beam is not 100% polarized so the measured parity violating asymmetry is needed to be normalized by polarization to get the experimental asymmetry, $A^{exp} = A^{measured}/P_e$. Three polarimeters are available to measure the electron beam polarization. Mott polarimeter is in the injector building and Moller and Compton polarimeters are in the hall A. Moller and Compton polarimeters were planned to upgrade for PREx to measure the beam polarization with in 1% error. Mott polarimeter and Compton polarimters are discussed here. Moller polarimeter is described in chapter 3.

2.4.1 Mott Polarimeter

Mott scattering is the interaction between magnetic moment of the polarized electron(lepton) arising from its spin state and the orbital angular momentum of target atom. It was first calculated by Nevill Mott [49] and today it is used as a tool to measure the electron beam polarization. If $I(\theta)$ is the scattering amplitude for non polarized electron then Mott cross section can be written as

$$\sigma = \; I(\theta)[1 + S(\theta)\vec{P}.\hat{n}], \tag{2.7}$$

where $S(\theta)$ is the famous Sherman function and it describes how well the interaction differentiate between two helicity states of incoming electrons. Dependence of Sherman function upon scattering angle for various energies of incoming electrons is given in fig 2.13.

If $\vec{p}$ is the momentum of incoming electron and Ze is the charge of target nucleus then in the center of mass frame Mott scattering cross section is given by:
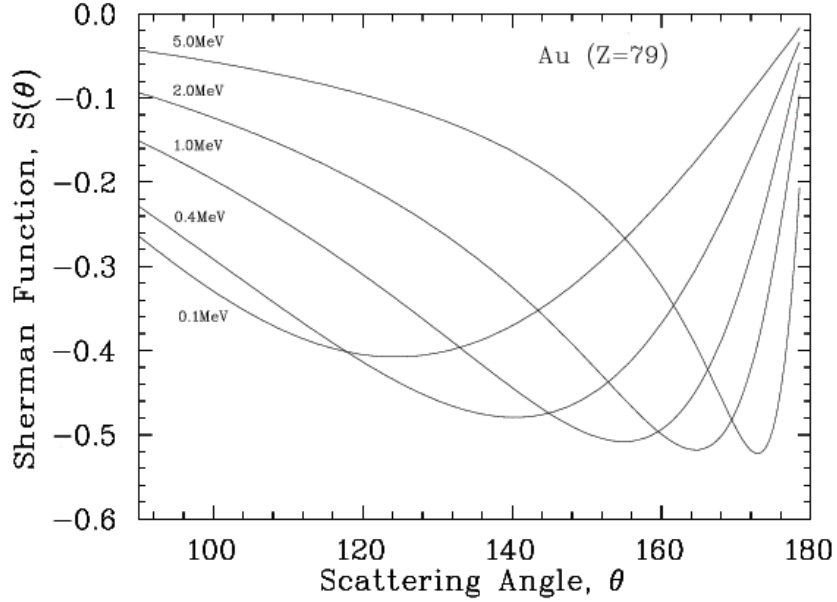
FIG. 2.13: Sherman function v/s scattering angle.

$$\frac{d\sigma}{d\Omega} = \frac{Z^2 e^4}{4(4\pi\epsilon_0)^2} \frac{1 - v^2 \sin^2\left(\frac{\theta}{2}\right)}{|\vec{p}|^2 v^2 \sin^4\left(\frac{\theta}{2}\right)}, \tag{2.8}$$

Measurement of beam polarization using Mott polarimeter requires to stop the beam delivery to hall A. Any measurement requires to stop the beam delivery to experimental target is called an invasive measurement. Mott parameter at the injector building of Jefferson lab operates at energy 5 to 10 MeV. It has four detectors located at positions to detect back scattered electrons at the angles of ±172.6 degree. Four detectors measure the counting asymmetry of back scattered electrons for horizontal(left-right) and vertical(up-down) configuration and we get the simultaneous measurement of x and y component of the beam polarization. With this we can infer the z component of the beam polarization. The targets are gold foils of varying thickness from 0.01μm to 5μm thickness. An empty target location is used to measure the target ladder backgoud. The analyzing power is measured by plotting the asymmetry for different thickness of the target and then extrapolating it to the thickness so it corresponds to the scattering from single atom. A schematic

diagram of Mott polarimeter is shown in figure 2.14.
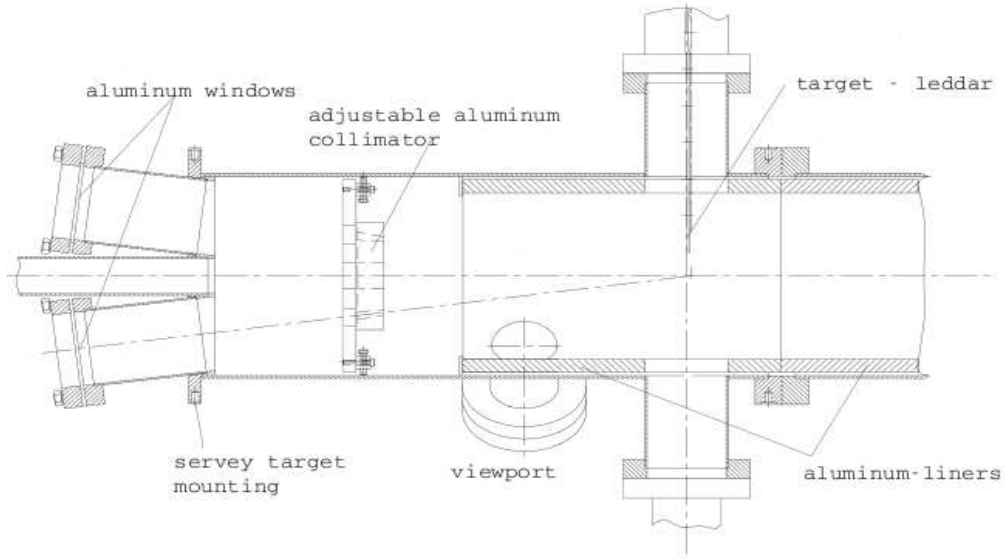
FIG. 2.14: Mott Polarimeter in accelerator building. Electron beam is going from left to right.

2.4.2 Compton Polarimeter

Compton polarimeter in hall A of Jefferson lab is a non invasive continuous measuring polarimeter. Only 1 out of 10^9 electrons undergo Compton scattering with polarized laser and the filed integral of magnetic chicane is zero so beam conditions remain almost the same. Compton scattering of longitudinally polarized electrons and circularly polarized photons ($\vec{e^-}\vec{\gamma} \to \vec{e^-}\vec{\gamma}$) take place in Fabry-Perot cavity. Back scattered photons are detected in a 6cm diameter and 15cm long GSO(Gd_2SiO_5) crystal. The response function of GSO crystal is measured and known. The Fabry-Perot cavity is upgraded for PREx to use low power green laser light ($\lambda = 532nm, k = 2.3eV$). Also as a part of upgrade an integrated data acquisition system is also commissioned. The old DAQ is a counting mode DAQ. A schematic diagram of Compton polarimeter is shown in figure 2.15.

As shown in figure2.15, electron beam enters from left and passes trough a
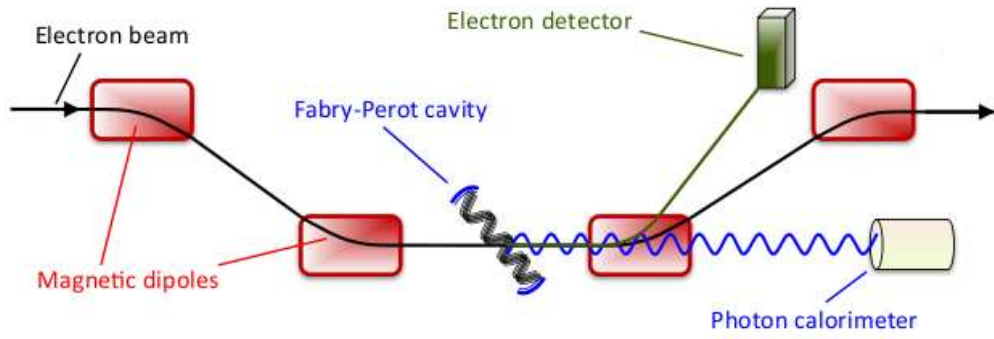
FIG. 2.15: Compton polarimeter. Electron beam is going from left to right.

magnetic chicane. Compton scattering takes place in the middle of chicane, Compton scattered electrons are detected in electron detector and non scattered electrons go to the right towards the experimental target.The energy-weighted counting asymmetry$\mathbb{A}$, of back scattered photons, between Compton scatterings of parallel and atniparallel polarizations of electrons and photons is given by:

$$\mathbb{A} = \frac{N^+ - N^-}{N^+ + N^-} = P_e P_\gamma A^{th}, \tag{2.9}$$

where P_e is the unknown electron beam polarization P_γ is laser polarization and A^{th} is analyzing power and it is given by [50]

$$A^{th} = \frac{2\pi r_0^2 a}{(\frac{d\sigma}{d\rho})} \ (1 - \rho(1+a))[1 - \frac{1}{1 - \rho(1-a)^2}], \tag{2.10}$$

where $a = \frac{1}{(1+4kE_e/m_e^2)}$, m_e is the electron mass, r_0 is the electron radius, k is energy of incident photon and E_e is energy of incident electron. The electron beam and laser collides with each other at a very small angle of 23mrad and in the calculation of response function it can be treated as linear collision. Polarization of the laser is flipped periodically between left and right to control the systematic errors. Background for Compton scattering is measured by turning off the cavity between the flipping of polarization. A GEANT4 simulation is used to extrapolate

the GSO response function. Figure2.16 on the next page is taken from [50] and it shows the Compton asymmetry for left and right circularly polarized laser states.
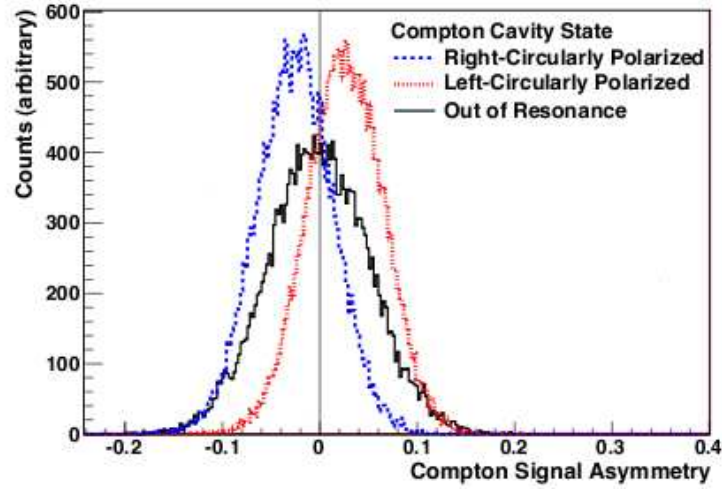
FIG. 2.16: Compton asymmetry for left(red) and right(blue) circularly polarized laser states.

2.5 Beam Monitering

In order to observe the parity violating asymmetry of the order of a few hundred part per billion and keep the systematics under desired level, a very precise measurement of beam position and intensity must be known for each helicity window. Then each detector signal is normalized with the beam intensity. Beam energy is also measured. Target density fluctuations are measured by luminosity monitors. The kind of monitors which are used in parity analysis are strip line monitors. Cavity monitors are also installed in Hall A. For each production run of PREx, beam parameters are recorded by EPICS and CODA.

2.5.1 Strip Line Position Monitor

Strip line monitors are located on many locations along the beam line. In PREx parity analysis two monitors are more important than others. One stripline beam monitor 4a(IPM1H04A) is located at 7.524m and the other monitor 4b(IPM1H04B) is located at 1.286m upstream from the target. Strip line monitors have four antennas fixed in a cylindrical cavity and tuned to the fundamental RF frequency of the beam. Beam travel along the axis of the cylinder. The position of these four antennas is rotated at $45\,^\circ$ counterclockwise to the EPICS hall A coordinate system and $135\,^\circ$ clockwise to the hall A transport system. The average position over 0.3 second is logged into the EPICS database. The RF signal from each antenna is proportional to the beam intensity times the distance of the beam from that antenna. Then RF signal is converted to DC signal via electronics shown in figure 2.17. In order to keep the pedestal and the gain same for each wire a gain switching technique is used which keeps the DC signal of the same size for different values of current. If X_s and Y_s are the X and Y position of the beam measured by stripline monitor then for parity analysis the X and Y position of the beam is given by a matrix of rotation.

$$\begin{pmatrix} X \\ Y \end{pmatrix} = \begin{pmatrix} \cos(45^\circ) & -\sin(45^\circ) \\ \sin(45^\circ) & \cos(45^\circ) \end{pmatrix} \begin{pmatrix} X_s \\ Y_s \end{pmatrix}. \tag{2.11}$$

Where X_s and Y_s are given by

$$X_s = \frac{37.52}{2} \left[\frac{X_p - X_m}{X_p + X_m} \right], \tag{2.12a}$$

$$Y_s = \frac{37.52}{2} \left[\frac{Y_p - Y_m}{Y_p + Y_m} \right], \tag{2.12b}$$

where 37.52mm is the distance between antennas (X_p, Y_p) and (X_m, Y_m). Further details of stripline position monitors can be found in [51].
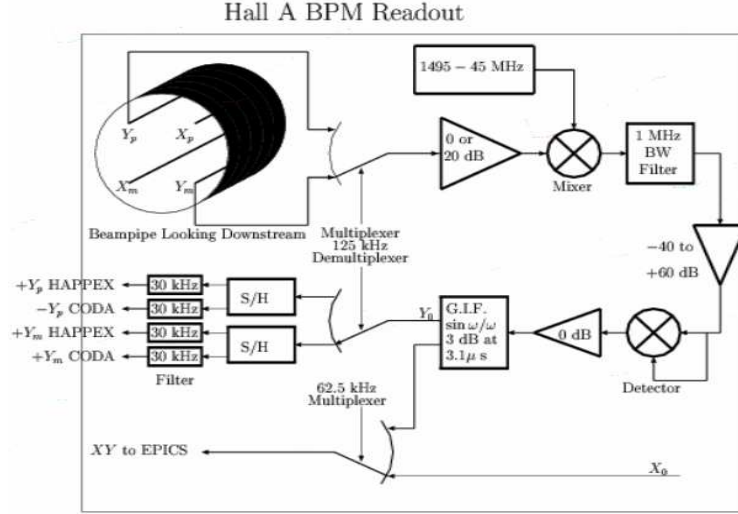
FIG. 2.17: Electronics of a strip line monitor.

2.5.2 Strip Line Current Monitor

The absolute beam current measurement is made by an unser[52] current monitor. The out put of unser monitor varies over a period of a few minutes. For continuous measurement of the beam current two stripline current monitors are used because current monitors are stable and linear over the range of beam current from 0.5uA to 70uA. Strip line current miniatures are located up and down stream of the unser monitor. Unser monitor is used to calibrate the stripline monitors. Unser and other monitors are very sensitive to temperature changes so all these devices are kept in a thermostablize box.

2.5.3 Cavity Monitors

Stripline monitors are used in parity analysis to normalize the detector signal. Along with strip line monitors (4A and 4B) there are two cavity monitors in the hall

A. Figure 2.18 shows the location of cavity monitors and stripline monitors. Cavity monitors were designed to measure the beam position at much low current regime like 50 to 25 nA. Stripline monitors cannot measure such a low current values. One of the reasons for such a low current is to measure the Q^2. Since the target is Lead very thick unlike to Hydrogen and Helium, the rates are very high and vertical drift chambers cannot perform at such a high rate. A nano ampere current range is required to measure the Q^2 with Lead target.
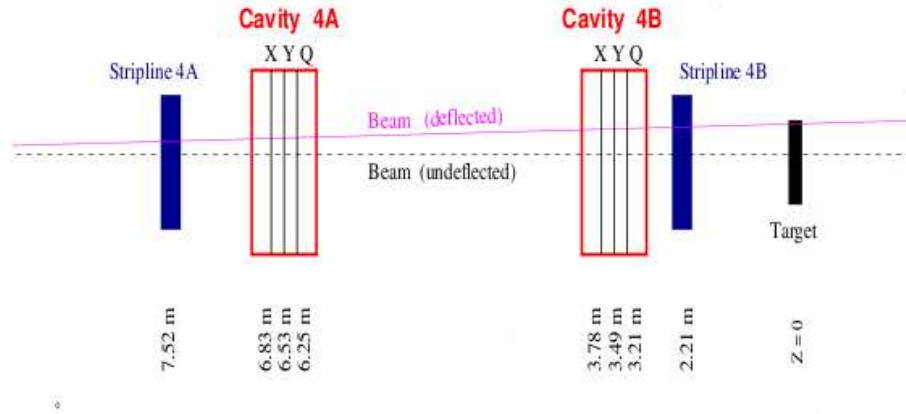
FIG. 2.18: Location of cavity monitors in hall A.

Cavity monitors are the cylindrical shape cavities made of stainless steal with low quality coefficient, $Q \approx 1500$. Cavity monitors or cylindrical cavities are tuned to 1497MHz frequency of the beam. Transverse electric modes are generated by the electron clouds passing through the cylindrical cavity. First monopole mode TM_{010} is coupled to the amount of charge in an electron cloud and the first dipole mode TM_{110} is coupled to the position of beam in the cavity. Each oscillating mode has an energy stored in it which is read out by electronics and gives accurate measurement of beam intensity and beam position. For example consider the TM_{110} mode. This mode is equivalent to a circuit of a capacitors and a inductor. Then resonance frequency is $\omega = (LC)^{-1/2}$ and R is the shunt impedance.

$$R = \frac{|\int^l 0 E(r)\exp^{j\omega t} dr|^2}{2P}, \tag{2.13}$$

where P is the power dissipated. The exchange of stored energy in TM_{110} mode and the cavity is given by

$$W = \frac{V^2}{2\omega}\frac{Q}{R}, \tag{2.14}$$

where V is the instantaneous voltage of mode TM_{110} and Q is the quality factor.
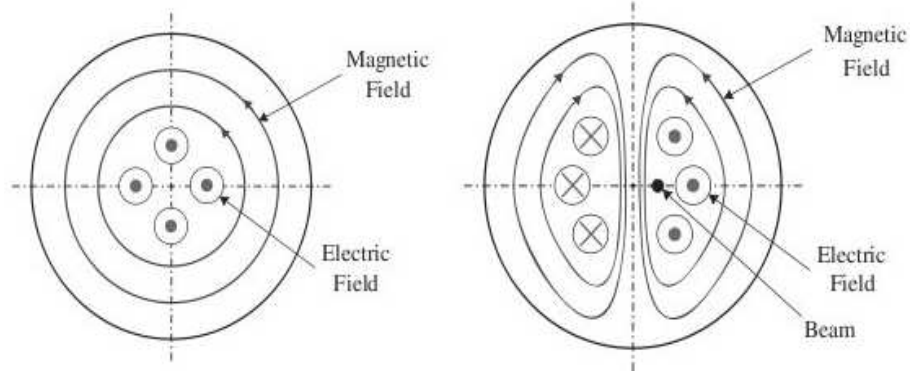
FIG. 2.19: Left diagram shows electric ang magnetic filed of resonance mode TM_{110}. Right Diagram shows electric and magnetic filed of resonance mode TM_{110}.

Details of cavity monitor are given in [53]. Cavity current monitor requires an amplifier if we go below 10 μA. Cavity monitors works well at nano Ampere current range. During the PREx we moved the beam at four corners of a $2 \times 2\ mm^2$ square at 25 nA beam current. This scan is shown below.

Scan size is $2 \times 2\ mm^2$ and the resolution is 1mm for cavity 2.

2.5.4 Target and Beam Raster

The cross section of electron cloud or the electron beam spot size is about $50\mu m$ and it can physically damage the target if it continually hit the target at same position. CW beam of this small size can also cause local density variations which can result in fluctuations of measured rates. In order to distribute the heat
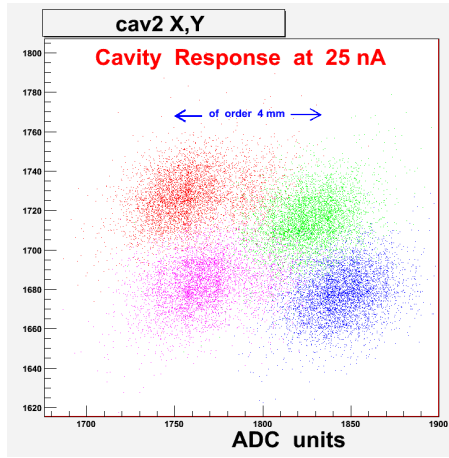
FIG. 2.20: Scan of 2 a × 2 mm^2 square at 25 nA.

deposit by the beam uniformly over the surface of the target, a beam raster system is used. The beam is rastered with two steering magnets upstream of the target at 25 kHz over and area of 4mm × 4mm.

Development of a Lead target that could operate at high current was a major concern. PREx target is made of 0.55mm thick Lead which is 99.1% isotopically pure Lead. This 0.55mm thick Lead foil is sandwiched between 0.15mm thick diamond foils. For good thermal conductivity a $25\mu m$ layer of Apiezon L vacuum grease is applied between Lead and Carbon surfaces. A pure hydrocarbon with high thermal conductivity, (Note: the background of this grease is negligible). The Lead-Carbon sandwich is squeezed by spring like washers which maintain a force to the sandwich. A silver-based paste is used between Carbon and Copper frame for heat sinking purpose. This paste in not applied to the central surface area of sandwich where beam hits the Lead target. The copper frame holding three PREx targets is cooled by cryogenic helium to 20K. Schismatic diagrams of target sandwich and cooling system is given below.

During the run we had two target related problems:

(1) after a week or so the target melted. The reason of melting was high radiation. Radiation slowly changed the crystal structure of diamond and as a result the ther-
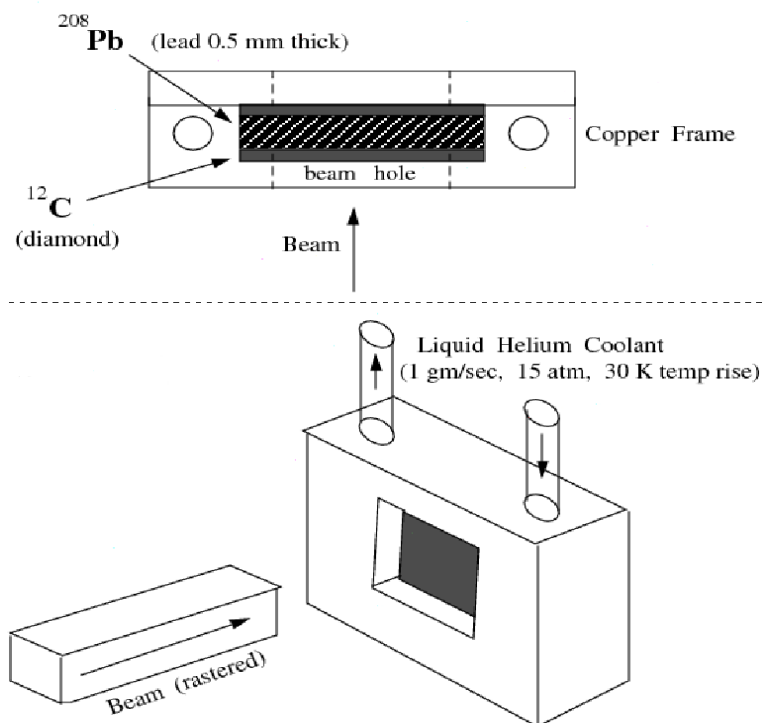
FIG. 2.21: Lead target is sandwich between two Carbon foils. Lead target is kept inside a Copper frame.
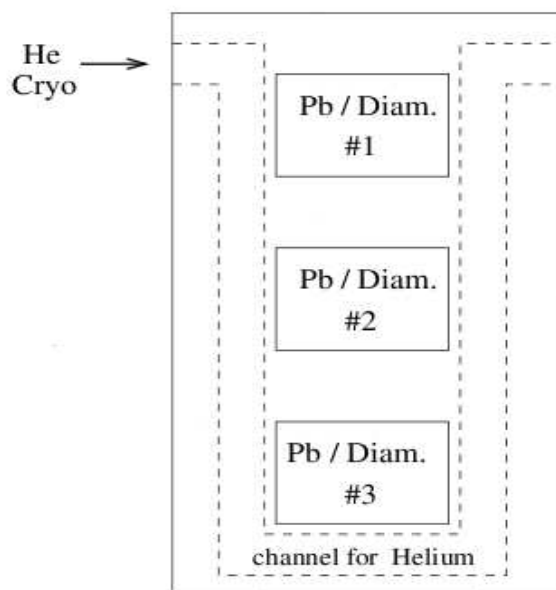
FIG. 2.22: Liquid He flows through the Copper frame around the three Lead targets.

mal conductivity decreased slowly. After some critical value there was not enough thermal conductive and the Lead foil melted. The life time of vacuum grease is 100MRad[54] and the life time of CVD diamond is given in[55]. The energy deposit in diamond by a $100\mu A$ electron beam is about $2\frac{MeV}{g/cm^3}$ and the radiation rate in diamond is $\approx 7 \times 10^4$ MRad/hr. This rate gave much higher dose of radiation to diamond in one week compared to its life time given by [55]

(2) The second target relating problem was fixed during the experiment. Before target melted its thickness became non uniform. The rasters' cycle was not synchronized with the helicity flip rate that resulted in acommone mode noise. As a result of this common mode nosies a left and right correlated asymmetry was observed. The raster was locked with helicity flip rate so that it could execute the same orbit between two helicity states and left and right asymmetry correlation was removed. the correlation. Figure2.23 shows the common mode noise correlation.
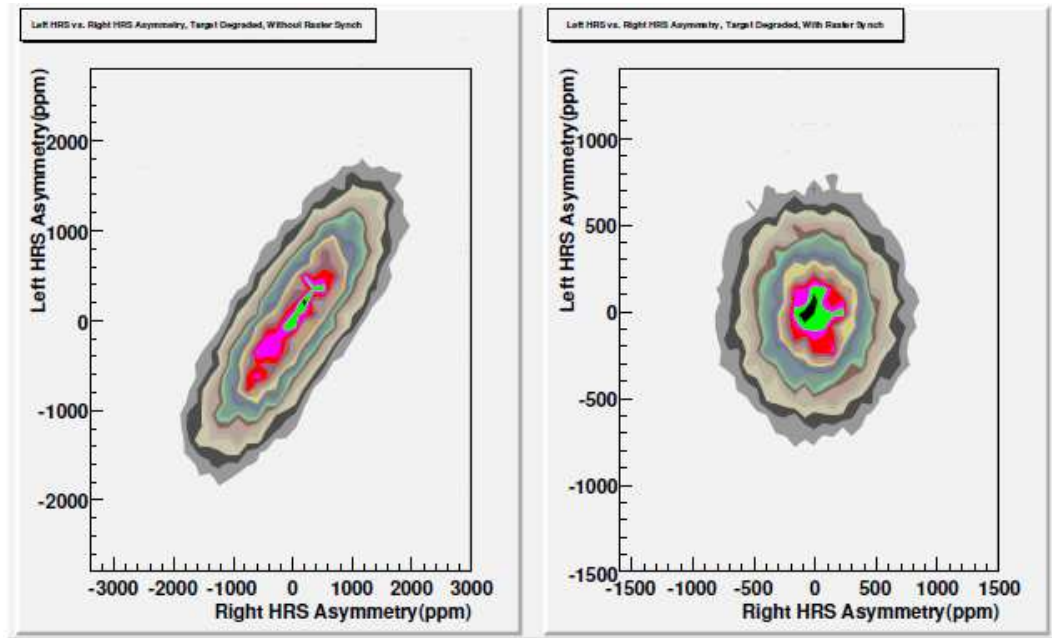
FIG. 2.23: Left graph shows correlation between left and right arm detectors when raster is not synced. Right graph shows correlation between left and right arm detectors when raster is synced. Both plots are with the degraded target.

There is another important issue related to the target, when target failed the

whole vacuum champer became contaminated with Lead i.e. a thin layer of Lead appeared on the scattering chambers' surfaces. In order to access the target chamber the target group had to wait for several days for radiation level go down.

2.5.5 Beam Modulating

Scattering cross section of electrons from ^{208}Pb atom depends upon energy and incident angle. If the electron beam is traveling along the z axis then the flux of the scattered electrons going into left and right detectors, for each helicity state, depends upon the position and angle of the beam hitting the target along x and y axis. Helicity correlated energy and position differences are small. But it is crucial to know the response of these parameters to the scattering cross section. For this we deliberately changed the position(x,y), angle(x,y) and energy of the beam for a short period of time. This procedure is known as beam modulation. Seven magnetic coils and an energy vernier are used in beam modulation. Magnetic coils are located upstream of the main bend arc of the hall A and energy vernier of cryo-module is in South Linac. During one run of data taking we have four modulation cycles. Response of position monitors and detectors is measured and then these responses are used in dithering analysis (chapter4). A typical response of monitors to a dithering cycle is shown in figure 2.27. Fast feed back(FFB) is turned off during beam modulation cycles for a production run.

2.5.6 Luminosity Monitor

Each luminosity or lumi monitor is a 12 inch long, 2 inch wide and 3/8 inch thick fused quartz connected to a PMT. In the quartz electrons emit Cerenkov radiation and this tradition is guided to PMT by a cylindrical aluminum walled light guide. Eight lumi monitors are located at 7m down stream from target symmetrically
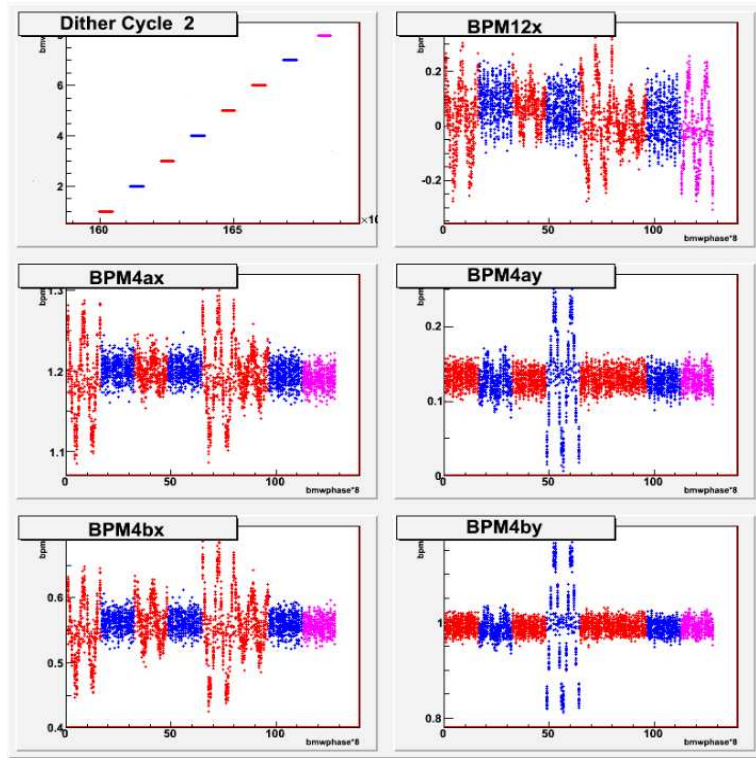
FIG. 2.24: Monitors response to dithering a cycle.

placed about the beam pipe line. Electrons scattered at and angle from 0.5° to 0.8°
are detected by lumi monitors. Lumi monitors are used to study the target density
fluctuations.

2.6 HRS and Septum Magnet

Two High Resolution Spectrometers(HRS) are the main experimental devices
of hall A. These spectrometers provide a momentum resolution better than 2×10^{-4}
and the horizontal angular resolution is better than 2 mrad at the design range of
central momentum from 0.8 to 4 GeV/c. High resolution of spectrometers makes
it possible to separate different reaction channels, for example to isolate elastic
scattered electrons from inelastic scattered electrons. The magnet configuration of
HRS is QQD_nQ. Scattered particles are focused vertically and horizontally by two

Parameter	Value
Configuration	QQD_nQ vertical bend
Bending angle	45°
Optical length	23.4 m
Momentum range	$0.3 - 0.4\ GeV/c$
Momentum acceptance	$-4.5\% < \delta p/p < +4.5\%$
Momentum resolution	1×10^{-4}
Dispersion at the focus(D)	12.4 m
Radial linear magnification(M)	-2.5
D/M	5.0
Angular range(LHRS)	$12.5° - 150°$
Angular range(RHRS)	$12.5° - 130°$
Angular Acceptance(Horizental)	± 30 mrad
Angular Acceptance(Vertical)	± 60 mrad
Angular resolution(Horizental)	0.5 mrad
Angular resolution(Vertical)	1.0 mrad
Solid angle at $\delta p/p = 0$, $y_0 = 0$	6 msr
Transverse length acceptance	± 5 cm
Transverse position resolution	1 mm

TABLE 2.1: Main design characteristics of hall A HRS

superconducting $\cos 2\theta$ quadrupole then they are bent at an angle 45° vertically up by a 6.6 m long dipole which also provide additional focusing from a field gradient(n) in the dipole. After the dipole there is another superconducting $\cos 2\theta$ quadrupole which provides better resolution of the horizontal and vertical coordinates of the target. HRS specifications are given in the table 2.1 which are taken from[56]. A schematic diagram of HRS is shown here inf figure2.25.

The largest part of uncertainties to parity violating asymmetry comes from Coulomb Distortions and Inelastic Scattering from excited states of Lead atom. The size of these uncertainties become as large as parity violating asymmetry and even larger beyond scattering angle of 6°. The minimum possible angle of measurement for the two HRS is 12°. A **Septum Magnet** was used for PREx. The particles which are initially scattered at 5.8° bent further by the septum magnet at an angle of 12° to enter the left and right HRS. 5.8° angle was selected because if we go below
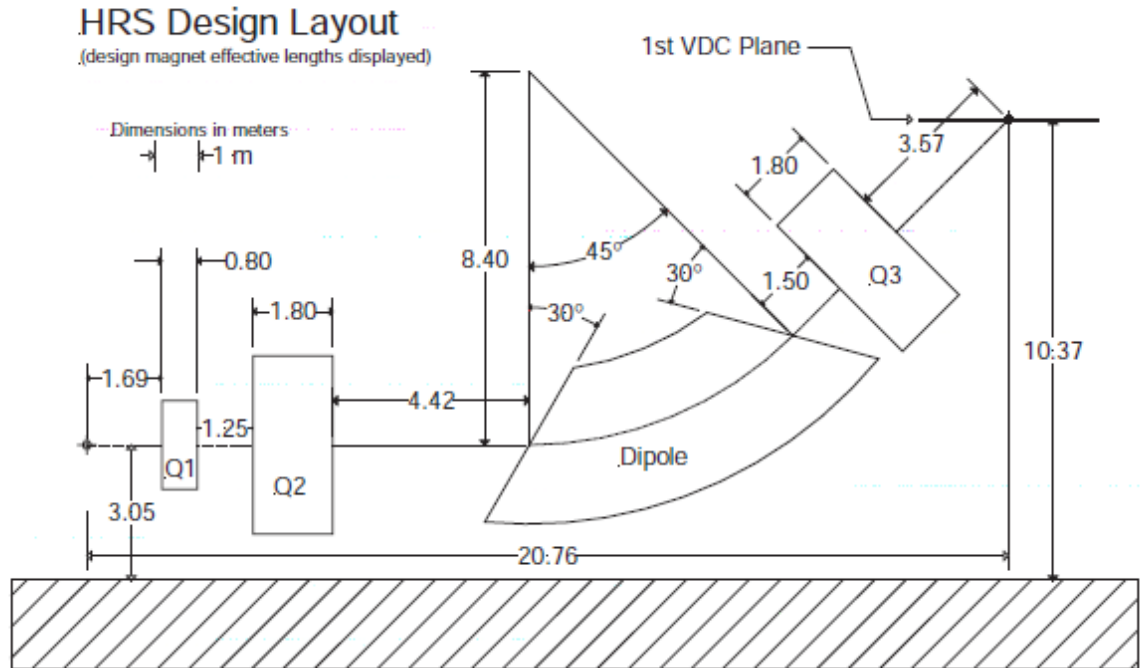
FIG. 2.25: A schematic diagram of HRS.

5.8° we were missing the solid angle. Diagram?? shows the location of septum magnet, target and two HRS.

We found that during the PREx we were running the septum magnet at low current and that reduced our acceptance. Following graph shows a comparison of PREx data and a Monte Carlo.

The dark line is real data and red is the Monte Carlo. In the left graph we have Monte Carlo with total PREx acceptance. In the right graph we run the Monte Carlo with cut on the scattering angle which reduces the accept acne and mimics the low current running of the septum magnet. Right graph shows a good agreement between PREx data and MC.
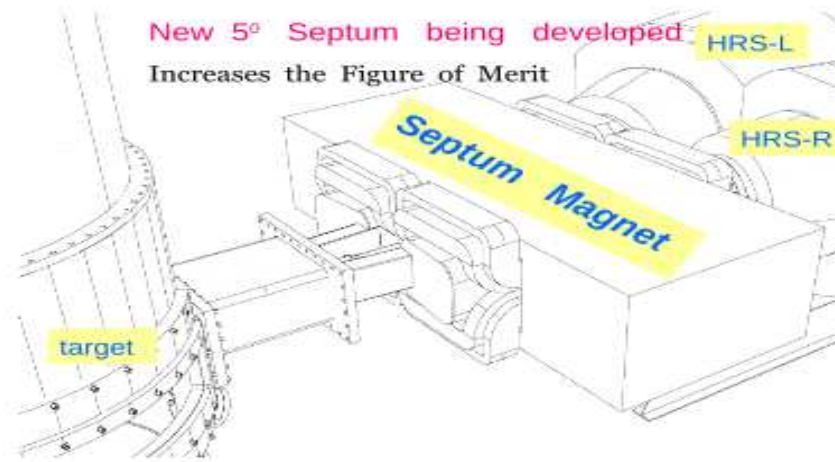
FIG. 2.26: Septum magnet is shown between scattering chamber and two HRS.
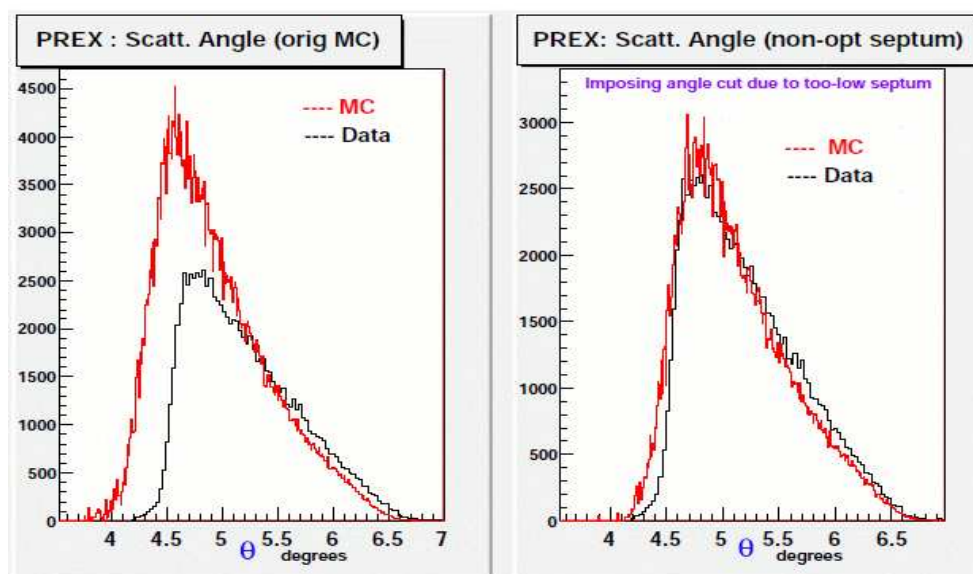
FIG. 2.27: Monte Carlo vs. real data for low current running of septum magnet

2.7   PREx Detectors

PREx detectors set consists of four detectors. Each detector has a quartz block facing a PMT. In each arm we have two detectors on the top of each other. The quartz are 14cm long and 3.5cm wide. Two lower quartz are 1cm thick and upper quartz are 0.6cm thick. All quartz are oriented so that the electrons pass through the larger surface at a 45 degree angle. There is a 45 degree level on the side of the quartz furthest from the PMT, in order to force electrons that travel away from the PMT to stay in the quartz via total internal reflection. Outside the quartz, there are mirrors forming a trapezoidal cone funneling towards the PMT. These detectors are made in University of Massachusetts.

CHAPTER 3

Flash ADC DAQ and Analysis

3.1   Introduction

PREx is designed to measure the neutron radius in ^{208}Pb with a precision of
1%. In order to keep the total error under 1% all possible sources of systematic
errors are studied and upgraded if necessary. One such possible source of systemics
is electron beam polarization which is used to normalize the measured parity violat-
ing asymmetry because the beam in not 100% polarized. If the systematic error of
beam polarization is more than the desired value then 1% error in ^{208}Pb radius mea-
surement is not possible to achieve. There are two independent polarimeters in hall
A to measure the beam polarization, Moller polarimeter and Compton polarimeter.
Moller polarimeter is upgraded for PREx, new superconducting Moller solenoid tar-
get and new scintillators were installed. In addition to upgrade the old Moller DAQ
a new data acquisition system was also installed. The new DAQ consist of Jefferson
lab custom built Flash ADC. The main purpose of FADC DAQ is to reduce the
dead time systematic error from 2% to 1%. The sample time of FADC is 4ns so we
can get all the information about detectors systematics from FADC data triggers. A

great success is also made by understanding the pile up effect on Moller asymmetry measurement. A good agreement between Moller asymmetry measurements of Old and FADC DAQs was the target for the FAC DAQ.

3.2 Moller Scattering

In 1932 C. Moller used the Dirac spinors and measured the scattering cross section of unpolarized electron electron scattering in quantum electrodynamics [57]. Since we cannot distinguish between scattered and recoil electron, there are two tree level diagrams that can contribute to the Moller cross section which are given below:
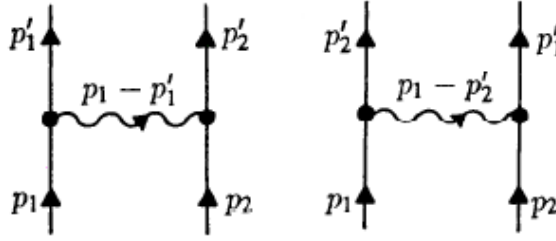
FIG. 3.1: Moller scattering. Left fig is the u channel and right fig is the t channel

In the center of mass frame four momenta of incoming and out going electrons are given by $p_1 = (E, \mathbf{p})$, $p_2 = (E, -\mathbf{p})$, $p_1' = (E, \mathbf{p}')$ and $p_2' = (E, -\mathbf{p}')$. Then the Moller cross section is given by [58]:

$$
\begin{aligned}
\left(\frac{d\sigma}{d\Omega}\right)_{cm} = {} & \frac{\alpha^2}{8E^2\mathbf{p}^4} \\
& \times \left\{ \frac{1}{(1-\cos\theta)^2} \left[(2E^2 - m_0^2)^2 + (\mathbf{p}^2(1+\cos\theta) + m_0^2)^2 - 2m_0^2\mathbf{p}^2(1-\cos\theta) \right] \right. \\
& + \frac{1}{(1-\cos\theta)^2} \left[(2E^2 - m_0^2)^2 + (\mathbf{p}^2(1-\cos\theta) + m_0^2)^2 - 2m_0^2\mathbf{p}^2(1+\cos\theta) \right] \\
& + \left. \frac{2}{(1-\cos\theta)(1+\cos\theta)} (2E^2 - m_0^2)(2E^2 - 3m_0^2) \right\}
\end{aligned}
$$

$$(3.1)$$

where θ is the scattering angle, E is energy of incoming electron and m_0 is the electron rest mass. At PREx energy we can use the ultra relativistic limit $E >> m_0$ of equation 3.3 which is

$$\left(\frac{d\sigma}{d\Omega}\right)_{ur} = \frac{\alpha^2}{8E^2}\left(\frac{1+\cos^4\frac{\theta}{2}}{\sin^4\frac{\theta}{2}} + \frac{1+\sin^4\frac{\theta}{2}}{\cos^4\frac{\theta}{2}} + \frac{2}{\sin^2\frac{\theta}{2}\cos^2\frac{\theta}{2}}\right) \tag{3.2}$$

Beam polarization measurements in hall A polarimeter involve the scattering of polarized electrons. Cross section for polarized electron electron scattering was given by [59]:

$$
\begin{aligned}
\left(\frac{d\sigma}{d\Omega}\right)_{pol} = {} & \frac{r_0^2}{4}\frac{1}{\gamma^2(\gamma^2-1)^2\sin^4\theta} \\
& \Big\{ [(\gamma^2-1)^2(4-3\sin^2\theta) + (\gamma^2-1)^2(\sin^4\theta + 4\sin^2\theta)] \\
& + 2(1-\gamma^2\sin^2\theta) \times (\mathbf{s}_1\cdot\mathbf{p}')(\mathbf{s}_2\cdot\mathbf{p}') \\
& - [(4\gamma^2-3)\sin^2\theta - (\gamma^2-1)^2\sin^4\theta] \times (\mathbf{s}_1\cdot\mathbf{s}_2) \\
& + 2[1-(4\gamma^2-3)\sin^2\theta + (\gamma-1)^2(\sin^4\theta-\sin^2\theta)] \times (\mathbf{s}_1\cdot\mathbf{p})(\mathbf{s}_2\cdot\mathbf{p}) \\
& - 2\cos\theta[1-\gamma(\gamma-1)\sin^2\theta][(\mathbf{s}_1\cdot\mathbf{p}')(\mathbf{s}_2\cdot\mathbf{p}) + (\mathbf{s}_1\cdot\mathbf{p})(\mathbf{s}_2\cdot\mathbf{p}')] \Big\}
\end{aligned}
\tag{3.3}
$$

where $r_0 = e^2/mc^2$ and $\mathbf{s}_1$ and $\mathbf{s}_2$ are spin vectors of incident and target electron respectively and similarly $\mathbf{p}$ and $\mathbf{p}'$ are the momenta of incident and target electron respectively. For Moller polarimeter it is convenient to use the notation given by [60]. So we can write the above mentioned cross section of polarized Moller scattering in center of mass frame as:

$$\left(\frac{d\sigma}{d\Omega}\right)_{cm} = \left(\frac{d\sigma}{d\Omega}\right)_0\left[1 + \sum_{j,k=z,y,z} a_{jk}P_j^B P_k^T\right] \tag{3.4}$$

where $\frac{d\sigma}{d\Omega_0}$ is the unpolarized Moller cross section, P_j^B, P_k^T are the beam and target polarizations respectively and $a_{j,k}$ are the asymmetry coefficients a.k.a. analyzing power. Since parity is conserved in QED so we have $a_{yz} = a_{zy} = a_{xy} = a_{yx} = 0$.

Other five asymmetry coefficients are given below. Equation 6.43 of on page 145 of [61] provides great help to understand and extract asymmetry coefficients.

$$a_0 = (2\gamma^2 - 1)^2(4 - 3\sin^2\theta + (\gamma^2 - 1)^2)(4 + \sin^2\theta)\sin^2\theta, \tag{3.5a}$$

$$a_{zz} = \sin^2\theta[(\gamma^4 - 1)\sin^2\theta - (2\gamma^2 - 1)(4\gamma^2 - 3)]/a_0, \tag{3.5b}$$

$$a_{yy} = \sin^2\theta[(\gamma^2 - 1)^2\sin^2\theta - (4\gamma^2 - 3)]/a_0, \tag{3.5c}$$

$$a_{xx} = -\sin^2\theta[(\gamma^4 - 1)^2\sin^2\theta + (2\gamma^2 - 1)]/a_0, \tag{3.5d}$$

$$a_{xz} = a_{zx} = -[(\sin^2\theta)\gamma(\gamma^2 - 1)^2\sin 2\theta]/a_0, \tag{3.5e}$$

The necessary relationships between center of mass frame and lab frame are given below:

$$E = \sqrt{m(E_l + m)/2}, \tag{3.6a}$$

$$\gamma = \sqrt{(\gamma_l + 1)/2}, \tag{3.6b}$$

$$\tan(\theta/2) = \tan\theta_l\sqrt{(E_0 + m)/2m}, \tag{3.6c}$$

$$d\Omega = \frac{8(E_0 + m)\cos\theta}{[2m + (E_0 - m)\sin^2\theta]^2}d\Omega_l, \tag{3.6d}$$

Where E_0 is primary energy and subscript l is for lab frame, quantities without subscript are in the center of mass frame. In paper [62] it is shown that when the

spins of target and incoming electrons are anti parallel then scattering cross section is grater than the situation when these two spins are parallel. At high energies $\gamma \gg 1$ the asymmetry coefficients are given by:

$$a_{zz} \rightarrow \frac{\sin^2 \theta (8 - \sin^2 \theta)}{(4 - \sin^2 \theta)^2}, \tag{3.7a}$$

$$a_{yy} = -a_{xx} \rightarrow \frac{\sin^4 \theta}{(4 - \sin^2 \theta)^2}, \tag{3.7b}$$

$$a_{xz} = a_{zx} \rightarrow 0, \tag{3.7c}$$

These functions are drawn in following diagram:
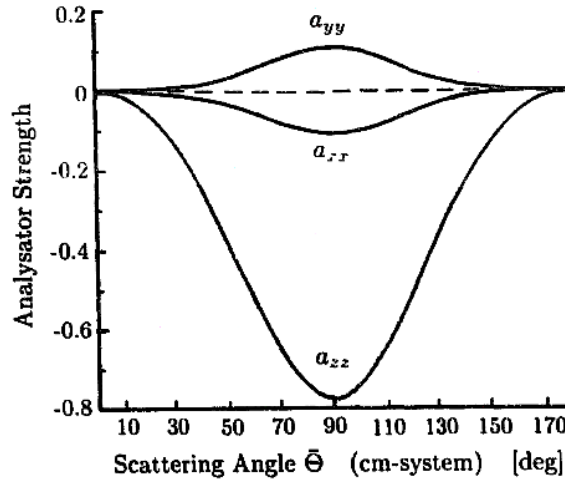
FIG. 3.2: Moller longitudinal a_{zz} and transverse(a_{xx}, a_{yy}) asymmetries v/s scattering angle in the center of mass frame at high energies.

At $\theta_{cm} = 90°$ the longitudinal analyzing power a_{zz} is maximum, $-\frac{7}{9}$.

3.3 Moller Polarimeter

Moller polarimeter is located at downstream to Compton chican. Due to higher rate Moller polarimeter is preferred for low current parity experiments, it is equally

useful for higher current experiments. Moller polarization measurement is an invasive measurement because we need Moller target for beam polarization measurements. Moller polarimeter is 7 meter long and consists of Moller target, three quadruples, a dipole and a target. It is a coincidence mode Moller spectrometer which is designed to detect the Moller electrons scattered at $\theta_{cm} = 90°$. It can measure the beam polarization for beam energies 0.8 GeV to 6 GeV. A schematic diagram of top and side view of Moller polarimeter is given below.
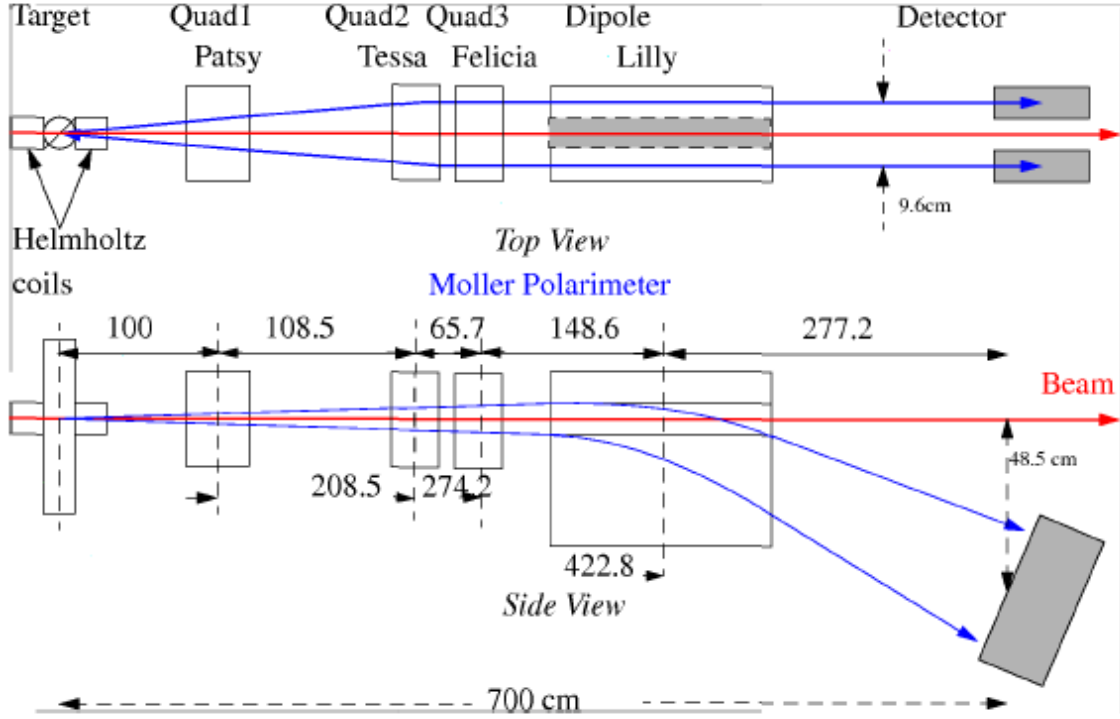
FIG. 3.3: Hall A Moller polarimeter top and side views. Beam hits the Moller target on left, Moller scattered electrons passes through quads Q1, Q2 and Q3 and then bend down by dipole and hits the target. Beam goes to the right to the beam dump.

Different parts of Polarimeter are explain in detail below.

3.3.1 Moller Target(Old)

Moller target for PREx was upgraded to a 4 Tesla superconducting solenoid target . Target upgrade and new Moller target is discussed in next section. Five

Moller targets(given in table below) are placed on sliding rail which can move the targets across the beam.

Target	6	5	4	3	2	1	0
Material	Beam hole	SM	Fe	Fe	SM	SM	Al
Thickness(μm)		6.8	9.3	14.3	29.4	13.0	16.5
Polarization(%)		7.97	7.44	7.62	8.21	7.80	

In this table SM stands for supermendur alloy. Before Nov 2004 beam polarization was measured at angle 20° and 105° and then average was calculated to cancel the effect of small transverse polarization in beam and in the target. After Nov 2004 target fails are kept at angle 20° to the beam in the vertical plane because vertical beam polarization is very small so we get Moller asymmetry only from longitudinal polarization.[63]. Target foils are magnetized by two Helmholtz coils in longitudinal direction to the beam with an applied field of 350 Gs. Target motion is watched by two TV cameras and temperature is controlled by water cooling. A few μA current can increase the target temperate to 20-40 K locally. The target settings were changed for PREx.

3.3.2   Moller Spectrometer

Hall A Moller polarimeter has a magnetic spectrometer consist of three qudrapoles and a dipole. The QQQD design of Moller spectrometer selects the Moller scattered in horizontal plane in a kinematics range of 70° < θ_{cm} < 105°. At the end of third quad the Moller particles are aligned along the beam axis. Next is the dipole which works as momentum analyzer as it separates the Moller electrons from Mott electrons. There is a collimator in front of the dipole which limits the azimuthal acceptance. In the median of dipole a piece of iron with a hole in it is placed. Electron beam passes through this hole to the beam dump and Moller electrons are

bent down by dipole. Effect of dipole on beam is negligible.[64]. For a given beam energy e.g. 1 GeV for PREx, the quad settings can be obtained by the PAW like this ($PAW > exec\ sett_magp\ e0 = 1\ nq = 3$), where 3 is for quad 3. The location of quads and dipole is shown in fig 3.3.

3.3.3   Moller Detector

Moller polarimeter detector is a spaghetti type coincidence mode calorimeter detector. Formulas published in [65] and [66] are used for hall A Moller polarimeter's target design. We have two columns of detectors, left and right, located in the shielding box downstream of the dipole to detect the Moller electrons in coincidence. Whole detectors package in each column consists of four scintillators and four calorimeters. Each calorimeter is assembled with $9cm \times 15.1cm \times 30cm\times$ blocks of Scintiplex III acrilic scintillator fiber using rolled Lead plates with semicircle channels. The scintillator fibers are separated by Lead plates. These fibers are along the direction of incident Moller electron. Photo-electron yield is 383p.e./GeV and the non linearity of detector is not more than a few percent for energy 1 to 3 GeV. Each calorimeter block is connected to Photonics XP2282B(2 inch) photomultiplier tube. Incoming Moller electrons passes trough the scintillator. Scintillator is connected to Hamamatsu R4124 photomultiplier tube of 13 mm diameter. Size of all four scintilla rots in one column is $31cm \times 4cm \times 3.6cm$. High voltages on all the calorimeter blocks are so adjusted that all the modules show Moller signal at ADC channel 300(old DAQ). So the bottom four modules have 50% higher gain than the top four modules. Details about Moller polarimeter detector can be found in[67].

3.4 Moller Polarimeter Upgrade

PREx is designed to measure the parity violating asymmetry of polarized electrons scattered off the Lead target with 1%. Since electron beam at TJNAF is not 100% polarized so we need to normalize the mesured asymmetry with beam polarization to get the physics asymmetry. In order to keep the error to 1% the beam polarization must be measured within one percent of error. Moller polarimeter is upgraded for PREx. Old configuration measured the polarization with total 2% error. Moler polarimeter upgrade has these three installations. The installation of new scintillators. The installation of new superconducting high magnetic field solenoid Moller target. The last step is the installation data acquisition system based upon flash ADC was also installed.[68]. Upgrade of Moller polarimeter is discussed below.

3.4.1 New Moller Target

Before PREx upgrade of the Moller polarimeter the Moller target is kept in a magnetic field of 350 Gauss applied by two Helmholtz's coils. This is a weak magnetic field. The systematic error of the target polarization is almost 2%. In order to reduce the systematic error due to target magnetization a brute force approach of magnetization is used for pure iron target foils. Pure iron target foils are saturated by keeping them in high magnetic filed of 4 Tesla with help of a super conduction split-coil solenoid. This approach is first proposed by [69]. For pure iron the electron polarization at saturation is known with very high precision[70]. The effect of magnetic filed on the electron beam is small, the fringe field has small focusing effect.

3.4.2   New Scintillators

There were two old aperture counters, one segment in each arm and they were overloaded for currents $> 1\mu A$. New scintillators consist of four segments in each arm. Three segments are equal in lenght and the fourth segment is longer than other three. Size of three small segments is $10cm \times 2cm \times 2cm$ and the size of long segment is $31 \times 2 \times 2cm$. The long scintillator segment is located inside the detector, close to the acceptance, other three are out side of the detector on the top of each other. The schematic diagram of new scintillators is shown in figure 3.4 . Black rectangle blocks represent the scintillators and the blue circles show the calorimeter blocks. Moller electrons first pass through the scintillators and then hit the calorimeter. A Hamamatsu R1424 PMT is connected to each scintillator.
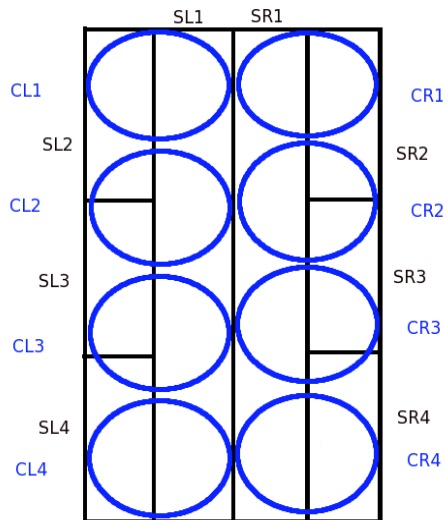
FIG. 3.4: A schematic diagram of Moller target scintillators and calorimeters. Black rectangle are the scintillators and the blue circles are the calorimeter.

New scintillators work at 5μA and also reduce the background. Scintillator signals arrive 12 nsec earlier than calorimeter signals at FADC. Third step of Moller polarimeter upgrade is the installation of new FADC DAQ and it is described in detail in next section.

3.5   Flash ADC DAQ

Flash ADC data acquisition system consist of a single VME crate which includes a Jefferson lab custom built Flash F250 ADC, a VME ROC, a Flex IO, a Level Converter and two other auxiliary support modules. One auxiliary module is CAN v560 scaler and the auxiliary module is CEAN v792 QDC. Flash ADC is the cutting edge device built at Jefferson lab for data acquisition and first time installed right before HAPPEX III for Moller polarimter in parallel to the old DAQ. FADC DAQ had become fully operational by the end of PREx. A NIM crate on the top of FADC VME crate is also used to split the signals like MPS, QRT and BCM etc. for old DAQ and FADC DAQ. NIM crate is also used to convert the signals from LEMO to ECL.

We needed to upgrade the Moller polarimeter not only for the PREx but also we wanted to install a new DAQ as the old DAQ is 12 years old and has no spares. Old DAQ is also not fast enough for high current measurements. The main purpose of FAD DAQ is to reduce the dead time systematic error to zero so that the total systematic error of Moller polarimeter reduces from 2% to 1%. The 4 nsec sample time of FADC enables us to get complete information about detector systematics and performance with the help of FADC data triggers.A schematic diagram figure 3.5 and a real diagram figure 3.6 of FADC DAQ are shown below.

The hardware details of FADC DAQ are given below. The details of FADC DAQ can be found here[71]. A brief introduction of important parts of FADC DAQ is given below.

3.5.1   F-250 Flash ADC

Jefferson lab custom built F250 Flash ADC is the heart of FADC DAQ. In this section the characteristics of FADC and how it is programmed to generate trig-
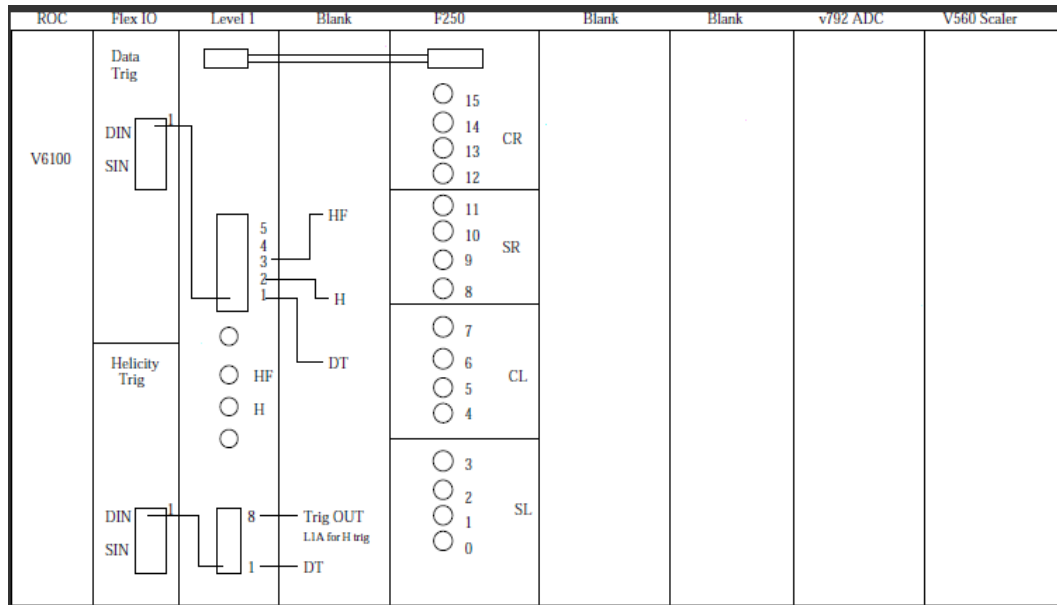
FIG. 3.5: FADC DAQ. A schematic diagram of VME crate.
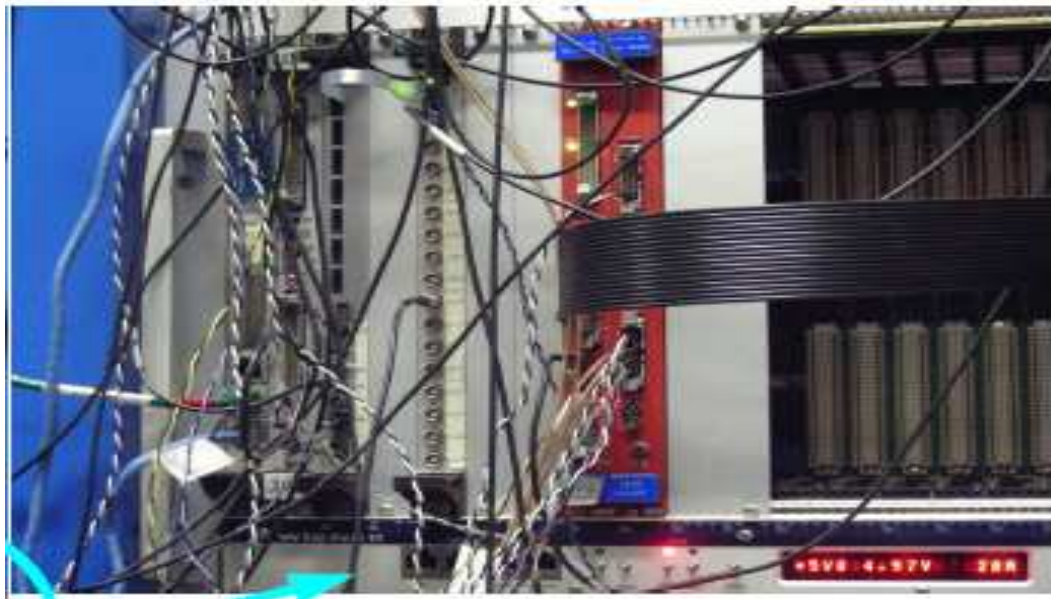
FIG. 3.6: FADC DAQ. A real diagram of VME crate.

gers for Moller measurements are discussed. FADC has 16 analog LEMO inputs(8 calorimeter blocks and 8 scintillators paddles). The helicity signal has an ECL input at the top of FADC. Its sample time is 4 ns and it has 12bits/sample resolution. Its a FPGA device so it has the flexibility of software to the hardware speed. Data triggers are generated by FADC so we do not need signal splitters, discriminators or summing modules. All the necessary characteristics of the signals from PMTs like threshold, sample window, coincidence window, pulse width and prescales are controlled by software.

3.5.2   FADC Logical Signals for Moller

Analog signals from calorimeter and scintillators which are digitized and recorded as data trigger by FADC pass through the logic in FPGA specially designed for Moller DAQ. The Moller signals are typically > -1 Volts so the first step is to digitized only those signals which are large enough. i.e. pass the threshold. If P_i^j and S_i^j are analog signals where i is number of channels and j is number of samples then the signal logic is given by

- **CL** $= \sum_{i=1,4} \sum_{j=1,2} P_i^j \geq Thresh_1$

- **CR** $= \sum_{i=1,4} \sum_{j=1,2} P_i^j \geq Thresh_1$

- **SL** $= \left(\sum_{j=1,} S1^j \geq Thresh_2\right)$ **.OR.** $\left(\sum_{j=1,} S2^j \geq Thresh_2\right)$ **.OR.** $\left(\sum_{j=1,} S3^j \geq Thresh_2\right)$ **.OR.** $\left(\sum_{j=1,} S4^j \geq Thresh_2\right)$

- **SR** $= \left(\sum_{j=1,} S5^j \geq Thresh_2\right)$ **.OR.** $\left(\sum_{j=1,} S6^j \geq Thresh_2\right)$ **.OR.**

$$\left(\sum\nolimits_{j=1,} \text{S7}^j \geq \text{Thresh}_2\right) \text{ .OR. } \left(\sum\nolimits_{j=1,} \text{S8}^j \geq \text{Thresh}_2\right)$$

The data from any channel of FADC is summed over two sample windows. The coincidence Moller events in left and right arms are within a time window of 8 nsec. Next step is to record the data trigger. All those signals which pass the threshold are mixture of single and coincidence Moller events. Single events **CL**, **CR** and coincidence events **CL.AND.CR** can be prescaled from 1 to 2000. Sample sum size and thresholds can be programmed in FADC. Data from each channel of FADC is stored on a circular buffer. When trigger input is active FADC looks 100 nsec back. This 100 nsec time is called "Programmable Latency". Please see the figure 3.7. Starting from the point where the time "Programmable Latency" starts, the data is processed which is inside the time window "Program able Trigger Window". "Program able Trigger Window" is 8 nsec long. There are two data events in figure 3.7 at time T1 and T2 respectively. These two events are within "Program able Trigger Window" and they have crossed the "Trigger Energy Threshold"(TET). A pulse height sum of these two events is performed over "Programmable Number of Sample". "Programmable Number of Sample" are 2 sample windows of FADC. NSB stand for "Number of Samples Before" and NSA stands for "Number of Samples After". The pulse height sum is performed from NSB of T1 to NSA of T2. The SUM1 and SUM2 are passed to VME FPGA. The data trigger of FADC is determined by the area under the digitized pulse. In Old DAQ data trigger is generate if the pulse from PMT tube crosses a potential threshold. This is the fundamental difference between data triggers of FADC DAQ and old DAQ. FADC keep storing the data on circular buffer so no data is lost. FADC works in counting mode.

Scintillator data is averaged over two sample windows and then checked against the TET. When the average of a scintillator channel is less than TET, Hit Bit for that channel is turned on and remains on as long the two window sample average
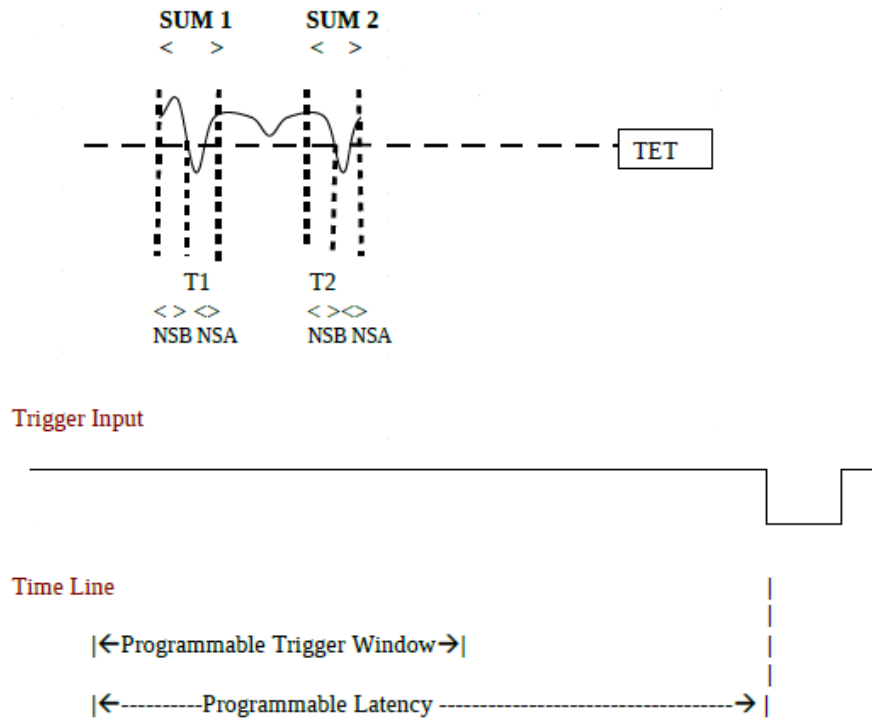
FIG. 3.7: FADC dta trigger.

is less than TET. Hit Bits are then converted to Hit Sum. Besides data triggers there are inboard program able scalers in FADC. Helicity signal going into FADC via a ribbon cable at the top of LEMO inputs act as a trigger for scalers. Scalers essentially work as a dead time-free integration of data by counting the number of single and coincidence data within a given helicity state. There are total seven onboard scalers

1) **CL**

2) **CR**

3) **CL** and **SL**

4) **CR** and **SR**

5) **CL** and **CR**

6) **CL** and **CR** and **SL** and **SR**

7) **CL** and **CR** and (**SL** and **SR** delayed by 100 nsec)

Moller asymmetry is measured by the logic of scaler no. 6 and for background subtraction we used the scaler no. 7.

3.5.3 FADC Data Acquiring Overview

When we start taking data and the "Go" is turned on FADC wait for the next trailing edge of the "HELICITY_FLIP" signal. After trailing edge of the HELICITY_FLIP signal ENABLE_MOLLER period starts, data is digitized and scalers are counting.
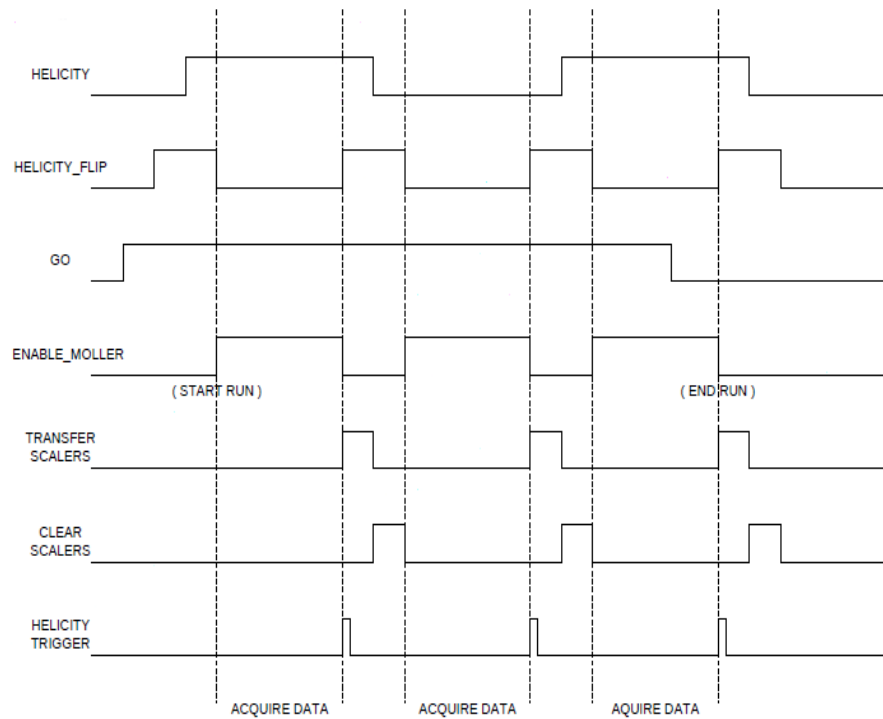
FIG. 3.8: FADC data taking.

When FADC sees the HELICITY_TRIGGER pulse it stops, leading edge of HELICITY_FLIP arrives at same time and ENABLE_MOLLER period ends. FADC FPGA passes on the digitized data and the scaler values. Scalers are cleared and CLEAR_SCALERS pulse is issued. The next trailing edge of HELICITY_FLIP

signal arrives and same procedure starts again. When "GO" is turned off FADC wait for the next leading edge of HELICITY FLIP to make sure that the data is acquired for an integral number of definite helicity states. This process is described in figure 3.8.

3.5.4 ROC, Flex IO and SD-FG Modules

In figure 3.5 the first module from left is a MVME v6100 single board Read Out Computer(**ROC**). ROC takes the digitized data and the values of onboard scalers from FADC and sends them to CODA. Next to ROC is **FLEX − IO** which has two parts. Top half handles the data trigger generated by FADC and the associated trigger is labeled as "DT". Bottom half handles the helicity triggers and the associated triggers are labeled as "HT". Third module is FPGA based **SD − FP** which works as a level 1 converter. It has ECL and LEMO inputs, we used ECL inputs. The MPS pulse goes into input "HF" of SD-FG. MPS pulse starts a blank out interval during which scalers values are read and ROC transfers the data. Input "H" is for the helicity state signal and input "DT" for the data triggers. One auxiliary modules is conventional **v650** scaler and other auxiliary module is **v792** QDC. Extra copies of MPS, HELICITY and QRT goes into v792 QDC for double check purpose. Other important signals like beam current, a 100 kHz clock and Moller target position are plugged into v560 scaler.

3.5.5 NIM Crate

On the top of FADC VME crate, there is a NIM crate, used to split some signals for FADC and old DAQ. We also used the signal converters in NIM crate to convert BCM, 100 kHz clock, MPS, QRT and Helicity signals from LEMO to ECL. One ECL output goes to v792 scaler and the other ECL output goes to FlEX-IO. Shpe

of MPS pulse is adjusted by using a discriminator in NIM crate and then adjusted MPS signal is sent to old DAQ and FADC DAQ.

3.5.6 FADC Data Events

Flash ADC helps a lot to understand the pile up effect and separates the Moller events from non Moller events. Since the sample time of FADC is 4 nsec so we can essentially get a pulse profile for each data event. The coincidence window for Moller event is 8 nsec or two FADC sample windows. Following diagram 3.9 shows the pulse profile of a super coincidence Moller data event. The time delayed on calorimeter and scintillator channels is set such that the scintillator signal is shown 20 nsec earlier than calorimeter channels. We can see that all the calorimeter blocks show a pulse at sample no 9(36 nsec) and all the scintillators show the pulse at sample no 4(16 nsec). Red line is the pulse height histogram of current data event.
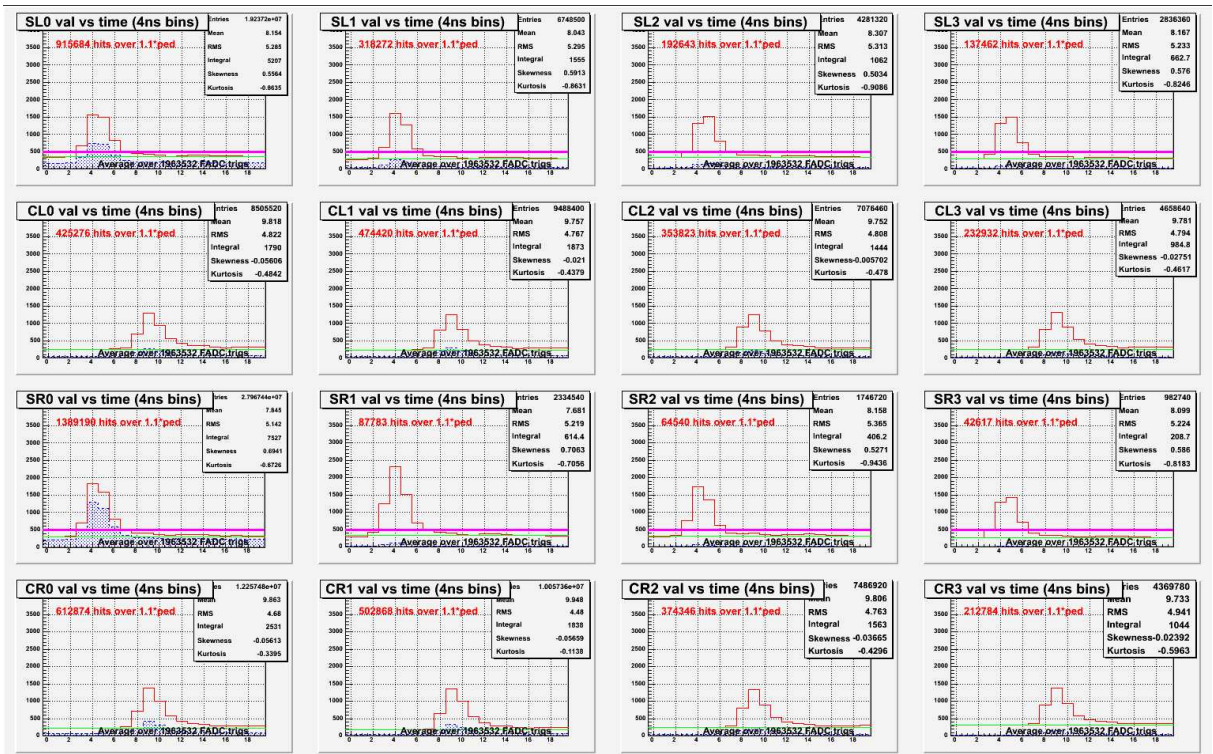
FIG. 3.9: One Moller FADC data event.

Moller polarimeter measures the rate asymmetry of coincidence Moller events to get the beam polarization. With the help of FADC we can separate the coincidence Moller events from other **non coincidence Moller** signals generated at the detector. Figure 3.10 shows a non coincidence Moller event occurred after 16 nsec of coincidence Moller event. For simplicity scintillator pulse is not turned off.
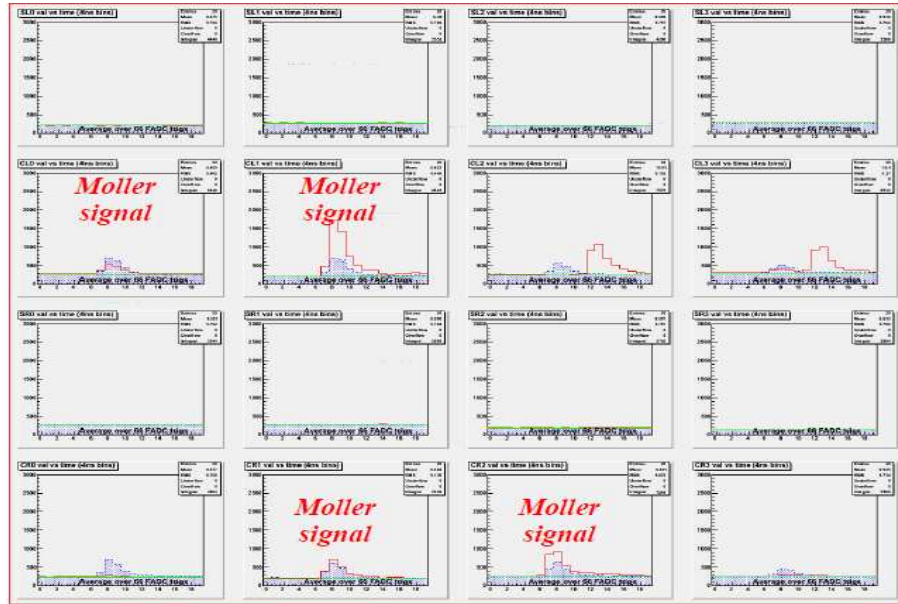
FIG. 3.10: Coincidence and non coincidence Moller FADC data event.

We must take account of **pile up** effect while extracting the beam polarization from measured asymmetry. Old DAQ uses a scaler which has a time delay between scintillator and calorimeter signals to get an estimate of pile up effect. FADC actually gives us the snapshot of each event taking place in detectors and it extracts the pile up events very cleanly from the Moller events, see fig 3.11. In first and second blocks of calorimeter right arm shows two signals which are not Moller coincidence events, pointed by a green question mark. It will make the rate of right arm larger than left and induces a false asymmetry.

An electron entering the detector can produce the signal in more than on calorimeter block. The Moller signal in detector can be distributed over all of four
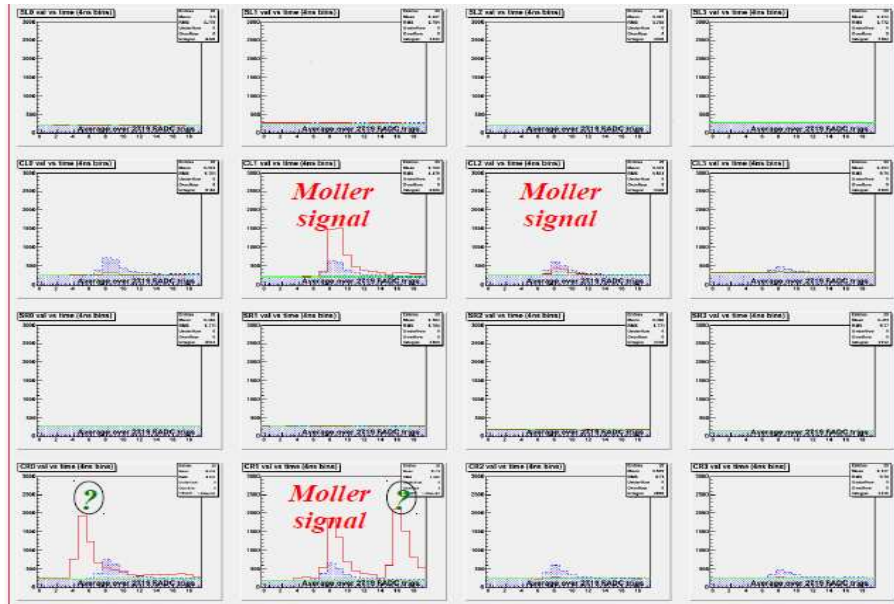
FIG. 3.11: Pile up and a coincidence Moller FADC data event.

calorimeter blocks. Following two figures 3.12 and 3.13 show the energy shared by top left calorimeter block and second right calorimeter block with all other calorimeter blocks.

Top left calorimeter block shares the energy of the signal with a calorimeter block right beneath it so we can see the energy correlation as a dark line. This dark line tells that if more energy is shared by CL-1 block then less energy is shared by CL-2 block and vice versa. Left and right arms are physically separated so we do not see the same distribution of energy between CL-1 and CR-2. CL-1 block has its coincidence Moller electron in CR-3 block and CR-4 block, while CL-3 block in figure 3.13 has its coincidence Moller electron in CR-1 block and CR-2block . This is a manifestation of conservation of momentum. Second calorimeter right block CR-2 has same energy sharing and its coincidence electron is in CL-2 block.

Histogram of total energy deposit in one arm of calorimeters is very helpful to understand the Moller signal and pile up effect. If we histogram the sum of area under the pulse in all the four blocks of right arm calorimeters then the horizontal
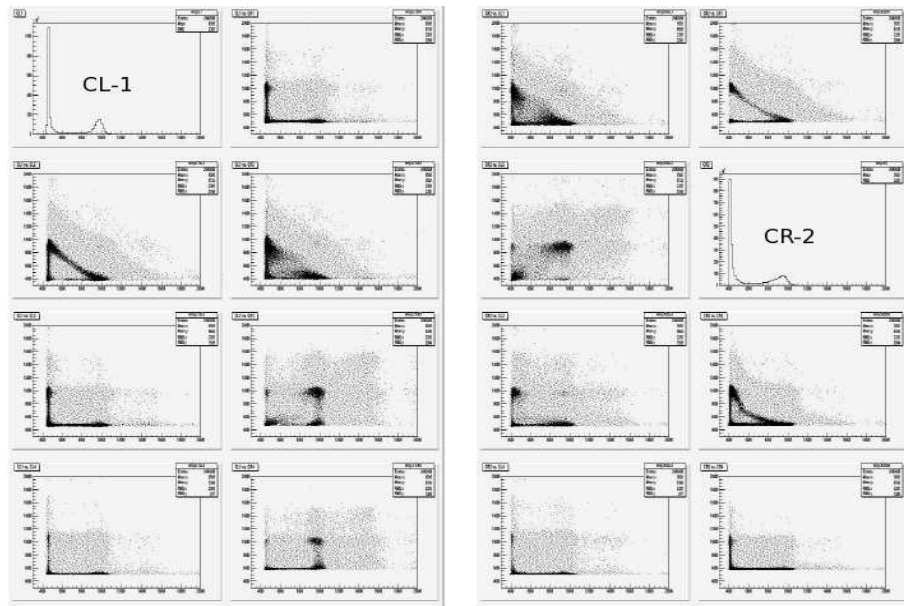
FIG. 3.12: Energy sharing of CL-1(left) and CR-r(right) calorimeter block with all other calorimeter blocks.
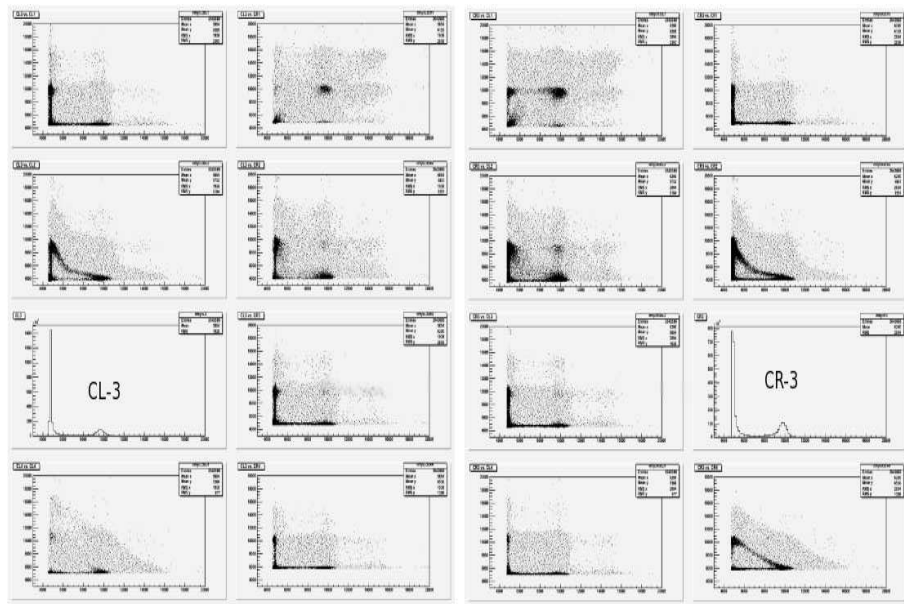
FIG. 3.13: Energy sharing of CL-3(left) and CR-3(right) calorimeter block with all other calorimeter blocks.

axis of figure 3.14 is proportional to the energy deposit in right arm of calorimeters. We can clearly see the FADC pedestal, FADC FPGA threshold, Moller signal and the pileup in figure 3.14.
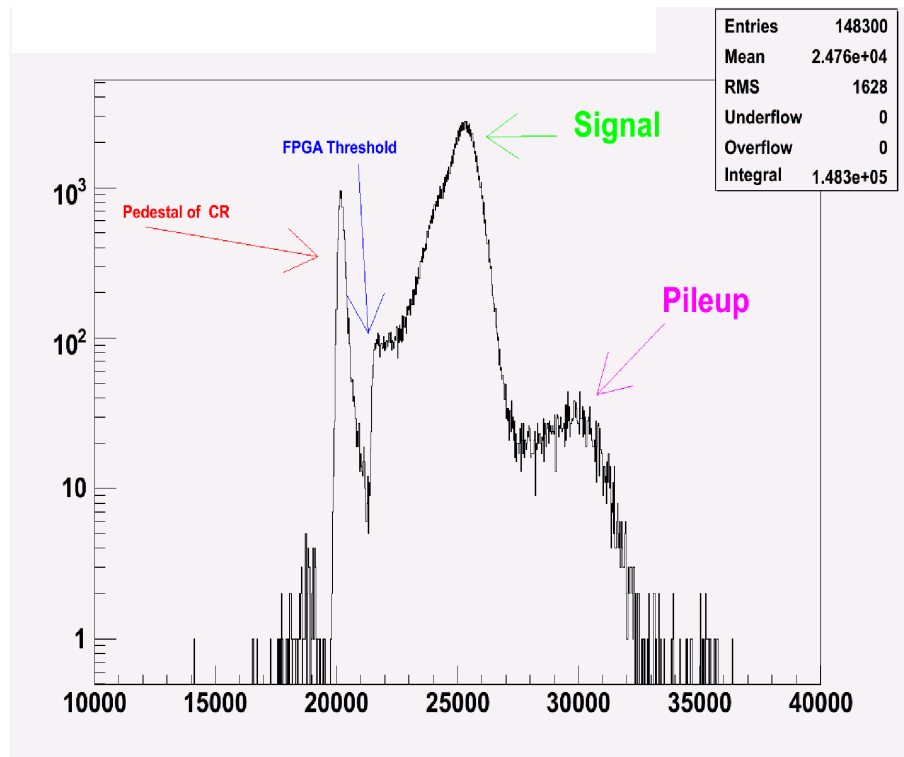
FIG. 3.14: Histogram of total energy deposit in all four blocks of right arm calorimeters.

3.5.7   Old DAQ and FADC Differences

The old and FADC DAQs have some differences. First difference is that the FADC generates the data trigger by summing the area under the digitized pulse for all the eight calorimeter blocks, then it checks this area against a threshold value. On the other hand Old DAQ just checks the pulse height against a threshold value. So in FADC if a Moller event is distributed over all the eight blocks the FADC will still count it while the same event can be missed by old DAQ. There is another trigger related difference. FADC triggers on either left single, right single or coincidence Moller elector ns while old DAQ triggers only on the left arm and

then look for the single left, single right or coincidence Moller events.

Moller FADC DAQ was installed in hall A in June 2009 before HAPPEX III. During the running of HAPPEX III and PVDIS we found that FADC DAQ had 5 percent high single and coincidence rates as compared to the old DAQ. There was a 5 percent asymmetry difference between old and FADC DAQ. We performed a threshold scan for old DAQ and found that the trigger threshold of old DAQ was higher than the FADC and old DAQ was cutting a portion of signal pulses from the PMTs. In order to make the two rates same we need to make correction to the rates of FADC DAQ by taking account of the high threshold of old dAQ. First we plot the energy deposit histograms of old and FADC DAQs in left arm of calorimeter blocks on the top of each other, see figure 3.18.
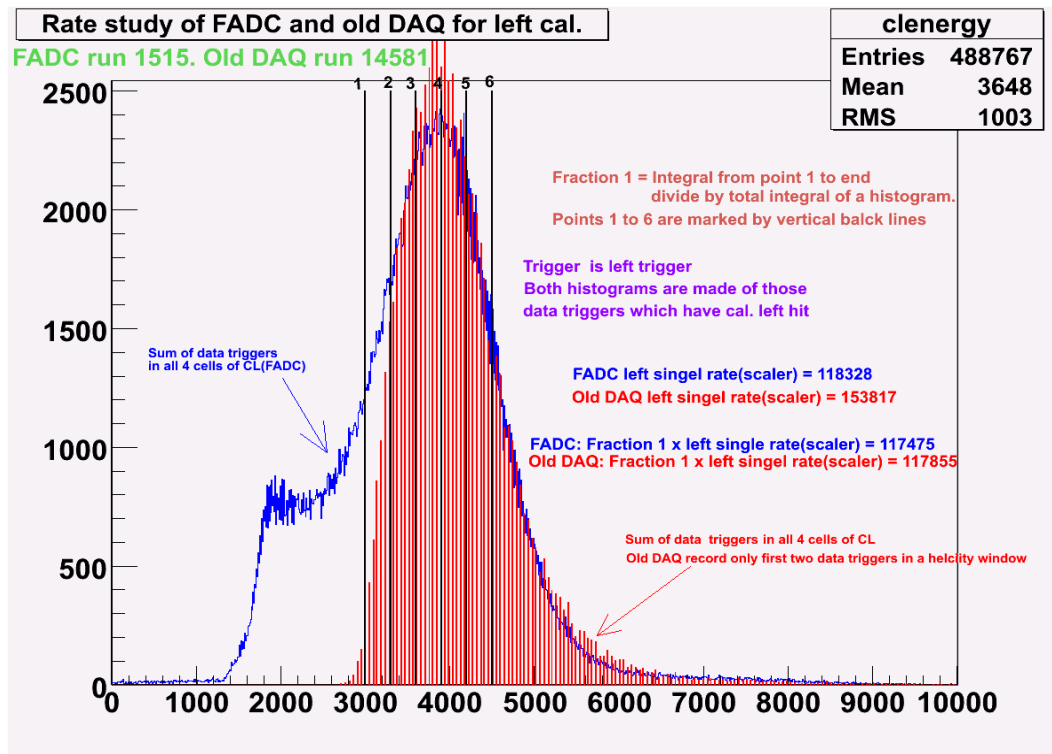
FIG. 3.15: Rate comparison of old and FADC DAQs after taking account of the threshold difference.

Blue histogram is for FADC and red is for old DAQ. The red histogram is scaled such that the median and trailing curve of the two histogram were matched.

Now we can see that the threshold of old DAQ is higher than FADC. This is the reason that FADC has higher rates than old DAQ. A correction for this difference was made. The vertical black lines show the point where a cut is put on the signal of FADC DAQ. The fraction 1 is the integral of blue(FADC) histogram from black line 1 to the end divided by the total integral of blue histogram. Then in the same way we calculated the fraction 1 for red(old DAQ) histogram. Multiply the fraction 1 of blue histogram with the single left rate of FADC DAQ and multiply the fraction 1 of the red histogram with the single left rate of old DAQ. The old DA Q's rate after multiplying with its fraction 1 is 117855 Hz and the FADC DAQ's rate after multiplying with its fraction 1 is 117475. This is an excellent agreement. The same procedure is performed for right arm single rates. We used only scaler data for this correction because old DAQ uses scalers to measure the rates. After fixing the threshold we used new threshold values of FADC on left and right arms which are closed to the old DAQ values and then we measured the FADC coincidence rates with new threshold values using the data triggers. The results are given in table below and the agreement is good. FADC runs are 1515, 2045 and 2048. Old DAQ's runs are 14581, 14661 and 14664.

Single Left Rates(Scalers)	Run 1515 and 14581	Run 2045 and 14661	Run 2048 and 14664
FADC Rate × Frac1	117475	220906	216804
Old DAQ's Rate × Frac1	117855	219973	217861
Single Right Rates(Scalers)			
FADC Rate × Frac4	112518	206574	204441
Old DAQ's Rate × Frac4	109871	209078	2061911
Coincidence Rates(Data Triggers)			
FADC	15267	24859	19292
Old DAQ's Rate	14597	25357	20390

In the last section of the table above we should have appropriate value of coincidence prescale which is at least 5. For prescale values 5 or more scaler rates and data trigger rates are in good agreement with each other and these results are shown in section 3.7.

3.6   Moller Polarimeter Systematic Errors

In this section the details of each systematic error are given. All the systematic errors for old and FADC DAQs are same except the dead time. FADC DAQ worked as parasite DAQ and final beam polarization measurement is given by old DAQ. Moller spectrometer with QQQD configuration gives an analyzing power close to $-\frac{7}{9}$. For precise measurements of beam polarization GEANT simulations are used to make an estimation of the systematic errors. These systematic errors are discussed below.

3.6.1 LevChuk Effect

In 1994 L. G. Levchuk pointed out the possibility of a systematic error in Moller polarimeters known as Levchuk effect[72]. Pure iron foils are used in most of the Moller polarimeters including hall A. The incoming beam electrons scatter from motionless electrons of the target. Its quite possible that beam electrons also scatter by inner shells(K and L) electrons of the target. For those electrons which are scattered by the electrons of the inner shells of the target the intra atomic motion of target electrons can cause a deviation of analyzing power from its maximum value. A deviation of analyzing power from its maximum value may result in a false polarization measurement. Levchuk effect depends upon target thickness, polarimeter acceptance, magnetic optics and electron beam. The reference [73] describes in details about the Levchuk effect to hall A Moller polarimeter. For PREx it is estimated that Lef check roor is 0.5%, see the figure below.
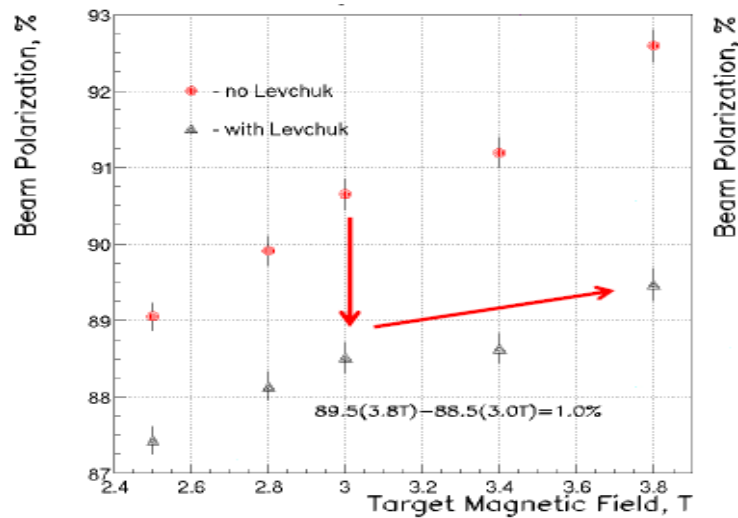
FIG. 3.16: Beam polarization vs target magnetic field with and without Levchuk effect.

3.6.2   Targets Polarization Discrepancy

We use four iron foils with different thickness to measure the beam polarization. These foils are 99.86% pure iron. Polarization measurements by these four foils are different and it resulted in a 0.5% systematic error of the moller polarimeter.
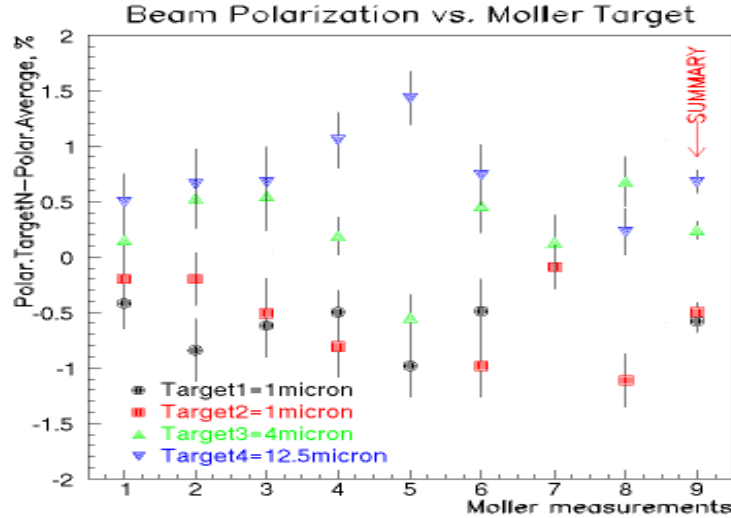
FIG. 3.17: Target polarization difference for different target foils.

3.6.3   Target Saturation

The Moller polarimeter was upgraded to use the brute force method to saturate the target foil by applying a very high magnetic filed of 4 T. This magnetic filed of 4 T is applied with the help of a superconducting solenoid. This set up, taken from hall C was reported [74] that the foils saturate at magnetic field of 3.75 T. But when we actually made this target saturation measurement during the PREx, we found that we might be sitting just at the edge of saturation and thus we had a systematic error due to target saturation.

Right after PREx we had a test run of APEx and then the experiment DVCS. For DVCS we used new target foils, which are 99.96% pure iron and they showed a clear saturation of iron target.
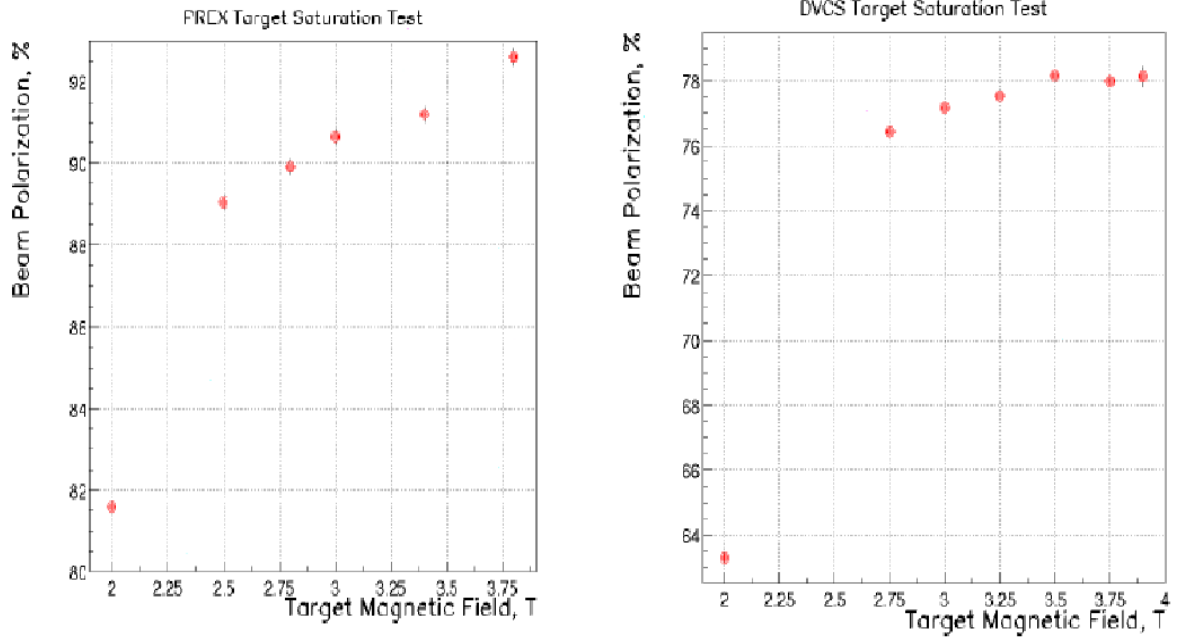
FIG. 3.18: Left(PREx): Beam polarization of target vs. magnetic field of superconducting solenoid. Right(DVCS): Same plot as left but with new target foils.

3.6.4 Analyzing Power

Moller spectrometer has (Q1)(Q2)(Q3)(D) configuration and designed to get maximum analyzing power $-\frac{7}{9}$ in center of mass frame for coincidence Moller scattered electrons. GEANT simulations are used to get the analyzing power for a particular beam energy of an experiment. Historically the systematic error of analyzing power is $\pm 0.3\%$ and it is a measure of the difference between GEANT and real data. The difference between GEANT and real data is due to drift of power supplies of quads and dipole. Other possible reasons are target position, beam position and quad position etc. During the PREx we observed a difference between GEANT and real scan of coincidence rate vs. magnetic filed of quads Q1 and Q3. It is called quad shift(figure below).

This shift exists for superconducting target and room temperature target. This shift is observed at different beam energies. The quads power supply current and
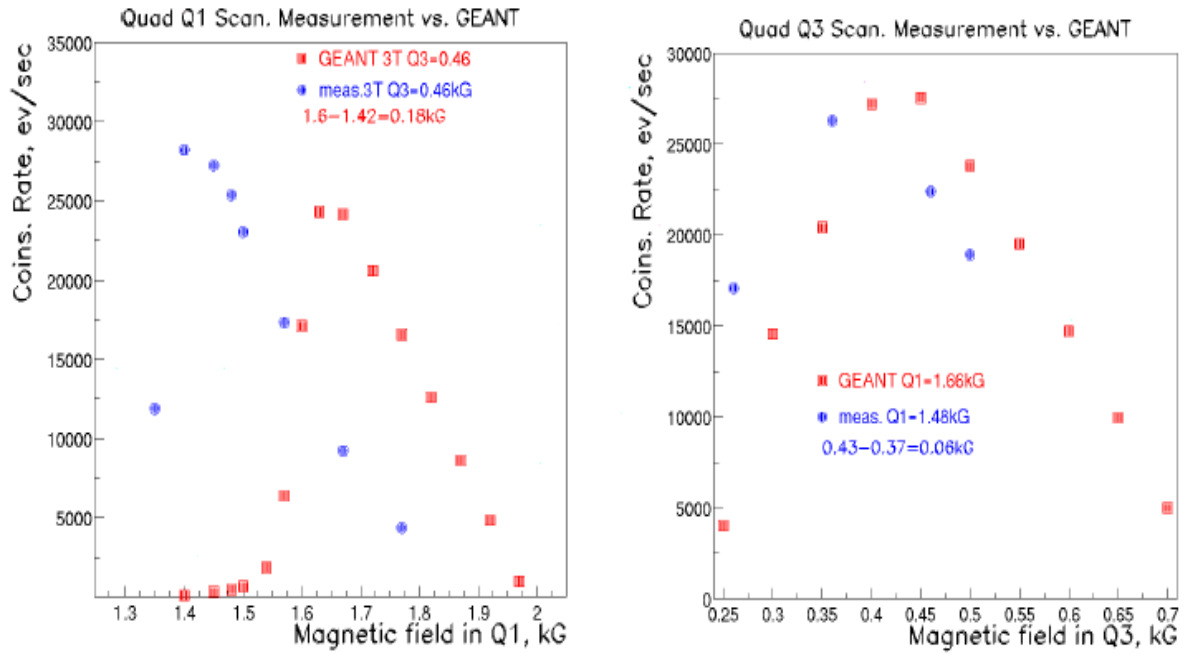
FIG. 3.19: Left: Coincidence rates vs Q1 magnetic filed. Right: Coincidence rates vs Q3 magnetic filed. Red squares are GEANT simulation and blue circles are real scans.

the value of current read out are same. This shift was a surprise and best guess for this shift is due to the difference between real value of $(B \times d \times l)$ and the value used in GEANT. In Moller polarimeter the regions close to the end of quads are sued for focusing purpose where as we think that the GEANT uses the central region of quads. The systematic error comes from the accuracy of the peak in figure 3.20. For the purpose of focusing quadrupole Q1 is more important than Q3. The disagreement between GEANT and real scan for Q1 is 0.18 kG and for Q3 the difference is 0.06 kG. The Q1 settings for PREx is 1.66kG and Levchuk effect is estimated for 1.63kG, 1.66kG and 1.69kG. For these three values of Q1, using the GEANT simulation, the analyzing power is plotted vs magnetic of super conducting solenoid at the target. This gives us a reasonable estimate of systematic error of analyzing power which is $\pm 0.3\%$.
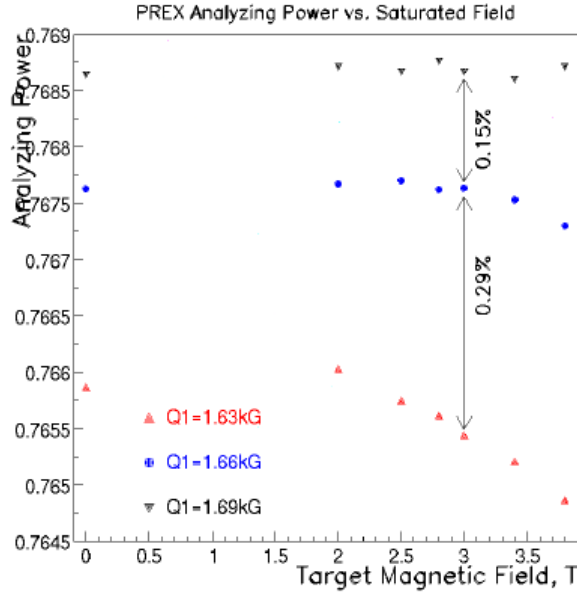
FIG. 3.20: Left: Coincidence rates vs Q1 magnetic filed. Right: Coincidence rates vs Q3 magnetic filed. Red squares are GEANT simulation and blue circles are real scans.

3.6.5 Target Temperature

The systematic error due to target temperature is estimated with the numerical calculation of two dimensional heat equation.

$$\partial T/\partial t = \bigtriangledown^2 T \kappa/(\rho C_P) - 2\sigma\varepsilon((T+T_0)^4 - T_0^4)/(\triangle z \rho C_P) + B_{flux}\alpha/C_P, \qquad (3.8)$$

where $\kappa = 0.75 W/cm/K$ is thermal conductivity for iron, $\rho = 7.87(8.14)g/cm^3$ is the density of supermendur target, $\sigma = 5.67 \times 10^{-12} W/cm^2/K^4$ is the Stefen-Boltzmann constant, ε is foil emissivity which depends upon surface structure and may range from 0.005 for polished surface and 0.8 for rough surface. The value of ε we used is 0.1, $T_0 = 300$ K which is outside temperature, $\triangle z$ is foil thickness, B_{flux} is the density of beam flux, $\alpha = 1.5$ MeV/(g/cm^2) is the energy deposit by one minimum ionizing particle and $C_P = 0.4$J/g/K is the specific heat of iron target. The target temperature systematic error is 0.02%. The last systematic error, target foil polarization is estimated to be 0.25%.

3.7 FADC Analysis and Results

3.7.1 Stability of FADC

Flash ADC is cutting edge device built at Jefferson lab. FADC based data acquisition system is installed right before HAPPEX III. In this section important characteristics of FADC are discussed and then final asymmetry calculation is presented. It is shown [75] that FADC is very stable to measure rates and asymmetry even in very high background.
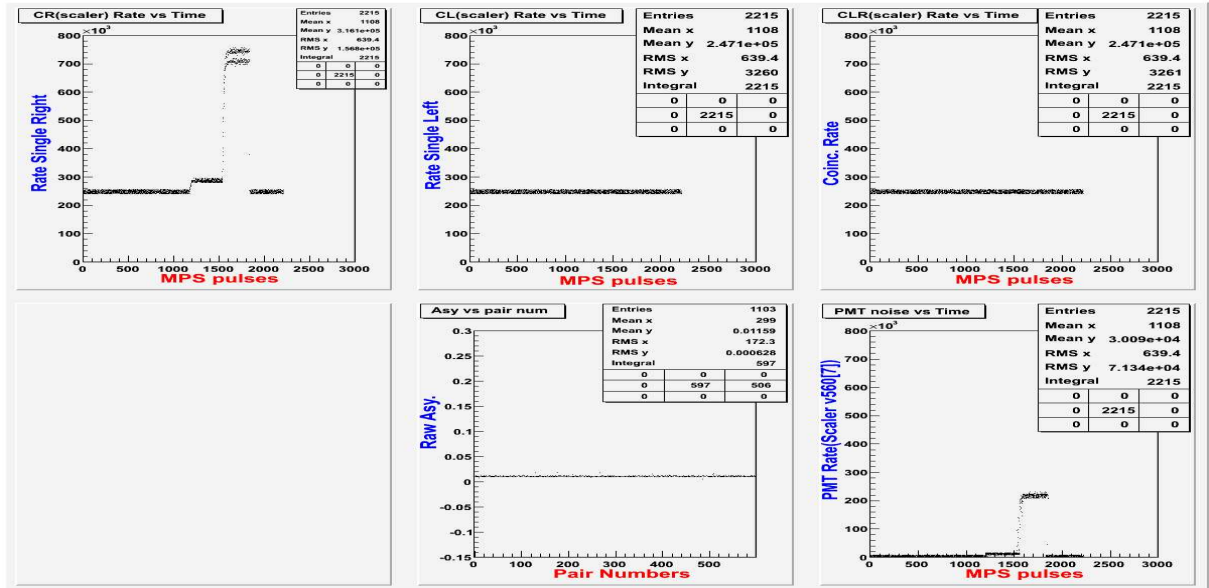
FIG. 3.21: Results of FADC pulsar test.

Figure 3.21 shows the stability of FADC in high background. The outputs of an asymmetry module which can produce an asymmetry of 0.11ppm are connected to one left and one right calorimeter LEMO inputs of FADC. A PMT is used as a background source and is connected to another right LEMO input. In all the graphs of figure 3.21 horizontal axis is the number of MPS pulses. Around MPS pulse number 1200 we turned on the PMT and we can see that in upper left graph the rates get higher. Then around the MPS pulse number 1500 the gain of PMT was

increased and a big jump in single right rates(upper left plot) can be seen. At this point the PMT background is as high as 250 kHz and yet the coincidence rate(upper right) plot and the asymmetry vs. PMS pair number(lower middle) plots are stable. So FADC can work very well in high background.

3.7.2 Spin Dance Result

During the commissioning period of an experiment **spin dance** measurement is performed to get the appropriate settings of wien filter for optimum longitudinal polarization in the hall. Spin dance of PREx is performed on April 5th and with the help of Moller polarimeter we found the appropriate value of wien filter. In the figure 3.22 the fit to polarization vs. wien angle is shown using the FADC DAQ.
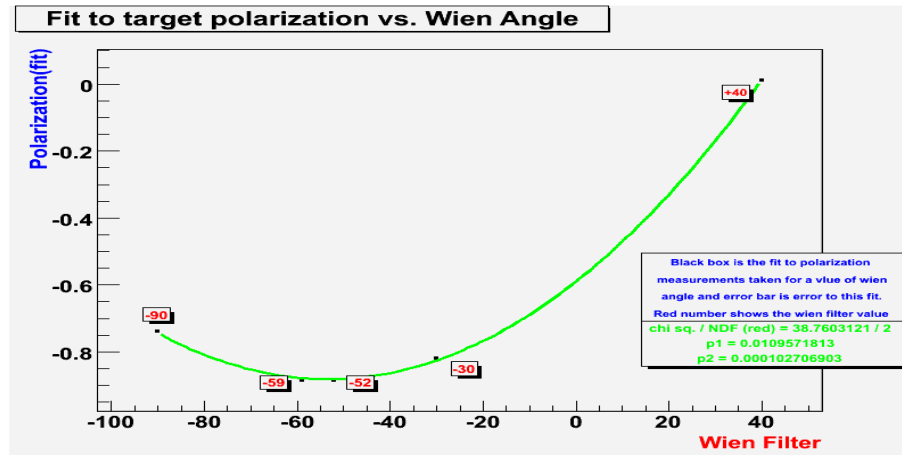
FIG. 3.22: FADC spin dacne fit.

3.7.3 Scaler and Data rate comparison

If a prescale value less than 5 is used then the dead time of FADC plays a role and scaler rates differs from data trigger rates. For appropriate coincidence prescale values, the scaler rates and the data trigger rates are same.

For the following table **Coincidence Prescale = 10**

Run No.	Target	Beam Current	Single Left Scaler vs Data	Right Left Scaler vs Data	Coin Scaler vs Data
1353	1	3.1 uA	113000 - 114000	87540 - 85860	13130 - 13070
1370	2	3 uA	202300 - 199200	154500 - 151400	23800 - 23880
1373	2	3 uA	202100 - 199000	154400 - 151300	23720 - 23800
1322	3	1.2 uA	341900 - 340500	242100 - 240600	21310 - 21270
1321	4	1.2 uA	342100 - 339600	242800 - 240300	21620 - 21600
1553	5	0.4 uA	244560 - 241860	214210 - 214440	25540 - 25520
1554	6	0.4 uA	252700 - 249870	222110 - 219500	27160 - 27160

For the following table **Coincidence Prescale = 5**

Run No.	Target	Beam Current	Single Left Scaler vs Data	Right Left Scaler vs Data	Coin Scaler vs Data
1375	2	3 uA	200400 - 195100	153200 - 147900	23500 - 23500
1374	2	3 uA	201500 - 196000	153900 - 148500	23680 - 23690
1355	1	9 uA	324600 - 313700	251600 - 148500	41230 - 40930

3.7.4   FADC and Old DAQ Delayed Time

Flash ADC has sampling time of 4 nsec. It is shown by Roman Pomatsalyuk [76] that FADC takes about 150 nese to respond to first data trigger when the prescale is set to one. The FADC internal time 250 MHz time clock is used to find the time intervals between data triggers. Time interval distribution of FADC data triggers is shown in figure3.24. It is a Poisson distribution. In the left graph of 3.24 the horizontal axis is time axis which goes from 0 to 250×10^3 nano sec.

In the right graph we zoomed into the region from 0 nano sec to 500 nano sec and we can see that FADC starts counting after 150 nano sec. As mentioned, the
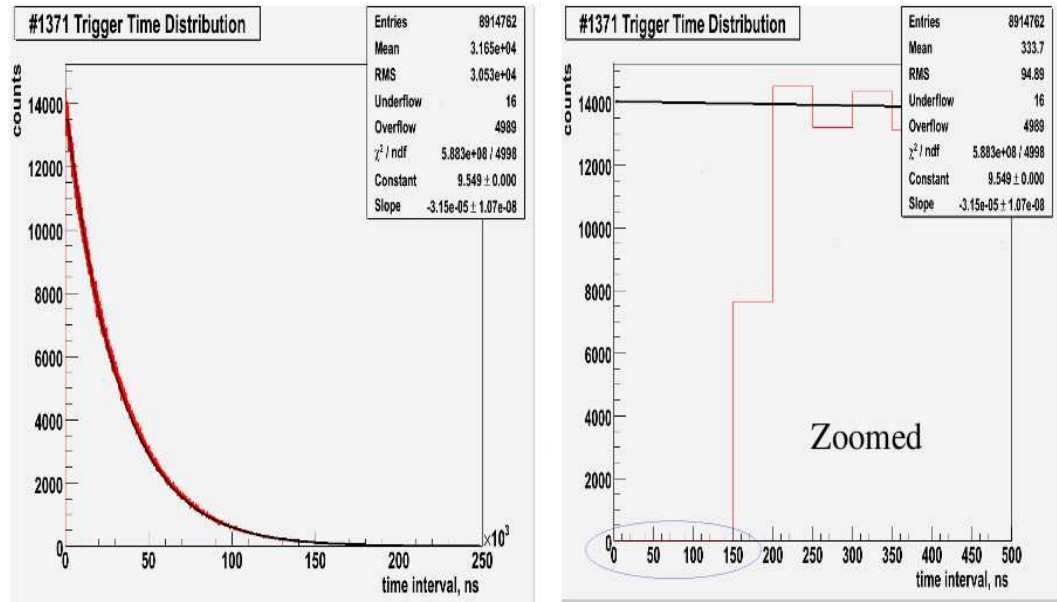
FIG. 3.23: FADC delayed time.

sampling time of FADC is 4 nsec so we believe that this 150 nsec delay is due to FPGA. The delayed time of old DAQ is 0.3% and for FADC DAQ we may neglect the delayed time systematic error.

3.7.5 Data Triggers and Scalers Asymmetry

In the subsection 3.7.3 it is shown that for appropriate precalse values the FADC is internally consistent. The second check is to compare the asymmetry measured by data triggers and by the scalers.

Asymmetry measured by scaler is 0.0515 ± 0.00023 and by the data triggers is 0.0512 ± 00034, which is almost the same. The spikes in data trigger asymmetry are because of prescale value.

3.7.6 FADC and Old DAQ Raw Asymmetry

The target was set for the FADC DAQ to get the same asymmetry as of old DAQ. The raw asymmetry in the old DAQ is measured by a super coinciding scaler
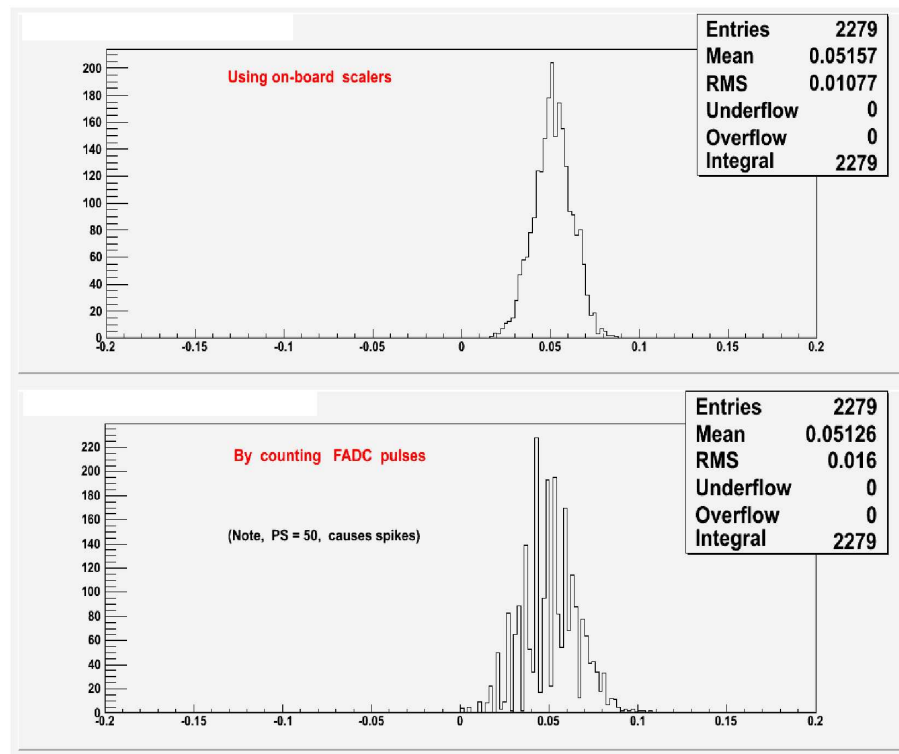
FIG. 3.24: Top: Asymmetry by onboard scalers.
Bottom: Asymmetry by data triggers.

CL-CR-SL-SR. Old DAQ takes only first two data events in a given helicity state. By the middle of PREx run we were able to remove all the problems of FADC DAQ. The final beam polarization results are given my old DAQ but FDAC DAQ is fully operational. The Following graph shows an excellent agreement between FADC and old DAQ.

In the figure 3.25 we tried to make the conditions for two DAQs exactly the same. Red triangles are Old DAQ runs and blue boxes are FADC runs. These old DAQ and FADC DAQ runs are taken at the same time. These are the selected runs of beam polarization measurements taken on April 28th, May 5th and May 8th 2010. The error bars on FADC runs are larger than old DAQ because only those FADC runs are taken which started after and ended before its corresponding old DAQ run. This procedure is adopted in order to make conditions exactly the same. Same signal from calorimeters and scintillators is split for old DAQ and FADC DAQ. This
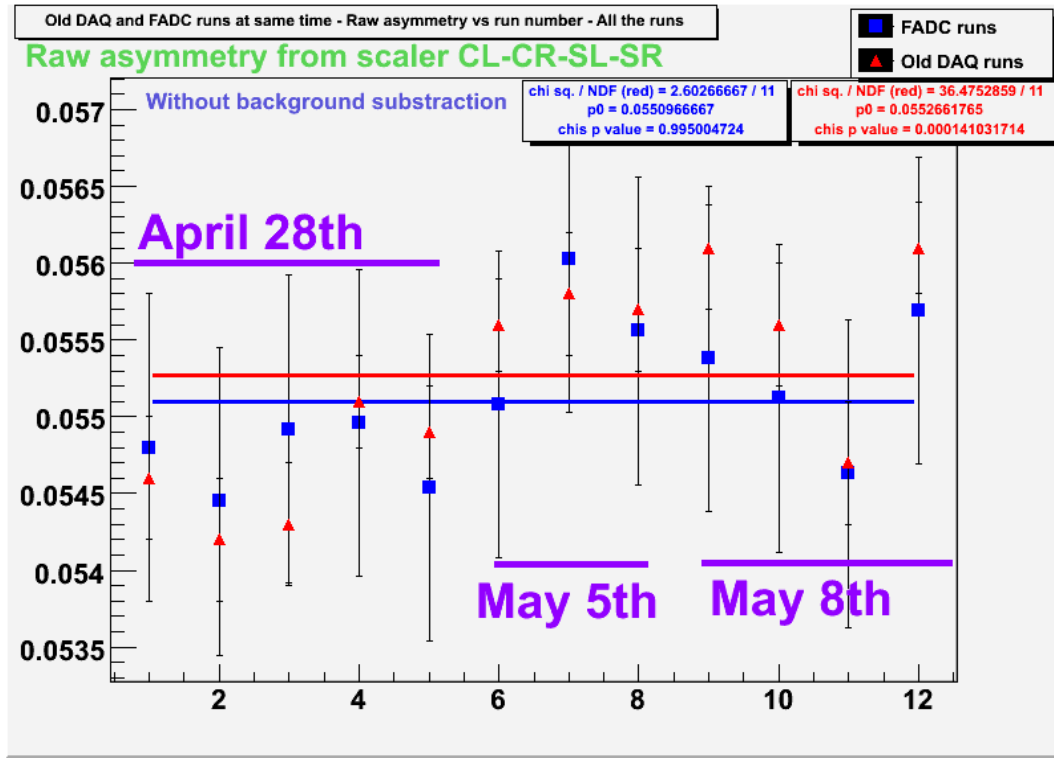
FIG. 3.25: FADC and Old DAQ asymmetry agreement.

graph shows the asymmetry without background subtraction. Figure 3.25 shows the raw asymmetry measured by two DAQs. The blue line is a fit to the FADC runs and the average FADC DAQ raw asymmetry is 0.0551 ± 0.0003. The red line is a fit to the old DAQ runs and the average old DAQ raw asymmetry is 0.0553 ± 0.0001. The final beam polarization of PREx measured by Moller polarimeter is

$$(90.32 \pm 0.07(\text{stat}) \pm 1.12(\text{sys}))\%, \tag{3.9}$$

An independent beam polarization measurement is made by Compton polarimeter. Two polarimeters are used to cross check the beam polarization. Beam polarization measured by Compton polarimeter is $(88.20 \pm 1.2(stat) \pm 1.2(sys))\%$. For PREx we used the averaged beam polarization measurements of Moller polarimeter and Compton polarimeter.

CHAPTER 4

PREx Analysis

4.1 Introduction

This chapter describes the data acquisition and parity analysis of PREx. PREx is a parity violation experiment and we used standard same data acquisition and analysis method which is used for earlier experiments HAPPEX, HAPPEX II, HAPPEX III and PVDIS. This chapter describes how we extracted the physics asymmetry from measured asymmetry. A short description of Q^2 measurements are also given. Helicity correlated position differences and charge asymmetries are measured. Longitudinal polarization of incoming electrons is flipped at 120 Hz rate. An insert able half wave plate and a double wien flip is used for passive sign ch age of helicity. The physics asymmetry is given by[77]:

$$A_{PV} = \frac{K}{P_b} \frac{(A_{corr} - F - T) - P_b \sum_i A_i f_i}{1 - \sum_i f_i},$$

(4.1)

where P_b is the beam polarization, K is the finite kinematic acceptance, F is the false beam asymmetry, T is the transverse asymmetry, f_i is the fraction associated withe th back ground asymmetry A_i and A_{raw} is the asymmetry measured by the

detector.

4.2   Data Acquisition

The details of hall A data acquisition(DAQ) system is given in [78] and here a simple description of the DAQ is given here. The hall A DAQ consists of electronics and CEBAF online data acquisition system(CODA)[79]. Hall A DAQ electronics include front-end fast-bus ADCs, TDCs and scalers, 100BaseT ethernet, UNIX or LINUX workstations and a mass storage data tape silo(MSS). The CODA group of CEBAF developed the trigger supervisor[80]. CODA has a read out controller(ROC). an event builder(DB) and an event recorder(ER). For each triggers generated by trigger supervisor the corresponding data of this particular trigger is gathered by the ROC. ROC buffers this data and then sends these buffers to EB on a workstation with the help of network. The EB builds the eve ts from all different ROCs and sends then to the ER, then ER writes down this data on a local disk. The data acquisition system of hall A for parity experiment PREx has two modes of operations which are explained below.

4.3   Counting Mode

For Q^2 measurements, study of scattering of inelastically scattered electrons and for the alignment of the elastic peak we use counting mode. Counting mode requires to operate at very low currents. Vertical drift chambers(VDCs) are used to precisely see the trajectories of the scattered electrons. Counting mode provides the reconstruction of the tracks of scattered electrons from focal plane to the target. S2 scintillator and a 1024 Hz clock are used for trigger. Counting mode trigger system consists of CAMAC and NIM modules which are discriminators, delay units, logic

units and memory lookup modules. For current monitors voltage to frequency(V2F) converters are used.

4.4   Integrating Mode

Integrating mode of hall A DAQ is used for the asymmetry measurements. The helicity state is determined by an electronic module at polarized source set up. The helicity state is changed at 120 Hz rate and this information of helicity is not sent to anywhere. The actual helicity state is delayed by 8 helicity windows in order to minimize the cross talk. The helicity state of first window is pseudo random. A helicity sate is held for 8.33 msec and then a MPS pulse is released for 300 μsec. The quadruplet pattern of helicity states has two orientations:

1) $- + + -$

2) $+ - - +$

The same 60 Hz phase of quadruplet and the power line removes the electric power noise from asymmetry measurements. Two helicity states with opposite signs define the helicity pair. Helicity pair is used to calculate the asymmetry. There is a pairsync signal which differentiates the first and second helicity windows with in a helicity pair.

During a helicity state electrons hit the target. Elastically scattered electrons hit the PREx detector. With the help of ADCs connected to the PREx detectors we integrate the detector signal for this particular helicity state. For a short period of time when MPS pulse is ON the parity DAQ stops and integrated values are transferred and recorded. After MPS pulse the DAQ is ready for integration for next helicity state. The MPS pulse acts as a trigger for integrating mode of parity DAQ.
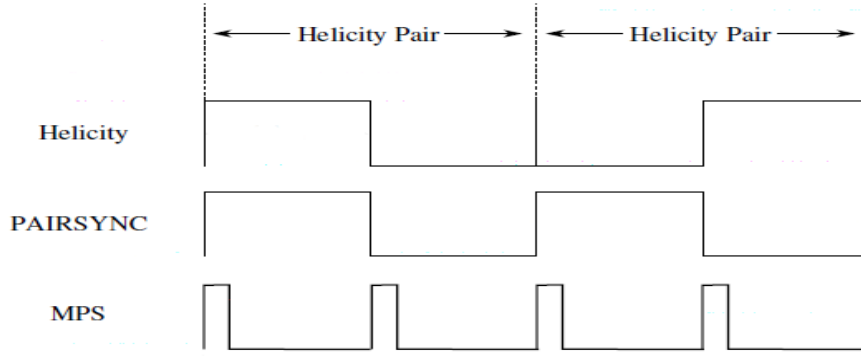
FIG. 4.1: MPS, PAIRSYNC and Helicity signals.

4.5 Parity Analysis

Parity data analyzer(PAN)[81] is written in C++ and it uses ROOT[82] libraries. The raw files generated by hall A DAQ are input to the PAN and PAN simply decodes these files. PAN requires a database file which has the data map of all the ADCs, Lumi monitors, current monitors, position monitors and other DAQ modules . Database file also has the values of cuts and pedestals. PAN subtracts the pedestals and DAC noise from ADC and scaler values, it also removes the 8 window delay of helicity state and finally PAN calculates the asymmetries and differences for helicity window pairs. The output of the PAN analysis is a root file. The root file has a Raw tree which has the decoded DAQ data for each helicity window. Pair tree and multiplet tree have the helicity correlated asymmetries and differences for helicity pairs and helicity multiplets respectively. One multiplet is consist of two adjacent helicity pairs. The asymmetry of a helicity pair is given by

$$A_{pair} = \left(\frac{\frac{D_R}{I_R} - \frac{D_L}{I_L}}{\frac{D_R}{I_R} + \frac{D_L}{I_L}} \right), \tag{4.2}$$

where R and L are two helicity states, D_R and I_R are the integrated signals of detector and current monitor respectively for helicity state "Right". PAN also mea-

sures the charge asymmetries and position differences. In order to avoid any human error, it randomly adds one sigma factor to the asymmetries, known as blinding. When we find all the normalization factors and all of our cuts are legitimate, then we just disable one string in the database file which removes this one sigma deviation and we get our final numbers.

4.6 Data Cuts

PAN do all kind of checks which are necessary to make the data clean and avoid any error. These checks are defined in database file as data cuts. For example if the beam drops during a CODA run then PAN does not include the beam which is below a certain value of ADC channel. If there is a sudden change in beam position, known as burp then PAN also cuts the events of burp region. Following graphs shows two examples of cuts.
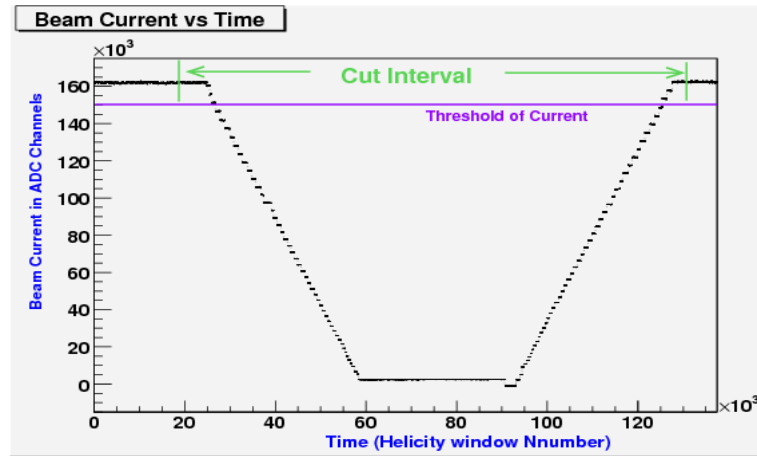
FIG. 4.2: Beam current cut

These are the cuts defined inside parity analyzer and other than these cuts we also removed the data during which we had any equipment malfunction. If a spectrometer's magnet trips or if we have any test run we removed it from our production data. Other than these beam related cuts PAN also takes care of the
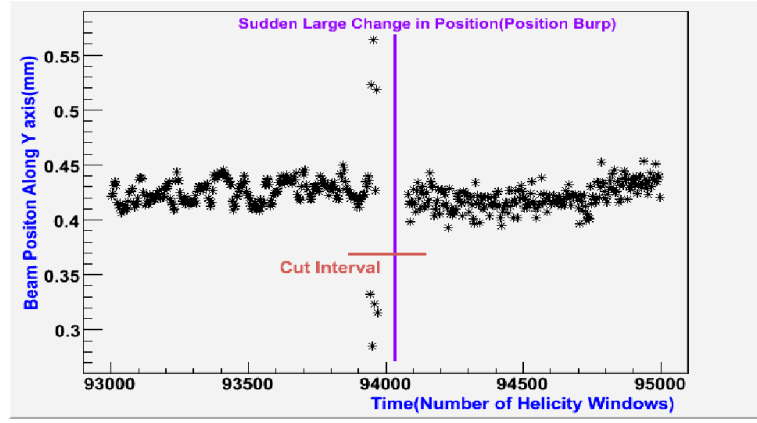
FIG. 4.3: Position burp cut.

DAQ signals and checks if there is a glitch in any ADC or scaler. All these cuts are summarized in the table below:

Cut Name	Threshold	Extent lo	Extent hi
(1) Low Beam	120000(ADC)	40	5000
(2) Beam Burp	2050(ADC)	40	40
(3) Event Sequence	-	25	25
(4) Pair Sequence	-	25	25
(5) Start up	-	0	0
(6) Monitor Saturation	500000(ADC)	30	30
(7) ADC Burp	100(ADC)	10	10
(8) Bad Scaler Value	-	1	1
(9) Beam Energy Burp	0.2267(mm)	100	1000
(10) Beam Burp RMS	-	40	40
(11) RMS of Double Difference	540(ADC)	120	120
(12) Position Sat RMS	50(ADC)	60	40

4.7 Raw Asymmetry

The PREx is designed to measure the Physics Asymmetry which we get after normalizing the measured asymmetry of the detectors. Measured asymmetry of the detectors is called raw asymmetry. We have total four detectors and the final number of raw asymmetry is the average asymmetry of four detectors. The final raw asymmetry is calculated this way: If G^L and G^R are the integrated signal of a detector for helicity state left and right respectively then asymmetry of this detector is given by

$$A_{rawofonedetector} = \frac{G^R/I^R - G^L/I^L}{G^R/I^R + G^L/I^L},$$ (4.3)

where I^L and I^R are the integrated current signals for helicity state left and right respectively. For measured asymmetry from four detectors we have to take care of three issues: the gain difference of PMT tubes, different number of electrons going into the detectors for each helicity sate and the different amount of current for each helicity state. So each detector must be weighted for these three factors. First we normalize the integrated signal of a detector for a single helicity window by the amount of current in that particular helicity window, $S_i = G_i/I$. Since the gain of PMT tubes can be different so we normalize S_i to average detector signal, $< S_i >$. If we plot the histogram of pairwise asymmetry of one detector the width of distribution is given by $\sigma_i = 1/\sqrt{N_i}$ where N_i is the total number of electrons hitting the detector "i", in on pair of helicity windows. The statistical weight for one detector is $1/\sigma_i^2$. So the final weight of a detector is:

$$w_i = \frac{1}{< S_i > \sigma_i^2},$$ (4.4)

Next we normalize the weight of each detector by sum of weights of all the four detectors:

$$W_i = \frac{w_i}{\sum_i w_i}, \tag{4.5}$$

So the final raw asymmetry is given by:

$$A_{raw}^{alldet} = \frac{(\sum_i S_i W_i)^R - (\sum_i S_i W_i)^L}{(\sum_i S_i W_i)^R + (\sum_i S_i W_i)^L}, \tag{4.6}$$

4.8 Passive Helicity Reversal

For good Lead production data of PREx we changed the helicity at the rate of 120 Hz. This is called fast helicity change. We also have an insertable half wave plate in the path of LASER and a wien filter. IHWP and double wien filter can flip the overall sign of helicity state. The analyzer and DAQ do not have the information of this change of helicity. Half of the data is taken with overall sign plus and half of the data is taken with overall sign negative. So when we add these two data sets together we get the cancellation of any helicity correlated beam systematics. For the final asymmetry calculations we have to make a sign correction for IHWP and wien states.

4.9 Position Differences and Charge Asymmetry

We can get a false asymmetry if the helicity correlated beam position difference or the charge asymmetry is large. The parity violating cross section and electron rate at detectors depends upon these two beam conditions. During the PREx we successfully kept the helicity correlated position differences and charge asymmetry small. After making the sign correction for IHWP and wien, following figures shows that the charge asymmetry4.5 and position differences**??** are very small.
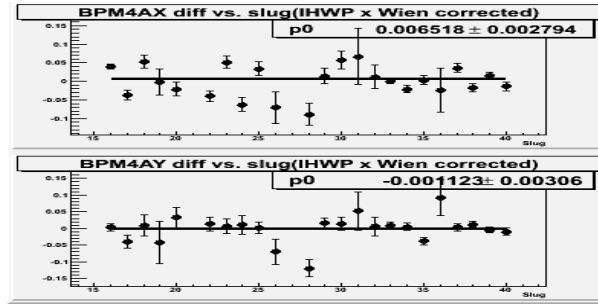
FIG. 4.4: IHWP and Wien corrected helicity correlated position differences measured by BPM 4ax and BPM 4ay.
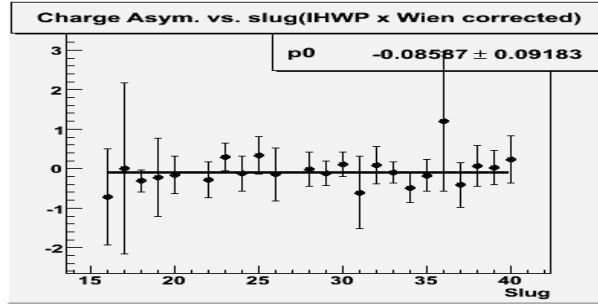
FIG. 4.5: Helicity correlated charge asymmetry of BCM1.

Detector signals are already normalized by the cahrge asymmetry. We need to make correction for helicity correlated position differences which is given by:

$$A = A_{raw} + \sum_{i=1}^{5} \beta_i \triangle x_i, \qquad (4.7)$$

where the summation is over five position monitors 4ax, 4ay, 4bx 4by and 12x. These five monitors measures the beam position, angle and energy at target. β_i are the response of a detector to each of these monitors. Beam modulation and regression analysis is used to find out the β_i.

4.10   Detector Pedestals

Pedestal is the electronic noise in a channel of an ADC when no signal is going into this channel. One CODA run is almost one hour long and during the PREx we took 64 pedestal runs. The purpose of the pedestal runs is to see if there in any

drift in pedestal over the time and make sure that the detector pedestals are stable. Figure 4.6 shows that our detector pedestals are very stable.
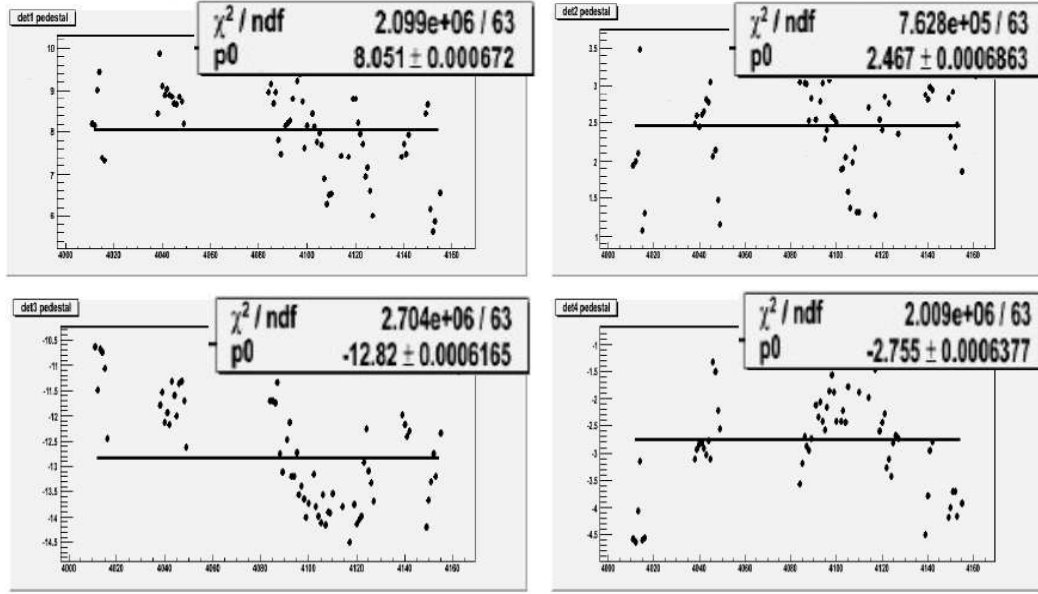
FIG. 4.6: History of pedestals of four PREx detectors.

The detector signal is of the order of 100,000 ADC channels and the pedestal of each detector is stable. The next thing is to make sure that the pedestal for each helicity state is same. In the figure 4.7 we measure the helicity correlated difference of pedestals for each pedestal run.
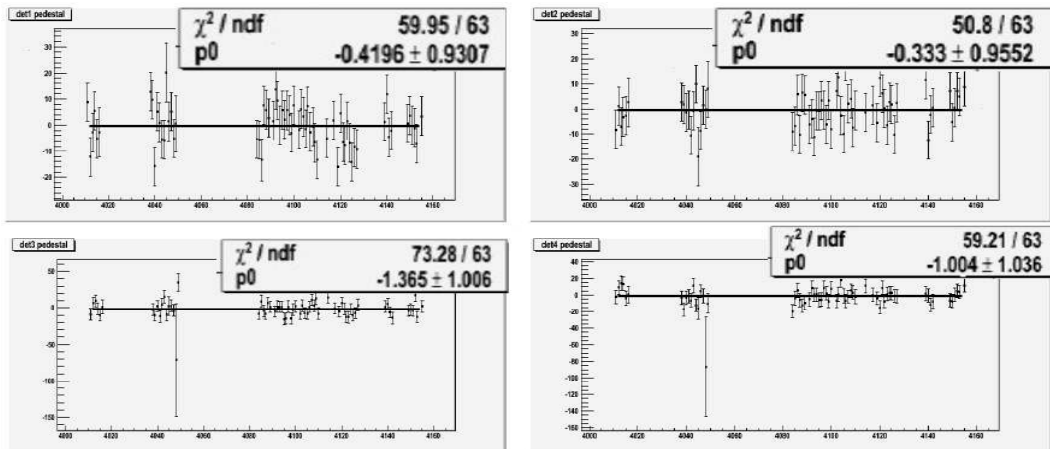
FIG. 4.7: History of helicity correlated pedestal differences.

The parity analyzer PAN measure the helicity correlated differences in the units of milli channels so the real number for helicity correlated pedestal difference of detector one is -0.0004196 $\pm$ 0.0009307 which is almost zero.

4.11   Linearity

PREx measures the asymmetry which is of the order of half part per million. For such small asymmetries we want all of our integrating devices to be linear. A small non linearity can introduce a systematic error. The integrating devices are PREx detectors and beam monitors. Integrated signals from these devices is proportional to the rates measured by them. Lets assume that there is a non linear part in the signal which can be modeled as

$$Signal_R = \delta G + c_1 \times R + c_2 \times R^2, \qquad (4.8)$$

where δG is error in pedestal, R is the rate, c_1 and c_2 are the coefficients of linear and quadratic terms respectively. The signal from current mo niter can be written as

$$C_R = \alpha \times C + D_Q, \qquad (4.9)$$

where α is coefficient of linear term and we assumed that $D_Q = 0$. The raw detector asymmetry is normalized by the beam current is given by:

$$A_R \approx (1 + \frac{c_2}{c_1} \times R + \frac{P}{c_1 R}), \qquad (4.10)$$

It was the goal to keep the slope of normalized detector asymmetry vs charge asymmetry less than than 1%. With $D_Q = 0$ the slope of normalized detector

asymmetry vs charge asymmetry is $\frac{c_2}{c_1}$. The normalized detector asymmetry vs charge asymmetry for slug 16 is figure 4.8.
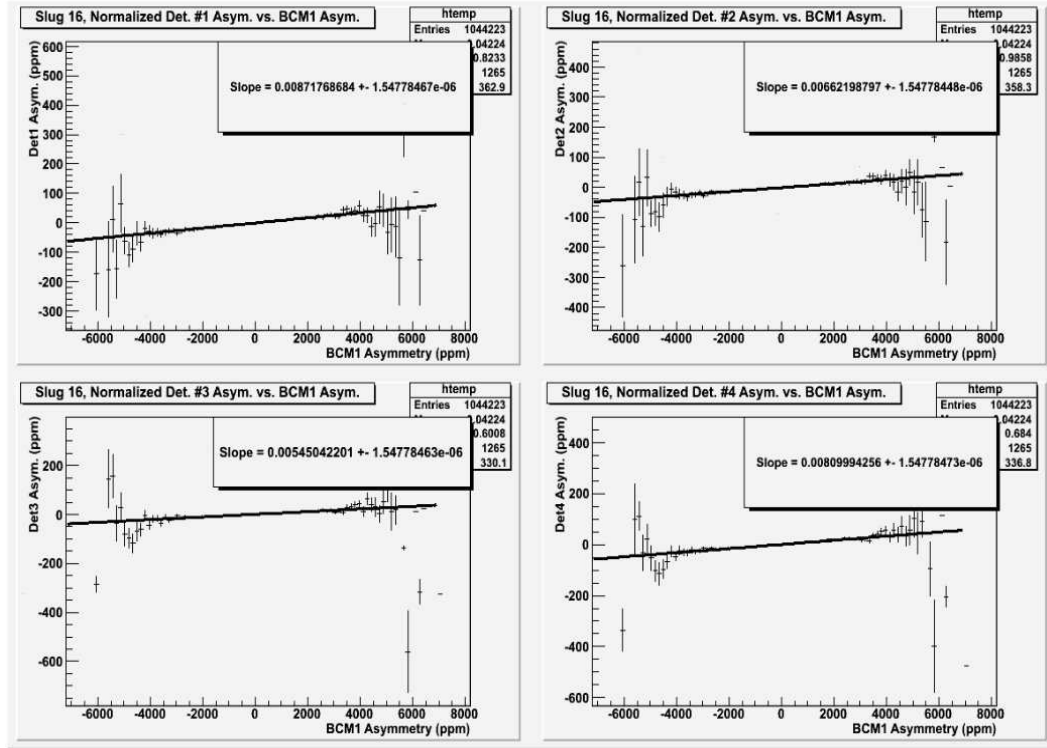
FIG. 4.8: Normalized detector asymmetry vs. charge asymmetry of slug 16.

Figure 4.9 shows that the charge corrected slopes of normalized detector asymmetry v/s charge asymmetry graphs. Horizontal green lines represent the $\pm 1\%$ slopes and blue lines represent the $\pm 2\%$ slopes. PREx average value of charge corrected slopes of normalized detector asymmetry v/s charge asymmetry graphs for all the detectors is less than one.

The maximum non linearity of current monitor is given by the double difference of charge asymmetry of two current monitors. These two monitors are BCM1 and BCM3.
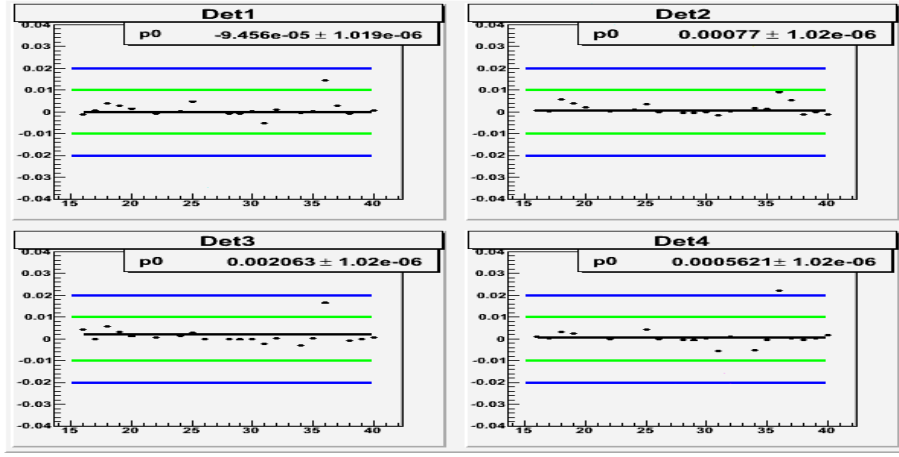
FIG. 4.9: Charge corrected slopes of det Asym. v/s. charge asym.

4.12 Dithering and Regression

Two independent methods are used to measure the response of detectors to the beam monitors. These responses are used to remove the helicity correlated noise of position, angle and energy of the electron beam. Beam modulation method and regression analysis are described in detail in [11] and here a brief description of these two analysis is given. In dithering we deliberately change the beam position and energy for short period of time with the help of eight coils and the response of detectors to monitors is measured. The correction to asymmetry is given by:

$$\triangle D = \sum_{i=1}^{5} (\frac{\delta D}{\delta M_i}) \triangle M_i,$$ (4.11)

Eight coils are used for beam modulation so the response of a detector to the monitors($\frac{\delta D}{\delta M_i}$) is given by:

$$\frac{\delta D}{\delta C_k} = (\frac{\delta D}{\delta M_i})(\frac{\delta M_i}{\delta C_k}),$$ (4.12)

The detector response to monitor($\frac{\delta D}{\delta M_i}$) is obtained by minimizing the chi square with respect to $\frac{\delta D}{\delta M_i}$. In matrix representation it is given by:

$$M_{DC} = M_{DM} \times M_{MC}, \tag{4.13}$$

where

$$M_{DC} = \sum_i \left(\frac{\delta D}{\delta C_i} \frac{\delta M_j}{\delta C_i}\right)/D^2, \tag{4.14a}$$

$$M_{DM} = \frac{\delta D}{\delta M}, \tag{4.14b}$$

$$M_{MC} = \sum_i \left(\frac{\delta M_m}{\delta C_i} \frac{\delta M_n}{\delta C_i}\right)/D^2, \tag{4.14c}$$

Finally the detector response to monitors is given by $M_{DM} = M_{DC} \times (M_{MC})^{-1}$. The matrix M_{MC} is not singular. In regression we use the natural beam motion to measure the response of detectors to the monitors. If y is dependent variable, the detectors and x is independent variable, the monitors then regression simply uses the least square fit method

$$\beta = \frac{\sum_{i=1}^{4}(y_i - <i>)(x_i - <x>)}{\sum_{i=1}^{4}(x_i - <x>)^2}, \tag{4.15}$$

where $y = \sum_i C_k x_k$ and C_k are the coefficients(the response of detector to monitor) given by $C_k = \delta y/\delta x_k$. Similar to dithering the chi square

$$\chi^2 = \sum \left(\frac{y_i - \sum C_k(x_k)_i}{\sigma_i^2}\right)^2, \tag{4.16}$$

is minimized with respect to C_k. Finally we can write

$$\sum_i D(M_n)_i = \sum_j C_j \sum_i (M_n M_j)_{ii}, \tag{4.17}$$

Regression corrected response of detectors to the monitors is given by

$C_j = (\sum_i D(M_n)_i)(\sum_i (M_n M_j)_{ii})^{-1}$. Again in regression analysis the matrix representation is used and that matrix $(M_n M_j)_{ii})$ is not singular. Then the values of regressed and dither corrected asymmetries are checked against each other. Dithering and regression agree with each other very well. The regression analysis make corrections to the asymmetry as mentioned above. Regression analysis reduces the width of Gaussian distribution of asymmetry. Figure 4.10 shows the widths of Lead production slugs before and after regression. Blue points are the width of each production slug after regression and red points are the width of production slugs before regression.
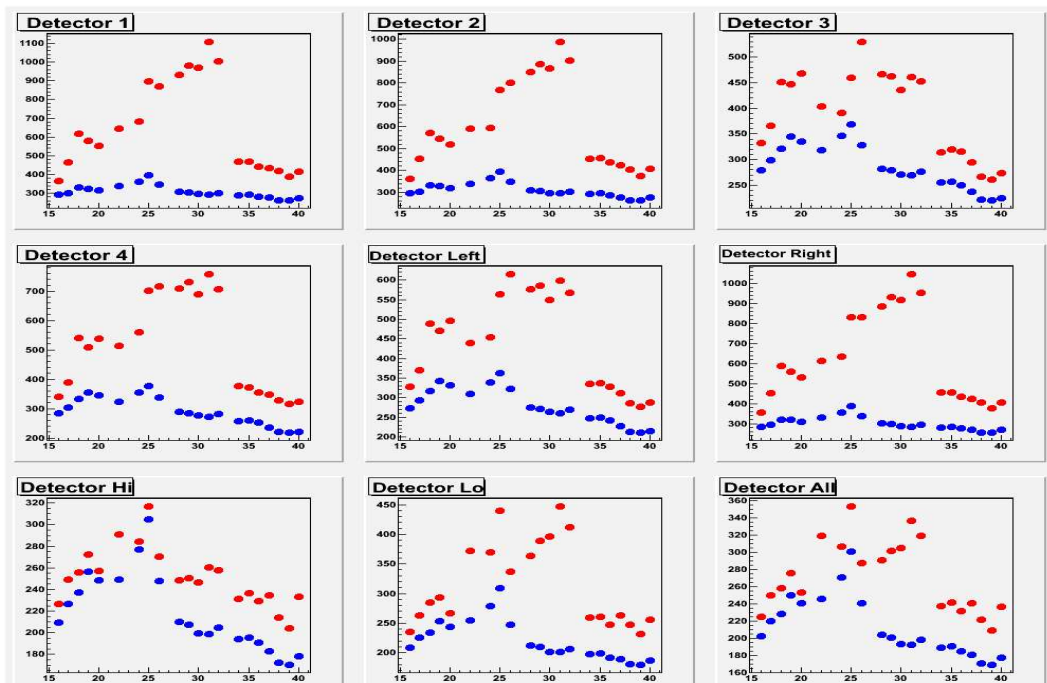
FIG. 4.10: Slugs widths with and without regression for each production slug. Horizontal axis is the production slug and vertical axis is ADC channels. Blue points are the widths of production slugs after regression and red points are the widths of production slugs before regression.

The melting of the target can be seen from these widths. From slug 16 to 32 asymmetry width is increasing due to the target melting. For last seven slugs we used the third Lead target which has the largest thickness of Carbon and it took longer time by radiation to destroy the crystal structure and reduce the thermal

conductivity.

4.13 Carbon Background

Three Lead targets are used for PREx and each of them is sandwiched between two diamond foils. The diamond foils are nominally 0.15 mm thick and the Lead is 0.55 mm thick. Carbon background should be subtracted from Lead raw asymmetry to get the Lead parity violating asymmetry according to equation4.20. Carbon asymmetry is well known and given by

$$A = \frac{3}{2} \frac{G_F Q^2}{\pi \alpha \sqrt{2}} \tilde{\gamma}, \tag{4.18}$$

where G_F is Fermi's constant, $\alpha = 1/137$, $\tilde{\gamma} = \frac{2}{3} \sin^2 \theta_{Weak}$ and Q^2 is four momentum transfer. The theoretical value of Carbon asymmetry is 0.637ppm at $Q^2 = 0.009 GeV^2$. Before the start of PREx it was estimated that the Carbon background is 0.64%[83]. During PREx we took two slugs to measure the asymmetry of Carbon. Each Carbon slug has opposite orientation of IHWP and same orientation of wien filter. Measured Carbon raw asymmetry is 0.5936 ± 0.0504 ppm. The Carbon Q^2 is 8% higher than Lead. In order to substract the Carbon background we need to determine the Carbon fraction which is given by

$$\frac{Carbon}{Lead} = \frac{FF_C^2}{FF_{Pb}^2} \times \frac{Z_C^2}{Z_{Pb}^2} \times \frac{\rho_C/m_C}{\rho_{Pb}/m_{Pb}} = 0.066, \tag{4.19}$$

at q = 0.47 fm^{-1} where FF is form factor, Z is atomic number, ρ is density, t is thickness and m is atomic mass. During the experiment the target melted and target thickness reduced to 90% which resulted an incrase in carbon contamination up to 0.074%. Total Carbon systematics is 0.0025 ppm(0.4%).

4.14   Transverse Asymmetry

Transverse asymmetry arises from one and two photon exchange[84]. Transverse asymmetry is an important systematics of PREx. CEBAF electron beam may have small fraction of electrons which are transversely polarized.
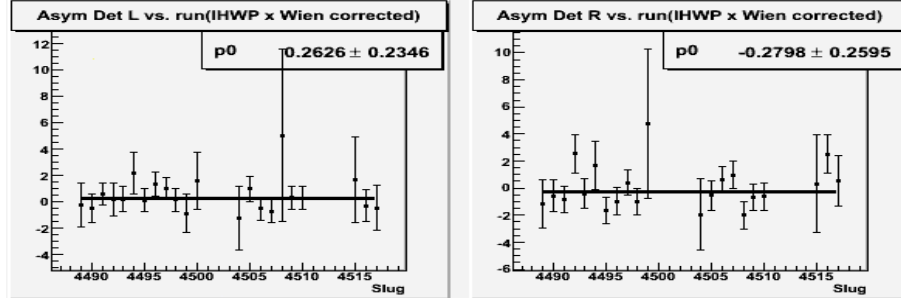
FIG. 4.11: Regressed transverse asymmetry of Lead target for left and right arms.

A non zero transverse asymmetry is due to non zero imaginary part of elastic amplitude. Two photon exchange gives a non zero imaginary part of elastic amplitude. Systematics due to two photon exchange becomes larger for greater scattering angle. Since the PREx asymmetry is half ppm so we carefully measured the size of transverse asymmetry. We took dedicated slugs to find out this small transverse asymmetry. Carbon Transverse asymmetry is also measured. The sign of transverse asymmetry is opposite in left and right detectors and the size is same. It means that the overall effect of transverse asymmetry is negligible.
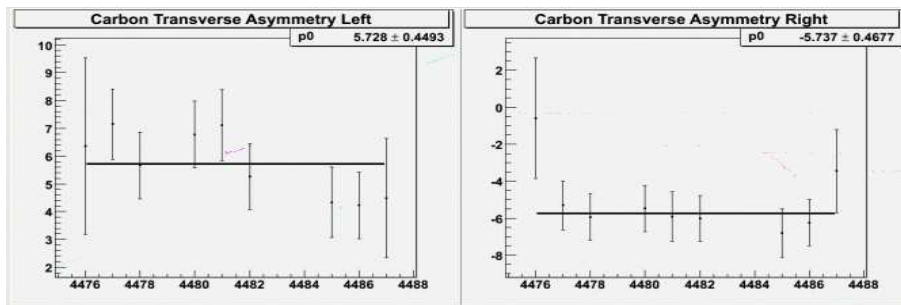
FIG. 4.12: Regressed Carbon transverse asymmetry for left and right arms.

4.15 Q^2 Measurement

Scattering cross section of polarized electrons from the Lead nucleus target is function of Q^2. The Q^2 is the measure of four momentum transfer from incident electron to target nucleus via a virtual boson.

$$Q^2 = -(p - p')^2 = 2EE'(1 - \cos\theta), \tag{4.20}$$

where p and E is four momentum and energy of incoming electron respectively, p' and E' is the four momentum and energy of of scattered electron respectively and θ is the scattering angle. PREx measured the counting rate asymmetry at a unique value of Q^2. Counting mode DAQ and two HRS were used for special runs to measure the PREx Q^2.

4.15.1 Beam Energy

Beam energy is measured by Arc-Energy method developed by French collaboration of Pascal Vernin and the Saclay group. Eight dipole magnets are used to bend the beam line by a nominal angle 34.3° to enter the hall A. The length of this bending arc is 40 m. Arc-Energy method measures the beam energy as a function of bend angle of the arc and filed integral of eight dipole magnets[56]. When electron beam bends by a dipole magnets, its momentum changes and the momentum of the beam is given by:

$$p = \ k \left(\frac{\int \mathbf{B.dl}}{\theta} \right), \tag{4.21}$$

where k = 0.299792 GeV rad T^{-1} m^{-1} c^{-1}, $\int \mathbf{B.dl}$ is the dipole field integral and θ is the bend angle. Field integral of each dipole is measured by a separate dipole and wire scanners are used to measure the bend angle at the same time.

4.15.2 Target Coordinates

Q^2 is a relationship between energy of incoming electron, energy of scattered electron and the scattering angle.
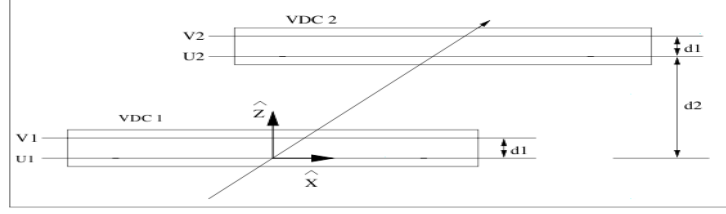
FIG. 4.13: Side view of vertical drift chambers and detector coordinate system. $\hat{y}$ axis is going into the page

The scattering angle is measured by a transformation of focal plane coordinates to the target plane coordinates [85]. A scattered electron passes through the vertical drift chambers[86] and the location of its path is marked by two spatial coordinates x_d and y_d and two angular coordinates θ_d and ϕ_d. These four coordinates are then corrected for any detector offset with respect to a reference set of coordinates to get focal plane coordinates $(x_f, y_f, \theta_f, phi_f,)$. Focal plane coordinate are transformed to the target coordinates$(x_t, y_t, \theta_t, phi_t,)$ by a set of tensors:

$$y_t = \sum_{j,k,l} Y_{j,k,l} \theta_f^j y_f^k \phi_f^l, \tag{4.22a}$$

$$\theta_t = \sum_{j,k,l} T_{j,k,l} \theta_f^j y_f^k \phi_f^l, \tag{4.22b}$$

$$\phi_t = \sum_{j,k,l} T_{j,k,l} \theta_f^j y_f^k \phi_f^l, \tag{4.22c}$$

$$\delta_t = \sum_{j,k,l} T_{j,k,l} \theta_f^j y_f^k \phi_f^l, \tag{4.22d}$$

Following diagram shows the target coordinate system:
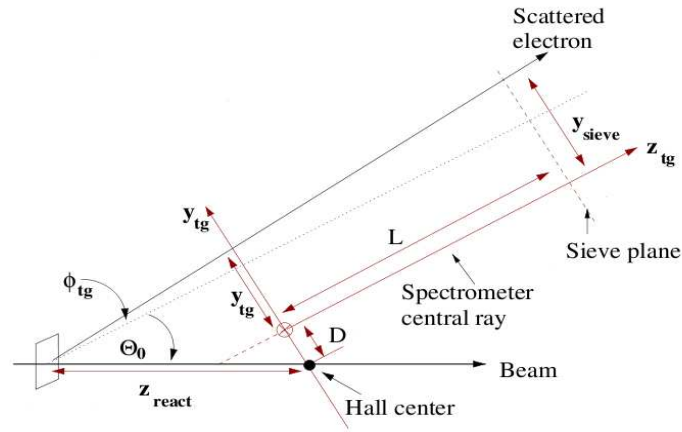
FIG. 4.14: Target coordinate system.

where transformation tensors $Y_{j,k,l}$, $T_{j,k,l}$, $P_{j,k,l}$ and $D_{j,k,l}$ are polynomials in x_f. These polynomials can be of the order of five. The final transformation for y_t for example is given by:

$$y_t = \sum_{j,k,l} \sum_{i=1}^{m} C_i^{Y_{jkl}} x_f^i \theta_f^j y_f^k \phi_f^l, \tag{4.23}$$

A sieve plate show in figure 4.15 is used to optimize the θ_t and ϕ_t.
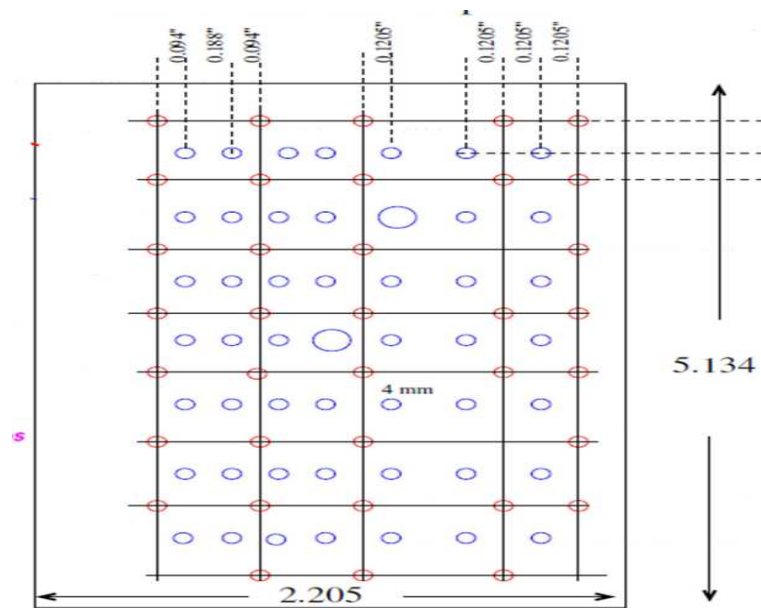
FIG. 4.15: A schematic diagram of sieve plate.

Figure 4.16 and 4.20 shows the sieve slit pattern. The red vertical and horizontal lines are calculated from the target coordinates and blue blobs are the data.
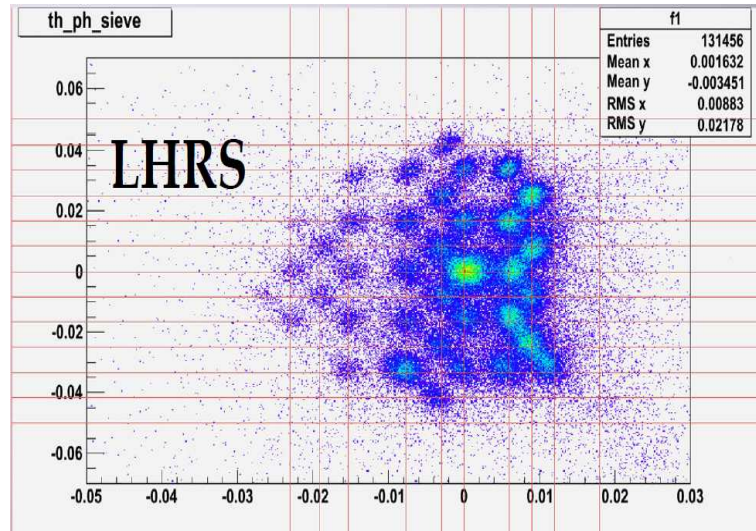
FIG. 4.16: Sieve plate data for left HRS.
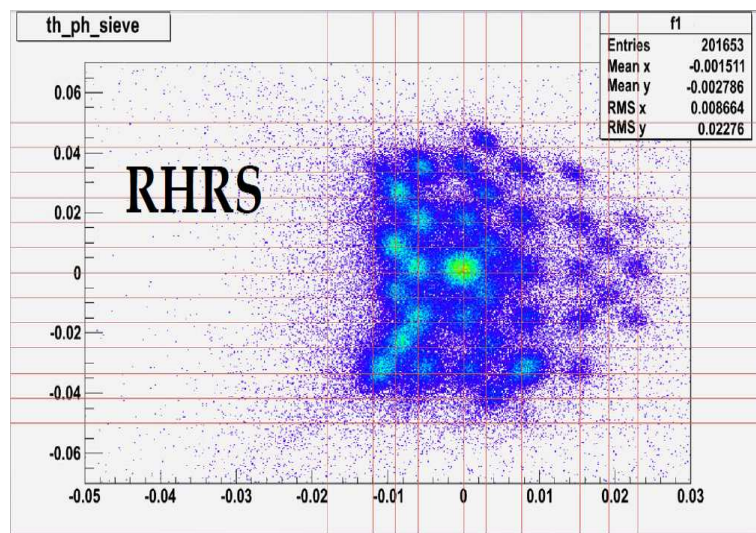
FIG. 4.17: Sieve plate data for right HRS.

4.15.3 Central Scattering Angle

The largest part of systematic correction to Q^2 comes from determination of the absolute value of scattering angle in lab. Central scattering angle is measured

by using a water cell target. Central scattering angle of left and right HRS is determined by measuring the energy of elastically scattered electrons from different targets. These targets have a good separation of elastic peaks. The relationship of scattering angle and incident energy E_0, measured energy of scattered electron E', incoming electron's' mass m and the recoiling nucleus mass m^* is given by

$$E' + \epsilon' = \frac{E_0 - \epsilon_0 - \frac{1}{2m}(m^{*2} - m^2)}{1 + (1 - \cos\theta)(E_0 - \epsilon_0)/m}, \tag{4.24}$$

where ϵ_0 and ϵ' are the energy loss of the incident and detected electrons respectively. The peak shapes of water cell Q^2 graph is fit with a Gaussian convoluted with and exponential given by equation 4 of [87].

Energy of scattered electron is $E' = \mathbf{p}_0(1 + \delta + \triangle\delta)$ where $\mathbf{p}_0$ is the central momentum setting of the spectrometer, δ is the fraction difference of the reconstructed momentum from $\mathbf{p}_0$ and $\triangle\delta$ is the second order correction to δ and it accounts for the local imperfections in the reconstruction matrix. The Q^2 for left and right arm are given below for trigger T1 and trigger T5. Trigger T1 is a scintillator above the VDC planes and trigger T5 is a scintillator above the PREx detectors. PREx parity violating asymmetry is measured by using the integrating mode in which the ADC value is generated by the energy deposit by the scattered electrons in the PREx detector. Q^2 is weighted by the PREx detector's ADC values to account for the integrated signal of detector, $Q^2 = \frac{\sum Q_i^2 W_i}{\sum W_i}$ where W_i is the weight factor of event i and Q_i^2 is the corresponding Q^2 measurement. Q^2 for left arm is 0.009330 GeV^2, for right arm Q^2 is 0.008751 GeV^2 and the average Q^2 of PREx is 0.009068 GeV^2. Q^2. For both arms Q^2 is weighted by N/σ^2 for each run. Figures 4.18 and 4.19 shows the Q^2 for left and right arms respectively.

The uncertainty in Q^2 is give by
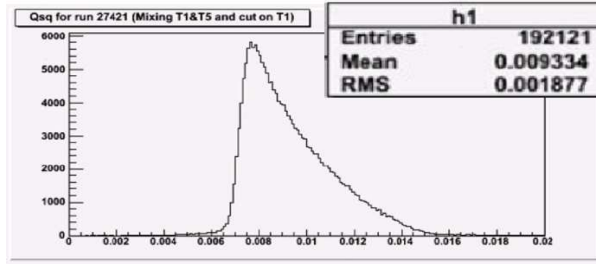
FIG. 4.18: Left arm Q^2 with triggers T1 and T5 and a cut on trigger T1. Run no. 27421 from [88].
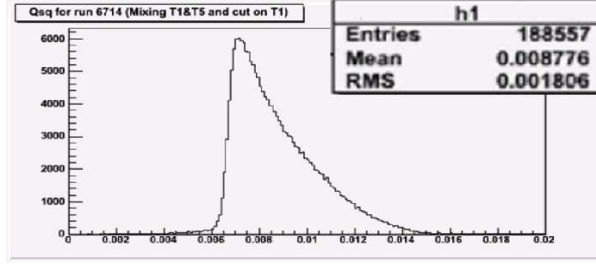
FIG. 4.19: Right arm Q^2 with triggers T1 and T5 and a cut on trigger T1. Run no. 6719 from [88].

$$Q^2 = 2EE'(1 - \cos\theta_{scat}), \tag{4.25a}$$

$$\delta Q^2 = \sqrt{((\tfrac{\partial Q^2}{\partial E})\delta E)^2 + ((\tfrac{\partial Q^2}{\partial E'})\delta E')^2 + ((\tfrac{\partial Q^2}{\partial\theta_{scat}})\delta\theta_{scat})^2}, \tag{4.25b}$$

The uncertainties in the central scattering angles are 0.43 mrad(0.49%) and 0.37 mrad (0.43%) for left and right arms respectively. The uncertanity in Q^2 of left and right HRS are 0.98% and 0.86% respectively. The uncertainties in Q^2 from E and E' are negligible.

4.16 Inelastic

Most of the background due to inelastic comes from first excited states of Lead and Carbon. Following diagram shows the first excited states of Lead(3-) and Carbon. The first excited state of Carbon is out of our acceptance and it does not

contribute. The fraction of first excited state of Lead(3-) is $(\sigma_{3-}/\sigma_{PV}) \approx 0.1\%$. After correcting for acceptance this fraction even reduces to 0.06% and the asymmetr due to inelastics from first excited state of Lead(3-) is $A_{(3-)} = 0.00075 A_{elastics}$. Higher excited states of Lead 4- and 5- are out of our acceptance.
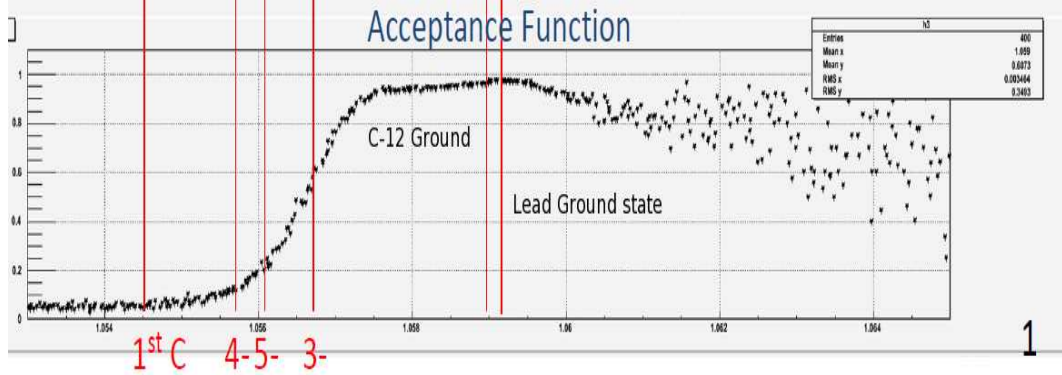
FIG. 4.20: Inelastics from excited states of Lead and Carbon.[89].

4.17 Acceptance

In equation 4.20 K is correction for acceptance and it appears as an overall function. This method is appropriate for HAPPEX experiment but for PREx where asymmetry is complicated function of Q^2 one needs to integrate over acceptance. A simulation is used to perform the integration and to calculate the parity violating asymmetry at the effective Q^2. The finite acceptance is included in this simulation.

4.18 PREx Asymmetry

In equation 4.20 A_{coor} is $(A_{rarw} - A_{beam})$ where A_{beam} is the beam corrected asymmetry which is measured separately by two independent methods, beam modulation and regression. One CODA run is almost on hour long and has typically 50k quadruplets. We averaged over 316 set of A_{corr} and normalized by corresponding

statistical error and it showed that data behaved statistically. The corrected PREx asymmetry is

$$(\mathbf{A_{corr} = 593 \pm 50(stat) \pm 10(syst))ppb}, \tag{4.26}$$

In order to get Physics asymmetry we have to subtract background from A_{corr} as given in equation 4.20 and then integrate over acceptance because asymmetry of Lead is function of Q^2.

CHAPTER 5

Summary and Conclusion

In this chapter the results of parity analysis of PREx and the results of Flash ADC DAQ are discussed. Important results and achievements of PREx are presented and future of PREx is discussed.

5.1 Flash ADC Data Acquisition System

The important results of FADC DAQ are summarized here. Flash ADC DAQ is simple and easy to handle. FADC DAQ uses only five slots of a VME crate and new modules can be added without any problem. Flash ADC is stable in high background, see figure 3.21. Rates measured by data triggers and onboard scalers are in good agreement with each other, table 3.7.3. The asymmetry measured by data triggers and onboard scalers is almost the same, see section 1.7.5. Flash ADC has negligible dead time of 150 nsec, section 1.7.4. The sample time of FADC is 4 nesc so this 150 nsec time delayed is due to FPGA. This 150 nsec time delayed systematics of FADC DAQ is negligible for present requirements of beam polarization measurements of hall A. Finally the raw asymmetry measurements of old DAQ and FADC DAQ are in good agreement with each other, see figure 3.25. Flash ADC data

114

acquisition system is fully operational and ready to measure the beam polarization.

5.2 PREx Results and Future Plans

PREx started at March 19th and ended in June 20th to measure the neutron radius via parity violating scattering. Before PREx the known values of neutron densities come from the hadron scattering experiments [90], [91], [92], [93] and [94]. The interpretation of hadron scattering is model dependent because of uncertainties in strong interactions. Parity violating asymmetry measurement gives the model independent value of neutron density distribution. Despite the fact that only 20% of the required statistics were obtained, important experimental achievements were made during the run of PREx. First time in Jefferson lab the cumulative pulse pair width was kept under 200 ppm at 30 Hz. Most of the time during PREx, the beam current was 50 μA but for last seven days the beam current was raised to 70 μA and the pulse width did not increased, see figure 4.10. PREx detectors are also a success which give a narrow width for mono energetic 1 GeV electrons at high rates. Calibration of a tune for two high resolution spectrometers may take months but during the experiment a new tune was successfully developed. The new tune was able to focus the elastic peak to a very small area. PREx target is Lead which may result in very high rates for Q^2 measurements. New cavity monitors are a success to work at nano amp current range, see figure 2.20 for Q^2 measurements. The beam corrected PREx asymmetry is below:

$$(\mathbf{A_{corr}} = \mathbf{594 \pm 50(stat) \pm 9(syst))ppb}, \tag{5.1}$$

and PREx parity violating asymmetry is given by:

$$(\mathbf{A_{phy}} = \mathbf{656 \pm 60(stat) \pm 14(syst))ppb}, \tag{5.2}$$

A correlation between parity violating asymmetry and neutron radius is shown in figure 5.1. In figure 5.1 different mean field models are used to calculate the relationship between parity violating, A_{pv} and the neutron radius R_n[95]. For each model the calculation is performed with proton weak charge $q_p = -0.0721$ and neutron weak charge $q_n = 0.9878$. Calculation for each model is performed with the models' neutron density and the experimental charge density of neutron. A fit to these models is shown by dark line. PREx physics asymmetry value gives the neutron radius, $\mathbf{R_n = 5.78^{+0.16}_{-0.18} fm}$.
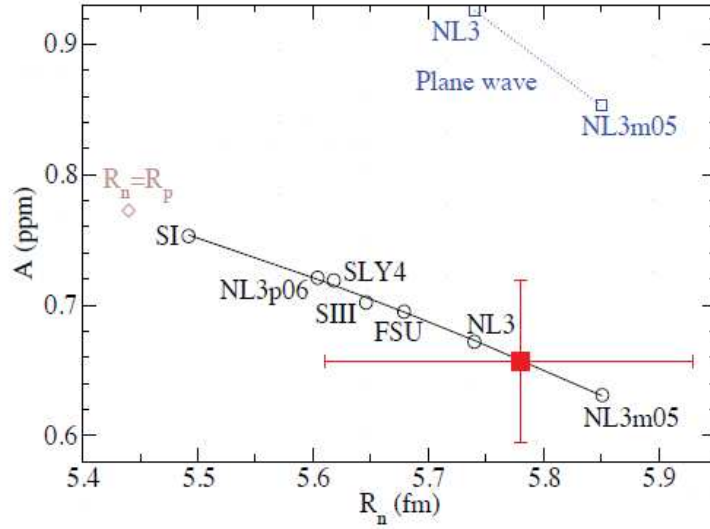
FIG. 5.1: Seven mean field neutron densities are shown in circles [95]. Result of PREx is shown in Red. Diamond show the result of calculations for $R_n = R_p$. Blue squares show plane wave impulse approximation results.

It is estimated that the total error of parity violating asymmetry of the first run of PREx will give us neutron radius with an error of 2.5%. Another achievement of PREx is that it has successfully established the existence of neutron skin. R_n - R_p = $0.33^{+0.16}_{-0.18} fm$.

A second run of PREx is approved and planned to run after 12 GeV upgrade of Jefferson lab. One of the important applications of PREx is to the study of Neutron

stars and supernova. It is very interesting that one single precise measurement of neutron radius has impact to:

Does a supernova become a neutron star or black hole?

What is density and size of neutron star?

Does a neutron exotic core exist?

How fast does a neutron star cool?

There is strong correlation between neutron radius and pressure of neutron matter at densities near 0.1 fm^{-3}, the 2/3 of nuclear density.

Lattimar and Parkash[96] considered the PREx as one of the important experiments to answer thees question.

Following figures show the correlation between neutron radius r_n in Lead and neutron form factor(left) and correlation between neutron skin $r_n - r_p$(fm) and symmetry energy(right) calculated [97] using the Hartree-Fock calculation.

FIG. 5.2: Left: Predictions for relativistic hartree-Fock calculations Neutron form factor v/s neutron radius r_n in Lead. Right: Correlation between neutron skin $r_n - r_p$(fm) and symmetry energy.

The entire spread of these models in figure 5.2 is about 4% and the current error of 2.5% has no impact but an error of 1% is very important.

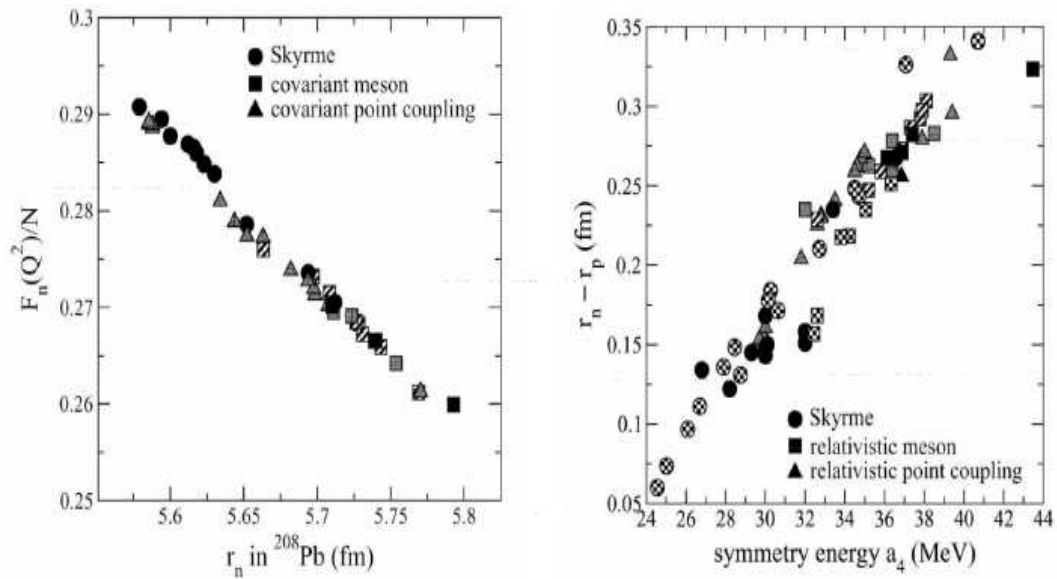The neutron radius can be measured with different nuclei. For a second run of PREx different choices of targets are discussed and the statistical errors are estimated in[95]. The possible new candidates for second run of PREx are ^{40}Ca, ^{48}Ca, ^{112}Sn, ^{120}Sn, ^{124}Sn and ^{208}Pb. Smaller nuclei are better candidate for parity violating asymmetry measurement. The parity violating asymmetry of smaller nuclei is large for higher momentum transfer large. Another important fact is that the neutron rich isotope has higher weak charge radius. This makes ^{48}Ca a very promising candidate and it has higher figure of merit than ^{208}Pb. On the other and PREx collaboration had already worked with ^{208}Pb target. ^{208}Pb target is studied very well and all of its important systematics are well known. The statistical error estimates for measuring the neutron radius R_n in 30 days for three different nuclei is shown in table 5.2. Neutron and Proton densities are calculated in they skyrme HF theory with the SLY4 inxtraction.

Target	Energy	$A_{pv}(5°)$	$\frac{d\sigma}{d\omega}(5°)mb/str$	Rate	ϵ_{Rn}	$\frac{\triangle R_n}{R_n}$
	GeV	ppm	mb/str	MHz/arm		%
^{208}Pb	1.05	0.7188	1339	1736	-2.762	0.6637
^{48}Ca	1.80	2.358	8.630	164.3	-4.266	0.4258
^{40}Ca	1.90	2.301	5.832	111.0	-3.920	0.5777

where $\epsilon_{Rn} = dlnA_{pv}/dlnR_n$. After measuring the neutron radius R_n a second measurement at high momentum transfer will constrain the surface thickness a_n of the neutron density.

APPENDIX A

2010 PREx Collaboration

2010 PREx Collaboration

X. Zhan
Argonne National Laboratory, Argonne, Illionis 60439, USA

K. Aniol
California State University, Los Angeles, Los Angeles, California 90032, USA

K. Aniol, D. Margaziotis
California State University, Los Angeles, Los Angeles, California 90032, USA

G. B. Franklin, M. Friend, D. Parno, B. Quinn
Carnegie mellon Univesity, Pittsburgh, Pennsylvania 15213, USA

C. E. Hyde, C. Muñoz-Camacho,
Clermont Université, Université Blaise Pascal, CNRS/IN2P3

D. S. Armstrong, T. Averett, W. Deconinck, J. Hoskins, E. Jensen, J. Leckey IV,
J. H. Lee
College of William and Mary, Williamsburg, Virginia 23187, USA

F. Benmokhtar, P. Carter,
Christopher Newport University, Newport News, Virginia 23187, USA

W.Boeglin, P. Markowitz
Florida International University, Miami, Florida 33199, USA

C. Chen, Z. Ye
Hampton University, Hampton, Virginia 23668, USA

R. Wilson

Harvard University, Cambridge, Massachusetts 02138, USA

R. De Leo

INFN, Sezione di Bari and University of Bari, I-70126 Bari, Italy

V. Bellini, A Giusa, G. Russo, M. L. Sperduto, C. M. Sutera

INFN, Dipt. di Fisica dell'Univ. di Catania, I-95123 Catania, Italy

G. M. Urciuoli

INFN, Sezione di Roma and Spienza - Università di Roma, I-00161 Rome, Italy

F. Cusanno, S. Frullani, F. Garibaldi, F. Mammoliti

INFN, Sezione di Roma, gruppo Sanità and Istituto Superiore di Sanità, I-00161 Rome, Italy

C. J. Horowitz

Indiana university, Bloomington, Indina 47405, USA

M. Mihovilovie, S. Sirca

Institut Jožef Stefan, 3000 SI-1001 Ljubljana, Slovenia

A. Glamazdin, R. Pomatsalyuk,

Kharkov Institute of Physics and Technology, Kharkov 61108, Ukraine

H. Albataineh, A. Eile, E. Gasser, F. Itard

laboratoire de Physique Corpusculaire, Clermont-Ferrand Campus des Czeaux 24, avenue des Landais BP 80026 63171 Auvire Cedex, France

G. Ron

Lawrence Berkeley National Laboratory, Berkeley, California 94720, USA

T. Holmostrom, W. Troth

Longwood University, Farmville, virginia 23909, USA

A. Puckett

Los Alamos National Laboratory, Los Alamos, New Mexico 87545, USA

W. Deconinck, J. Huang, A. Kelleher, S. Kowalski, N. Muangma, V. Sulkosky

Massachusetts Institute of Technology, Cambridge, Massachusetts 02139, USA

D. Dutta, N. Nuruzzaman

Mississippi State University,Mississippi State, Mississippi 39762, USAS

R. Beminiwattha, P. King, B. Waidyawansa

Ohio university, Athens, Ohio 45701, USA

M. Canan, C. E. Hyde

Old Dominion University, Norfolk, Virginia 23529, USA

N. Lubinsky

Rensselaer Polythechnic Institute, Troy, New York 12180, USA

R. Gilman, Y. Zhang

Rutgers University, The StateUniversity of New Jersey, new Brunswick, New Jersey 08901, USA

Y. Oh

Seoul National University, Seoul 151-742, South Korea

P. Decowski

Smith College, Northampton, Massachusetts 01063 USA

Z. Ahmed, R. S. Holmes, A. Rakhman, P. A. Souder, L. Zana

Syracuse University, Syracuse, New York 13244, USA

O. Chen, K. Kliakhandler

Tel Aviv University, P.O. Box 39040, Tel-Aviv 69978, Israel

W. Armstrong, D. Flay, E. Fuchey, Z.-E. Meziani, M. Posik, H. Yao

Temple University Philadelphia, Pennsylvania 19122, USA

J. Benesch, A. Camsonne, J.-P. Chen, K. de jager, A. Deur, J. Gomez, J. Grames, O. Hansen, J. Hansknecht, D. W. Higinbotham, J. J. LeRose, A. McCreary, R. W. Michaels, S. Nanda, B. Poelker, A. Saha, B. Sawatzky, A. Shahinyan, P. Solvignon-Slifer, R. Suleiman, B. Wojsekhowski, J. Zhang

Thomas Jefferson National Accelerator Facility, Newport News, Virginia 23606 USA

S. Johnston, K. S. Kumar, J.Mammei,D. McNulty, L.Mercado, P. Rogan, J.Wexler, V. Yim

University of Massachusetts Amherst, Amherst, Massachusetts 01003, USA

T. Bielarski, S. K. Phillips, K. Slifer

University of New Hampshre, Durham, New Hampshire 03824, USA

X. Yan, Y. Ye, P. Zhu

University of Science and Technology of China, Hefei, Anhui 230026, P. R. China

B. Babineau, A. Barbieri, G. D. Cates, M. Dalton, K. de Jager, X. Deng, C. Gu, G. Jin, R. Lindgern, N. Liyanage, V. Nelyubin, K. D. Paschke, K. Saenboonruang, R. Silwal, R. Subedi, W. A. Tobias, D. Wang, Z. Ye, X. Zheng

University of Virginia, Charlottesville, Virginia 22903 USA

J. Leacock

Virginia Polytechnic Institute and State Unviersity, Blacksburg, Virginia 24061, USA

S. Abrahamyan, A. Shahinyan

Yerevan Physics Institutte, yerevan, Armenia

BIBLIOGRAPHY

[1] G. Fricke *et al.*, At. Data Nucl. Data Tables **60**, 177 (1995).

[2] T. D. Lee and C. N. Yang, Phys. Rev. **104**, 254 (1956).

[3] C. S. Wu *et al.*, Phys. Rev. **105**, 1413 (1957).

[4] A. Salam, Almquist Forlag Stockholm (1968).

[5] S. Wienberg, Phys. Lett. **19**, 1264 (1967).

[6] S. Glashow, Nuc. Phys. **22**, 579 (1961).

[7] F. J. Hasert *et al.*, Phys. Lett. **B46**, 138 (1973).

[8] C. Y. Prescott *et al.*, Phys. Lett. **B77**, 347 (1978).

[9] H. de Vries, C. W. de Jager, and C. de Vries, Atomic and Nuclear Data Tables **36**, 495 (1987).

[10] T. W. Donnelly, J. Dubach, and I. Sick, Nucl. Phys. **A503**, 589 (1989).

[11] B. J. Moffit, Ph.D. thesis, The College of Willam and Mary, 2007.

[12] J. D. Walecka, *Electron Scattering for Nucelar and Nucleon Structure* (Cambridge Monographs, Cambridge, 2001).

[13] T. W. Donnelly and R. D. Peccei, Phys. Reports **50**, 1 (1979).

[14] T. W. Donnelly and J. D. Walecka, Ann. Rev. Nucl. Sci. **25**, 329 (1975).

[15] C. J. Horowitz, S. J. Pollokc, P. A. Souder, and R. Michaels, Phys. Rev. C **63**, 025501 (2001).

[16] J. J. A. Nolen and J. P. SChiffer, Phy. Lett. **29B**, 396 (1969).

[17] L. Ray and G. W. Hoffmann, Phys. Rev. C **31**, 538 (1985).

[18] H. J. Korner and J. P. Schiffer, Phys. Rev. Lett. **27**, 1457 (1971).

[19] X. Roca-Maza, M. Centeles, X. Vinas, and M. Warda, arXiv:1103.1762v2 (2011).

[20] E. D. Cooper and C. J. Horowitz, Phys. Rev. C **72**, 034406 (2005).

[21] M. Gorchtein and C. J. Horowitz, arXiv:0801.4575v2 (2008).

[22] C. J. Horowitz, Phys. Rev. C **21**, 254 (1998).

[23] C. J. Horowitz and S. B.D., Nuc. Phys A **368**, 503 (1981).

[24] B. Povh, Nucl. Phys. A **532**, 133 (1991).

[25] K. A. Aniol *et al.*, Phys. Rev. Lett. **82**, 1096 (1999).

[26] B. Muller *et al.*, Phys. Rev. Lett. **78**, 3824 (1997).

[27] A. Bohr and B. R. Motelson, *Nuclear Structure Vol. II* (Benjamin, ADDRESS, 1975).

[28] D. Goutte *et al.*, Phys. Rev. Lett. **45**, 20 (1980).

[29] G. Feinberg, Phys. Rev. D **12**, 3575 (1975).

[30] C. J. Horowitz, R. J. P. B.C. Clark, and J. P. Vary, *Relativistic Nuclear Many Body Physics* (World Scientific, ADDRESS, 1988).

[31] V. Dmitrasinovic and S. J. Pollock, Phys. Rev. **C52**, 1061 (1995).

[32] S. C. Bennett and C. E. Wieman, Phys. Rev. Lett. **82**, 2484 (1999).

[33] W. Marciano and J. Rosner, Phys. Rev. Lett. **65, 68**, 2963, 898 (1990, 1992).

[34] S. A. Blundell, J. Sapirstein, and W. R. Johnson, Phys. Rev. D **45**, 1602 (1990).

[35] V. A. Dzuba *et al.*, Phys. Lett. A **141**, 147 (1989).

[36] A. W. Steiner, M. Parkash, J. M. Lattimer, and P. J. Ellis, Phys. Rep. **411**, 325 (2005).

[37] B. G. Todd-Rutel and J. Piekarewicz, Phys. Rev. Lett. **95**, 122501 (2005).

[38] C. J. Horowitz and J. Piekarewicz, Phys. Rev. Lett. **86**, 5647 (2001).

[39] J. Xu *et al.*, Astrophys. J. **697**, 1549 (2009).

[40] A. W. Steiner and A. L. Watts, Phys. Rev. Lett. **103**, 181101 (2009).

[41] D. H. Wen, B. A. Li, and P. G. Krastev, Phys. Rev. C **80**, 025801 (2009).

[42] K. A. Aniol *et al.*, Phys. Rev. C **69**, 265501 (2004).

[43] G. D. *et al.*, Nucl. Instrum. Methods A **278**, 293 (1989).

[44] T. B. Humensky *et al.*, Nucl. Instrum. Methods A **521**, 261 (2004).

[45] G. Lampel, Phys. Rev. Lett. **23**, 491 (1968).

[46] D. T. Pierce, F. Meier, and P. Zurcher, Appplied Physics Letters **26**, 670 (1975).

[47] T. Maruyama *et al.*, Applied Physics Letters **85**, 2640 (2004).

[48] M. Baylac *et al.*, Phys. Rev. Special Topics - Acce. and Beams **8**, 123501 (2005).

[49] N. F. Mott, Proc. R. Soc. Lond **124**, 425 (1929).

[50] D. Parno *et al.*, arXiv:1106.4851v1 (2011).

[51] W. Barry, J. Heefner, and J. Perry, CEBAF PR-90-023 (1990).

[52] K. Unser, IEE Trans. Nucl. Sci. **28**, 2344 (1981).

[53] V. von, *Cavity Beam Position Monitor for the TESLA- cryomodule Cross-Talk minimization* (PUBLISHER, ADDRESS, 2003).

[54] (http://www.apiezon.com/apiezon-l-grease.htm).

[55] T. Behnke *et al.*, NIM A **489**, 230 (2002).

[56] J. Alcorn *et al.*, Nucl. Inst. and Meth. in Phy. Research A **522**, 294 (2004).

[57] C. Moller, Ann. Phys. **14**, 531 (1932).

[58] W. Greiner and J. Reinhardt, *Quantum Electrodynamics* (Springer, ADDRESS, 2002).

[59] G. W. Ford and C. J. Mullin, Phys. Rev. **108**, 477 (1957).

[60] B. Wagner *et al.*, Nuc. Inst. and Meth. in Phys. Res. **A294**, 541 (1990).

[61] H. Olsen., *Springer Tracts in Mod. Phys.* (Springer, ADDRESS, 1968).

[62] A. Bincer, Phys. Rev. **107**, 1434 (1957).

[63] E. A. Chudakov, JLab Hall A General Operations Manual 416 (2011).

[64] E. A. Chudakov *et al.*, Exp. Meth. and Processing of Data .

[65] W. Hofmann *et al.*, Nucl. Inst. and Meth. **128**, 283 (1982).

[66] P. D. Group, Phys. Lett. B **239**, 1 (1990).

[67] O. Glamazdin, http://www.jlab.org/ moller/docs/des2.ps.gz.

[68] O. Glamazdin, http://www.jlab.org/ moller/.

[69] M. Hauger *et al.*, nucl-ex/9910013v1 17 (1999).

[70] D. P. Barber *et al.*, Nucl. Instr. and Meth. A **329**, 79 (1993).

[71] D. Abbott, Jefferson Lab CODA Group, https://coda.jlab.org/wiki/index.php/.

[72] L. G. Levchuk, Nuc. Inst. Meth. Phys. Resaarch A **345**, 496 (1994).

[73] A. Afanasev and A. Glamazdin, hep-ex/9602002v1 11 (2002).

[74] M. Loppacher, *Moller Polarimeter for CEBAF Hall C* (PUBLISHER, ADDRESS, 1996).

[75] Z. Ahmed, PREx Colleboration Meeting Feb 20 2010, 2010, http://hallaweb.jlab.org/experiment/HAPPEX/minutes.html.

[76] R. Pomatsalyuk, PREx Colleboration Meeting Jan 29 2011, 2011, http://www.jlab.org/ moller.

[77] L. J. Kaufman, *Precision Measurement of the Proton Neutral Weak Form Factors at Q^2 0.1 GeV^2* (PUBLISHER, ADDRESS, 2007).

[78] J. Alcorn *et al.*, Nucl. Inst. and Meth. in Phy. Res. **A 522**, 294 (2004).

[79] G. Heyes *et al.*, Proceedings of the CHEP Coference 122 (1994).

[80] E. Jastrzembski *et al.*, 11th IEEE NPSS Real Time 1999 Conference (1999).

[81] R. Holmes, Parity Analyzer, http://www.phy.syr.edu/ rsholmes/happex/pan/html/index.html.

[82] ROOT, Ojbect Oriented Data Analysis Framework, http://root.cern.ch/.

[83] R. Michaels, Carbon Background Systematics, 2010, hallaweb.jlab.org/parity/prex/docs/c12bgr.pdf.

[84] M. Gorchtein and C. J. Horowitz, arXiv:0801.4575v2 6 (2008).

[85] N. Liyanage, Optics Calibration of Hall A HRS usng new C++ Optimizer, 2002, tN-02-012.

[86] K. G. Fissum *et al.*, Vertical Drift Chambers for Hall A, 2000, tN-00-016.

[87] R. Michaels *et al.*, Q^2 for HAPPEX-2, 2005.

[88] N. Liyanage and K. Saenboonruang, Q^2 and Elastic Carbon Background in Lead Analysis of PREx, 2011.

[89] K. Saenboonruang, HAPLOG 2583, 2011.

[90] C. Garcia-Reio, J. Nieves, and E. Oset, Nucl. Phys. **A 547**, 473 (1992).

[91] L. Ray, W. R. Coker, and G. W. Hoffmann, Phys. Rev. **C 18**, 2641 (1978).

[92] V. E. Starodubsky and N. M. Hintz, Phy. Rev. **C 49**, 2118 (1994).

[93] B. C. Clark, L. J. Kerr, and S. Hama, Phy. Rev **C 67**, 054605 (2003).

[94] A. Trzcinska *et al.*, Phys. Rev. Lett. **87**, 082501 (2001).

[95] S. Ban, C. J. Horowitz, and R. Michaels, arXiv:1010.3246 (2010).

[96] J. M. Lattimer and M. Prakash, Science **304**, 536 (2004).

[97] R. J. Furnstahl, Phys. Rev. **A 706**, 85 (2002).

VITA

<u>Zafar Ahmed</u>

Zafar Ahmed was born in Chenab Nagar(Rabwah), Punjab, Pakistan on August 12, 1978. He passed his F.Sc. examination in 1996 from Nusrat Jehan Inter College Chenab Nagar(Rabwah). In 1998 he received his B.Sc. from Government College University Lahore. Zafar Ahmed got his M.Sc. Physics degree from Quaid-i-Azam University Islamabad in 2001. In fall of 2001 Zafar Ahmed was awarded with UNESCO scholarship for one year diploma in theoretical high energy physics from Abdus Salam International Center for Theoretical Physics and successfully earned the diploma in the fall of 2002. In spring of 2004 he enrolled in the graduate program in Physics at the Syracuse University. Zafar Ahmed received his M.S. from Syracuse University and joined the medium energy experimental group of professor Paul Souder. Zafar Ahmed defended his thesis on April 30, 2012.